SERI/STR-211-3350
UC Category: 271
DE88001169

Research on Amorphous-Silicon-Based Thin-Film Photovoltaic Devices

Semiannual Subcontract Report
1 July 1987 – 31 December 1987

W. Bottenberg
K. Mitchell
R. Wieting
ARCO Solar, Inc.
Camarillo, California

D.L. Morel, Project Director

SERI Technical Monitor: W. Luft

May 1988

Prepared under Subcontract No. ZB-7-06003-3

Solar Energy Research Institute
A Division of Midwest Research Institute

1617 Cole Boulevard
Golden, Colorado 80401-3393

Prepared for the
U.S. Department of Energy
Contract No. DE-AC02-83CH10093

Printed in the United States of America
Available from:
National Technical Information Service
U.S. Department of Commerce
5285 Port Royal Road
Springfield, VA 22161

Price: Microfiche A01
Printed Copy A06

Codes are used for pricing all publications. The code is determined by the number of pages in the publication. Information pertaining to the pricing codes can be found in the current issue of the following publications, which are generally available in most libraries: *Energy Research Abstracts, (ERA); Government Reports Announcements* and Index (*GRA* and I); *Scientific and Technical Abstract Reports (STAR);* and publication, NTIS-PR-360 available from NTIS at the above address.

SUMMARY

Objective

The primary objective of this contract is to develop 13% aperture area (850 cm^2) efficiency four-terminal hybrid tandem submodules. The module design consists of a copper indium diselenide (CIS) based bottom circuit and a semitransparent thin film silicon hydrogen (TFS) based top circuit.

Discussion

During the first six months we have made significant progress toward achievement of the project goals and objectives. The efficiencies which we have achieved to date are summarized in the tables below.

4-terminal tandem cell (4 cm^2) performance.

Device	Eff. (%)	J_{sc} (mA/cm^2)	V_{oc} (mV)	FF
Semitransparent TFS	9.62	15.8	862	70.5
Filtered CIS	4.55	17.6	392	66.0
Tandem	14.17%			
Stand-alone CIS	8.71	33.0	411	64.2

*ASTM air mass 1.5, global 100 mW/cm^2, 25°C.

4-terminal tandem module performance.

Type	Power (W)	Area** (cm^2)	Eff. (%)	I_{sc} (mA)	V_{oc} (V)	FF
Semitransparent TFS	7.69	843	9.1	262	43.45	0.675
Filtered CIS	2.66	843	3.2	228	19.15	0.608
Tandem	10.35		12.3			
Stand-alone CIS	7.62	844	9.0	611	21.15	0.590

*ASTM air mass 1.5, global 100 mW/cm^2, 25°C.
**Aperture area.

These results have been measured at ARCO Solar using existing SERI calibrated references for TFS. We are working with SERI toward improvement of references and procedures for CIS and the more complex tandem structures.

A key element in the progress for TFS has been the development of ZnO. For the devices reported in the tables above, ZnO is both the front and rear transparent conductor. There is a large component of diffuse scattering in the performance of ZnO due to film texturing.

The performance of CIS devices is in many ways more conventional than TFS. The biggest uncertainty is in the nature and location of the junction. We have begun fundamental measurements of our current devices and development of an operative model. Preliminary results indicate a built-in potential of about 0.93 volts for devices which generate 0.45 volts under standard one sun conditions.

While the TFS and CIS component devices operate well individually, tandem devices made from these are experiencing additional optical losses. Preliminary analysis indicates that major contributions to this loss are coming from reflections at the top TFS and CIS interfaces. The resulting "filter efficiencies" for TFS of 35-40% are below the expected values of 45-55%. Improvement of optical coupling is a key element of future work.

Conclusions

- High performance semitransparent TFS devices and submodules have been fabricated using ZnO as the front and rear transparent conductor.

- High performance CIS devices and submodules have also been fabricated. The location and nature of the junction is not yet understood.

- Representative four-terminal hybrid tandem devices and submodules have been fabricated from TFS and CIS component circuits. Optical coupling between the circuits is lower than expectations due to reflection losses at key interfaces.

CONTENTS

CONTENTS
(continued)

Tables

Figures

CONTENTS
(continued)

CONTENTS
(continued)

CONTENTS
(continued)

INTRODUCTION

Objective

The primary objective of this contract is to develop 13% aperture area (850 cm^2) efficiency four-terminal hybrid tandem submodules. The module design consists of a copper indium diselenide based bottom circuit and a semitransparent thin film silicon hydrogen based top circuit.

This report discusses work completed for the period 07/01/87 through 12/31/87. It is divided into three parts. The first covers progress on transparent thin film silicon hydrogen (TFS) and focusses on results achieved with symmetrical ZnO/TFS/ZnO device structures.

The second section covers progress with copper indium diselenide (CIS). Detailed analysis of device microphysics is presented along with an assessment of factors limiting module level performance.

The third section is divided into two parts. The first presents the latest performance results for tandem cells and modules. The second part is a more extensive study and discussion of the problem of optical coupling between the two components of the four-terminal hybrid tandem structure. Effective optical coupling is a key to the success of this technology.

SECTION 1.0
TFS PROGRESS

1.1 INTRODUCTION

This section summarizes progress and status with thin film silicon (TFS) devices and materials for incorporation with copper indium diselenide (CIS) devices into tandem modules. While a significant fraction of the work reported here was performed under the auspices of the SERI contract, work which preceded the contract period is also included in order to present background for a coherent perspective.

The first division of this section reviews progress in TFS cell performance. Discussed in this section are developments in transparent conductors and contacts, results of parametric variation of TFS cell structure, and the status of TFS doped layers with enhanced microcrystallinity.

The next division summarizes the development status of 30x30 cm submodules based upon these cell structures. The circuit design and consequences of different patterning alternatives are reviewed. Experimentally measured submodule performance is compared to modeled performance projected from performance of individual cells.

Photostability (i.e. Staebler-Wronski stability) of TFS cells and submodules is discussed throughout this report. Generally, stabilized as well as initial device performance is characterized in the various experimental investigations. In addition to these results, a summary of "standard" device stability and comparison between outdoor and simulated solar exposures is made.

A final section briefly discusses optical characteristics of TFS devices relevant to TFS/CIS tandem devices and presents a summary of the impacts of device structure variations reviewed in the previous sections.

1.2 TFS CELL PERFORMANCE PROGRESS

1.2.1 Transparent Conductors, Contacts and Cell Structure Options

It is in the area of transparent conductors and cell structure that some of the most important new developments have occurred. Two alternative structures are compared (Fig. 1-1): glass/tin oxide/TFS(pin)/zinc oxide and glass/zinc oxide/TFS(pin)/zinc oxide.

Use of zinc oxide (ZnO) for the front transparent conductor contact in place of the "traditional" tin oxide (TO) provides significant gains in TFS device current generation while still allowing for good filter quality. This yields corresponding

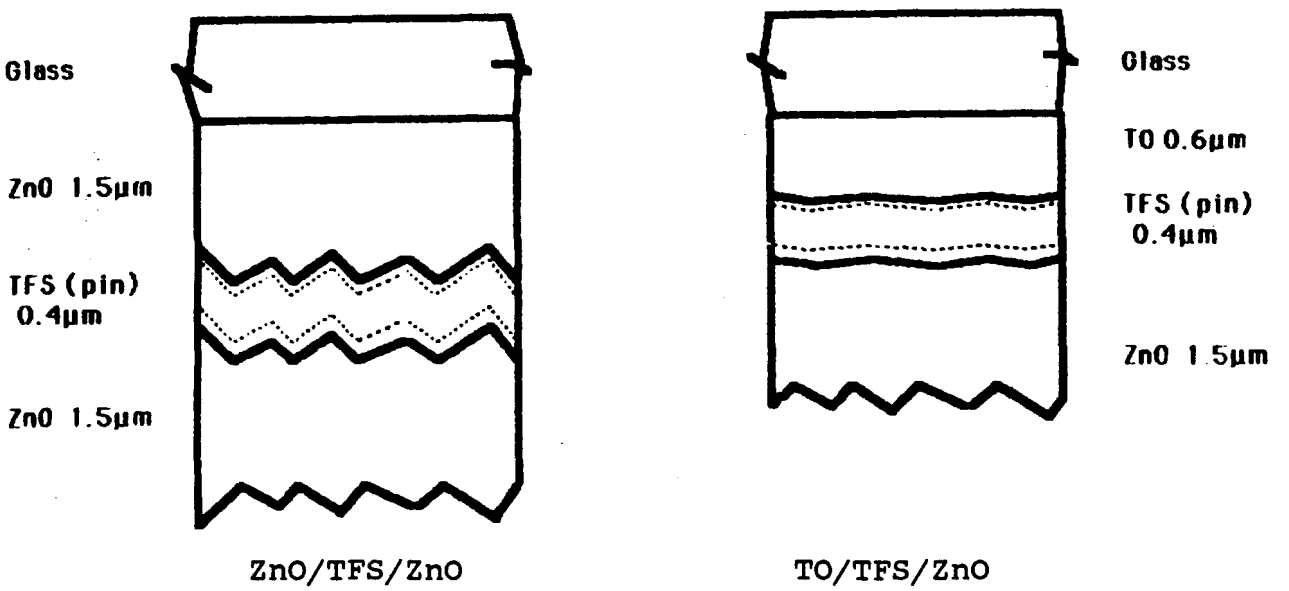

Fig. 1-1. Cross section of TFS cells.

gains in cell efficiency as shown in Fig. 1-2, where efficiency versus cell thickness is plotted for groups of cells with these two structures. (This is discussed in more detail below). The TO used in these experiments is the best commercially available. Its properties have been optimized in terms of overall commercial viability and not just in terms of a single property, such as texture, which might result in improved performance for small laboratory cells. The ZnO discussed here is also considered commercially viable, including highly textured samples.

Optical transmission of TO and ZnO films representative of those used in these devices is compared in Figs. 1-3 and 1-4. While transmission of the ZnO film is higher across the 300-1300 nm wavelength range of interest (despite its greater thickness), the improved current generation in the ZnO-based devices appears to be more a consequence of the favorable morphology of these films. In scanning electron micrographs (Figs. 1-5 and 1-6), ZnO films exhibit a much coarser surface texture than do TO films. (Additional analysis revealed these features to be rooted in columnar grains of corresponding size). A coarser surface reveals itself in a greater degree of "haze" or "milkiness" in the appearance of the film. This attribute can be quantified by appropriate optical measurements. One method uses a "Hazemeter" which allows average diffuse and total transmission to be measured. Figure 1-7 shows the roughly linear increase in TFS cell short-circuit current with increased diffuse transmittance of the ZnO front contact layer.

In addition to the impact of front contact morphology, other aspects of the cell structure can have important and interesting effects on current generation. A relative ranking of different cell structures is given in Fig. 1-8. While not directly relevant to tandem structures, it is interesting to note that substitution of a metal in place of ZnO for the back contact conductor of a TFS cell actually results in lower generated

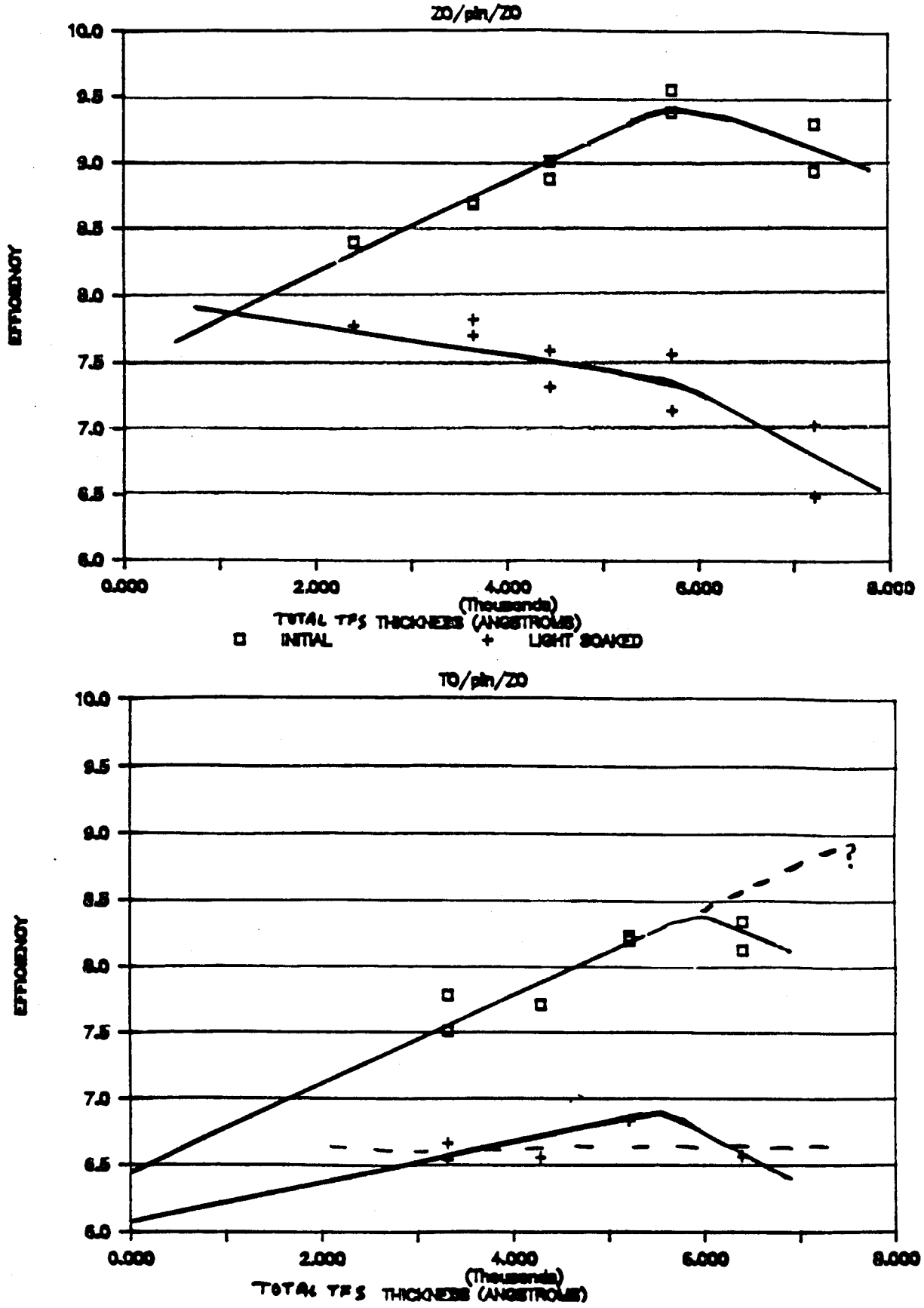

Fig. 1-2. Efficiency vs. thickness for ZnO (top) and TO (bottom).

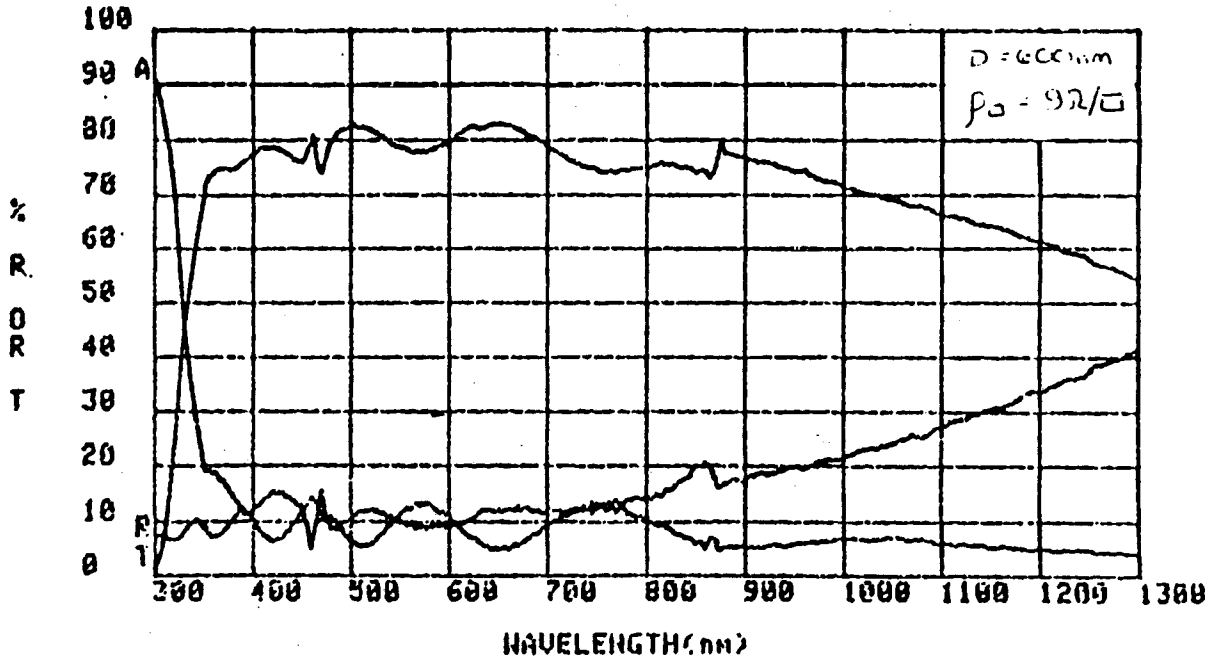

Fig. 1-3. Optical transmission of TO film.

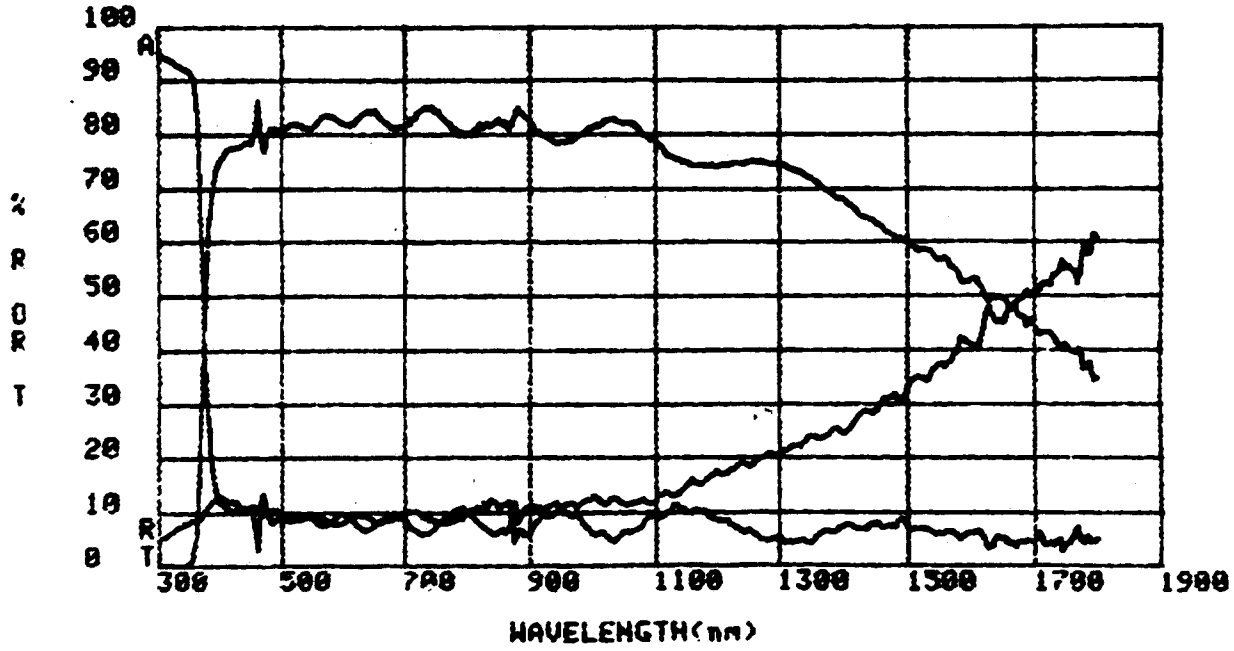

Fig. 1-4. Optical transmission of ZnO film.

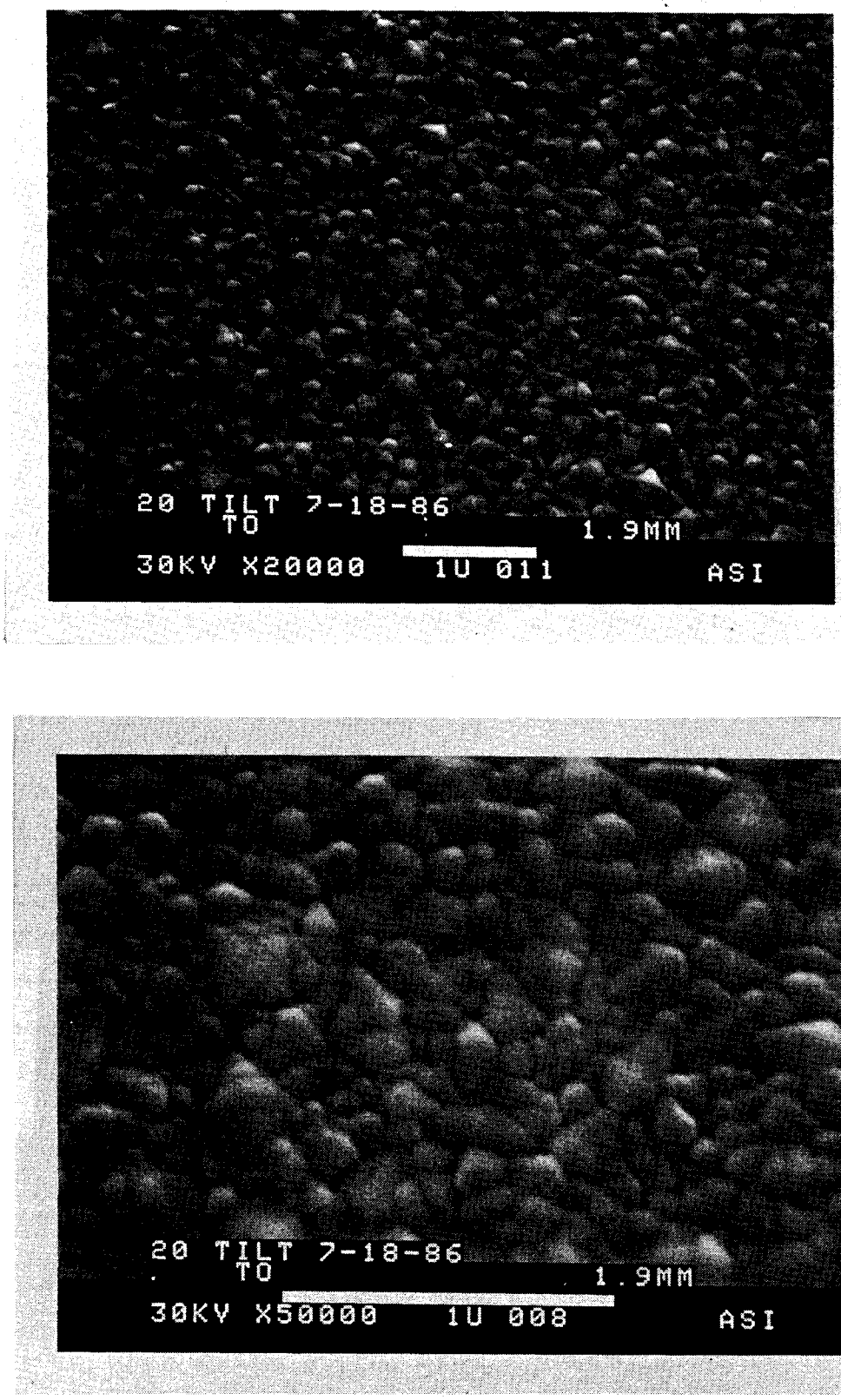

Fig. 1-5. Micrographs of TO film.

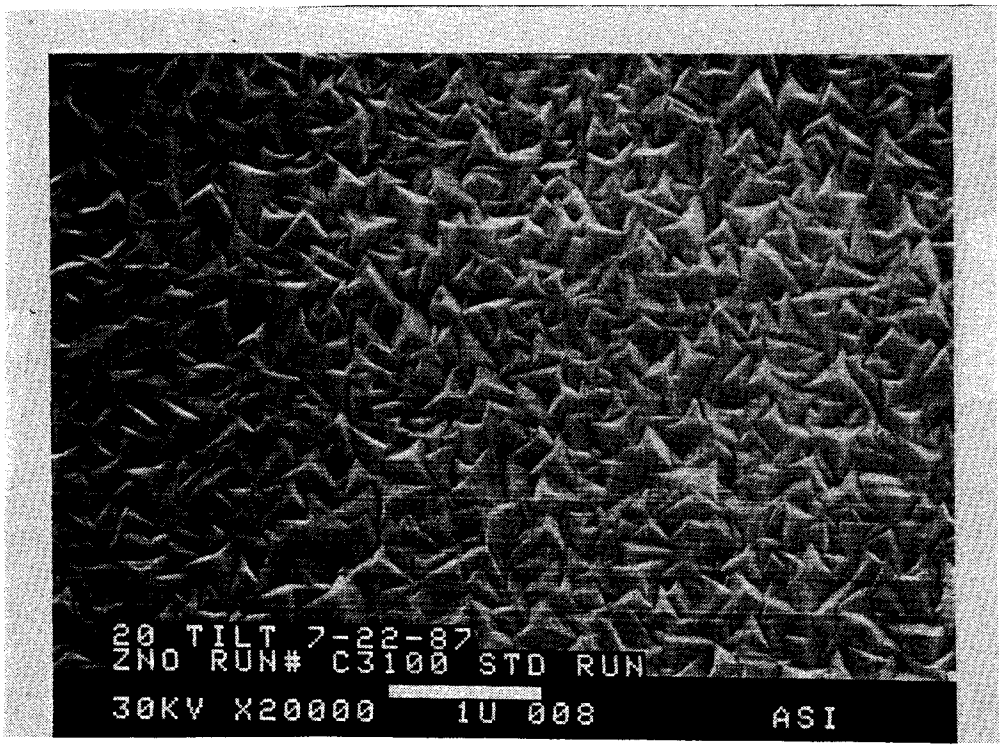

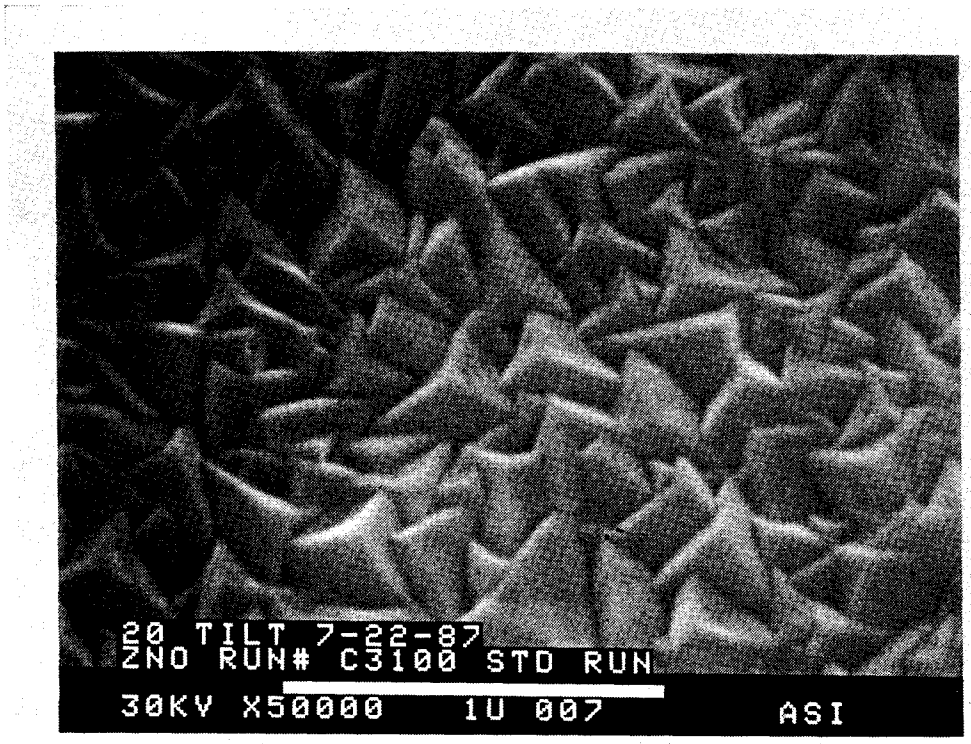

Fig. 1-6. Micrographs of ZnO film.

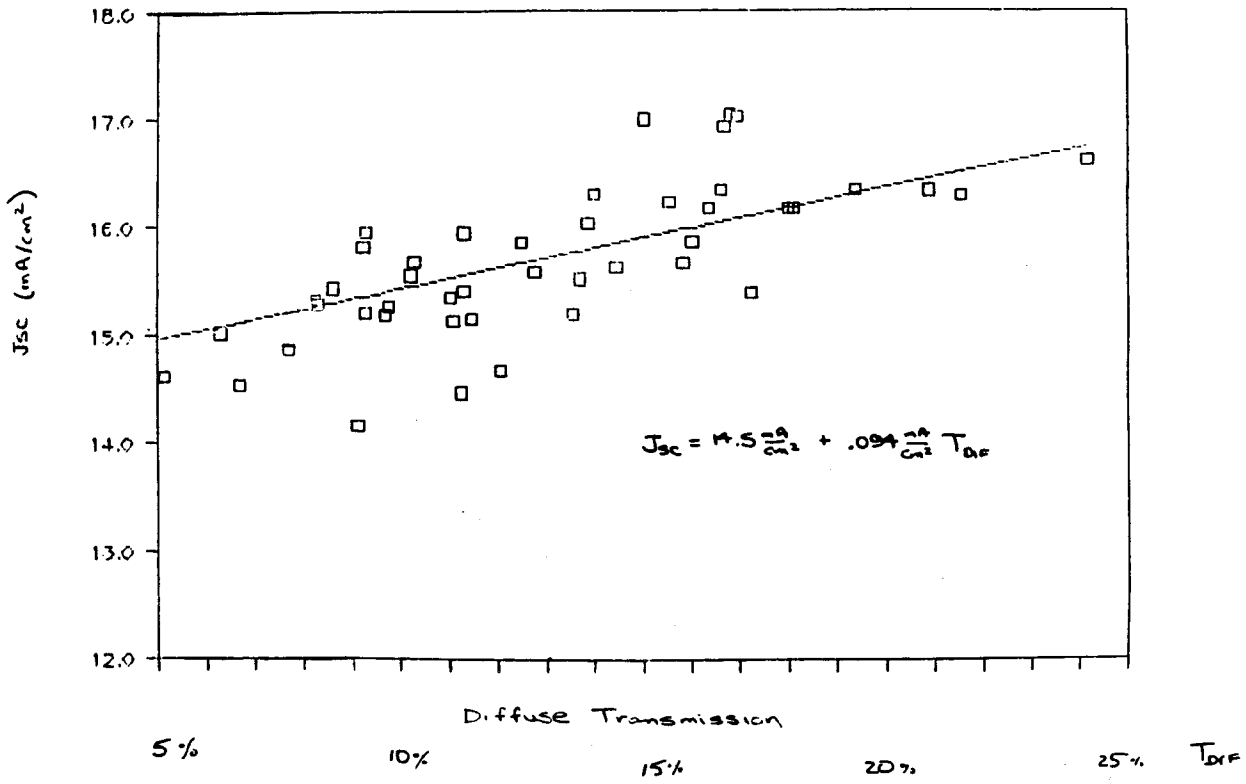

Fig. 1-7. Change in TFS J_{SC} vs. diffuse transmittance of ZnO.

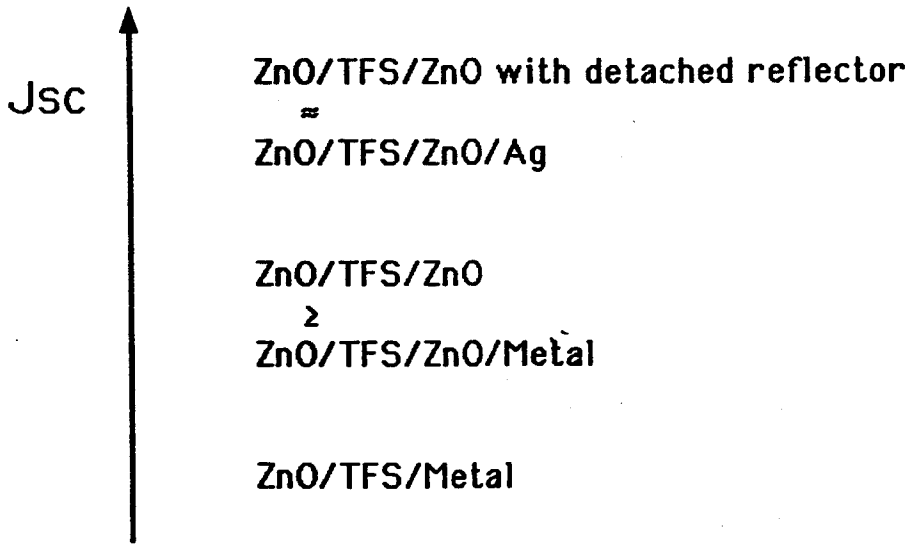

Fig. 1-8. Change in J_{SC} vs. cell structure.

current density. This is illustrated more quantitatively in Fig. 1-9, which shows cell performance parameters for a set of otherwise identical TFS cells with various back contacts: use of the "transparent" back results in more than 10% additional generated current (and 2-3% higher voltage). This result suggests that light trapping as well as scattering is an important mechanism for high current generation in ZnO/TFS/ZnO cells. The optical reflectance coefficient at a silicon/metal interface can be relatively low for many metals, resulting in a parasitic absorption loss which tends to suppress light trapping. This phenomenon is discussed by Martin Green in the context of concentrator cell structure [1].

The new zinc oxide/TFS/zinc oxide structure has provided some significant opportunities. Progress toward optimizing these structures is presented in the next section.

1.2.2 Optimization of TFS Cell Structure

The thicknesses of the component layers were varied systematically in order to examine performance sensitivity to these changes and to allow for device optimization.

1.2.2.1 Cell Performance vs. Zinc Oxide Layer Thickness

Two separate groups of devices were fabricated in order to assess independently the sensitivity to changes in the front and rear contact layer thicknesses; all other device parameters were held constant while each contact was varied.

In the first group the front contact ZnO thickness was varied from 0.7 μm to 1.5 μm (the rear ZnO thickness was fixed at 1.5 μm). Results are presented in Fig. 1-10. Performance is insensitive until front ZnO thickness is reduced below 1.0 μm, when a reduction in generated current and poorer curve fill factor (FF) result. The poorer fill factor is caused by increased device series resistance, indicated by the strong increase in shape at V_{OC} (S_{OC}).[1] Both of these observed changes are accounted for by changes in properties of the ZnO layer with thickness. Thinner ZnO has a finer grain structure leading to both reduced optical haze and poorer conductivity. It is interesting to note that cell performance is unaffected by changes in sheet rho in the thicker films (these are between 20 and 8 ohms/□). Since the geometry of current transport is similar in test cells and submodules, similar insensitivity can be anticipated for submodules. (The average current transfer length is actually somewhat -- about 10% -- greater in the submodule).

In the second group the rear contact ZnO thickness was varied from 0.7 μm to 1.5 μm (the front ZnO thickness was fixed at 1.5

---

[1]See Section 1.7 for definitions of S_{SC} and S_{OC}.

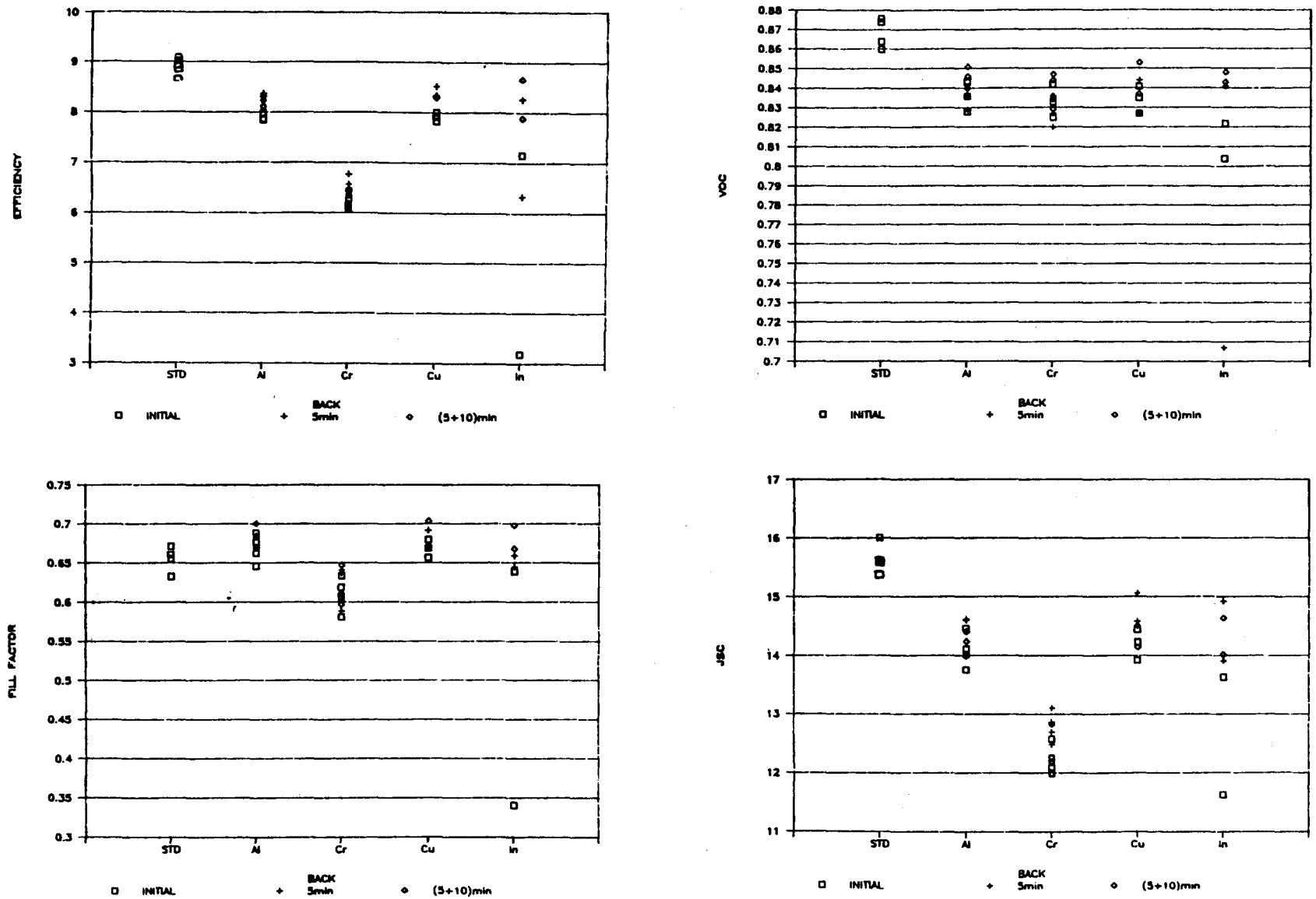

Fig. 1-9. Change in TFS cell performance vs. change in back contact. Cells are ZnO/TFS(pin)/contact. Contacts are STD (ZnO), Al, Cr, Cu and In. Each point is an average of up to 16 cells. Anneal time (@175^{o}C in air) is shown for metal contacts.

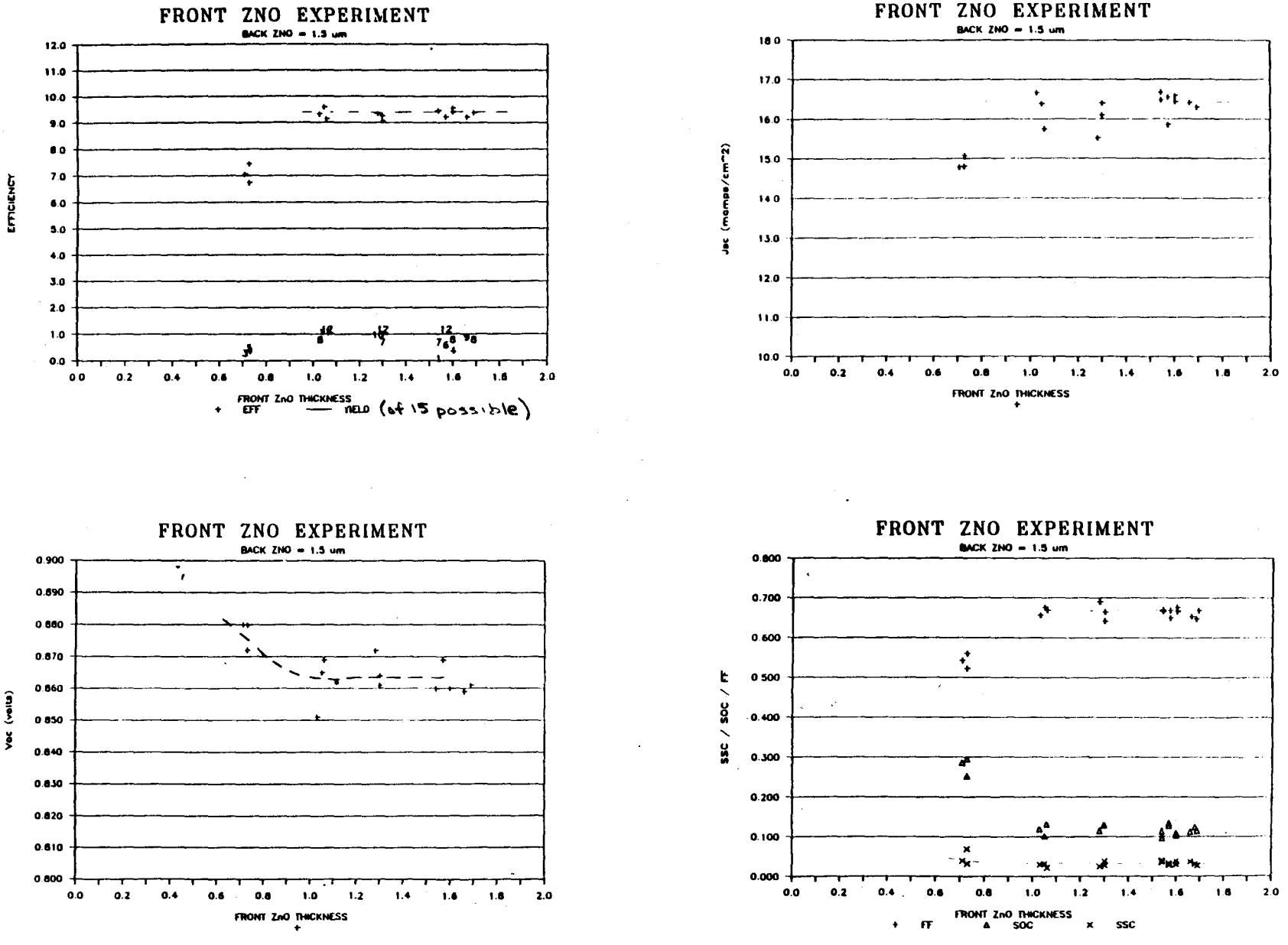

Fig. 1-10. Effect of changing front contact ZnO thickness.

μm). Results are presented in Fig. 1-11. Performance is entirely independent of this parameter except for some variation in fill factor, which is discussed below. In particular it is worth noting that the generated current density is independent of changes in rear ZnO thickness and optical haze.

The variations in observed fill factor are enmeshed in a subtlety of measurement technique. Since the rear ZnO layer does not readily make ohmic contact to electrical probes, an additional contact bus is applied to each cell (unlike submodules). Contact of this printed silver epoxy bus to the ZnO can contribute very significant series resistance. Measurement can be made "two-point" with current and voltage probes both applied to the bus, or it can be made "four-point" with the current probe on the bus and the voltage probe on the ZnO layer immediately adjacent to the bus. Either method has potential for error:

Two-point: the "external" contact resistance is lumped into the measurement of the cell; true cell performance is under-estimated.

Four-point: while the "external" contact resistance is removed from the measurement of the cell, the true cell voltage at load, i.e. fill factor, is overestimated by the magnitude of voltage drop through the ZnO sheet between the probe point and the bus. Normally this is completely negligible. However, if the sheet resistance of the rear ZnO layer is sufficiently great, e.g. greater than 20-30 ohms/□, then this error can be significant and true cell performance overestimated.

Thus, the two methods provide lower and upper bounds to the true cell fill factor. In the case of this group the "four-point" measurements begin to be somewhat suspect for rear ZnO thickness at and below 1.0 μm. The conclusion of this analysis is that true variations in cell fill factor with rear ZnO thickness are small (less than 0.02-3 fill factor units, and possibly zero).

1.2.2.2 Cell Performance vs. TFS i-Layer Thickness

TFS i-layer thickness is a dominant variable determining cell performance and stability. Two separate groups of devices were fabricated -- one with ZnO and one with TO front contacts -- in order to compare the sensitivity to changes in the i-layer thickness in the range 200-700 nm for these two device structures. i-layer deposition rates were in the range of 1-2Å/sec for this study. Initial and 20-hour light-soaked cell parameters are plotted in Figs. 1-12 through 1-17. (Preliminary analysis of the stabilized[2] performance of these cells indicates a continuation of the "20 hour" trends. These results will be discussed in more detail in a later report.)

---

[2]See Section 1.4 for a discussion of stability.

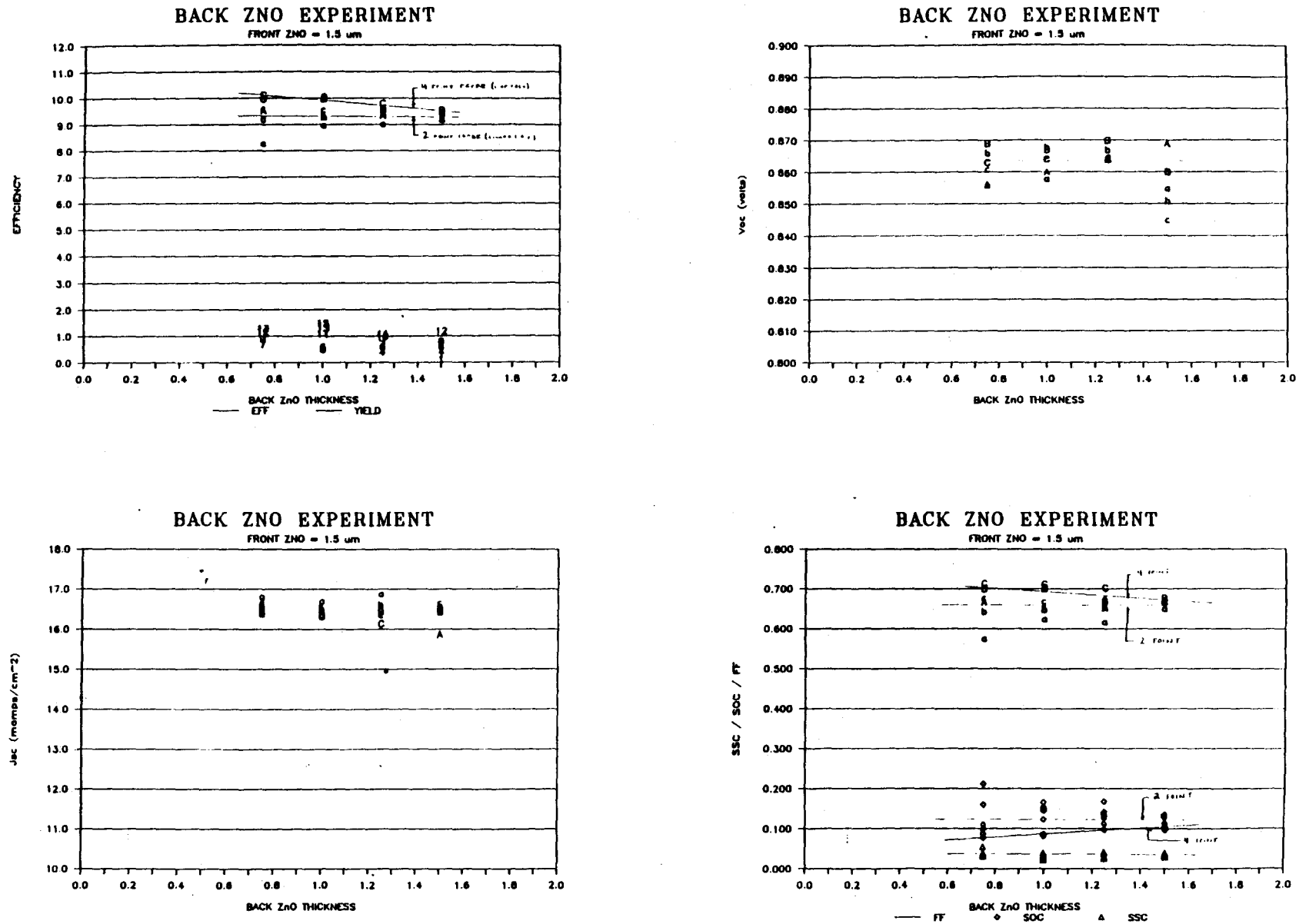

Fig. 1-11. Effect of changing rear contact ZnO thickness.

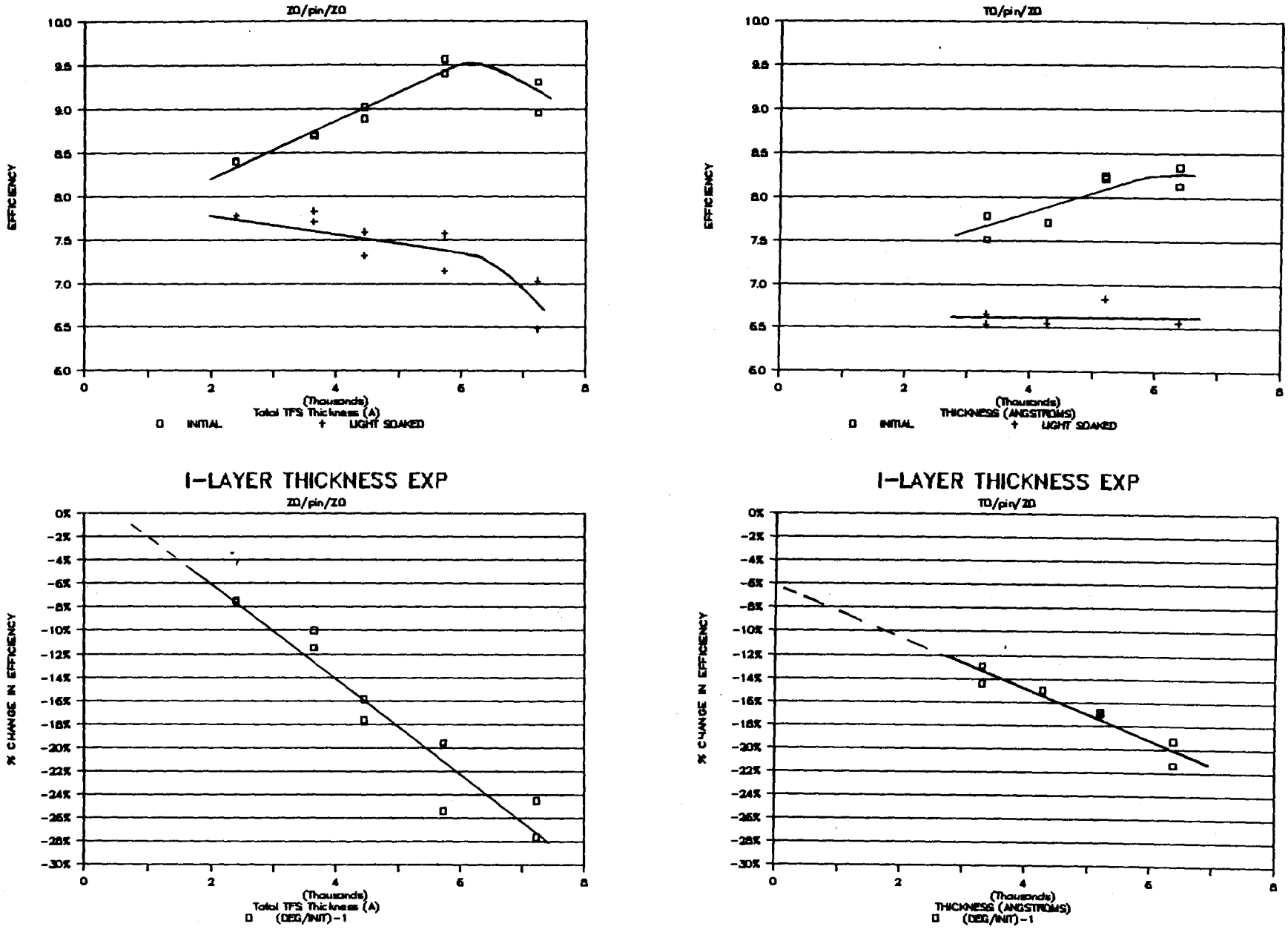

Fig. 1-12. Effect of i-layer thickness on efficiency for (left) ZnO/TFS/ZnO cells and (right) TO/TFS/ZnO cells.

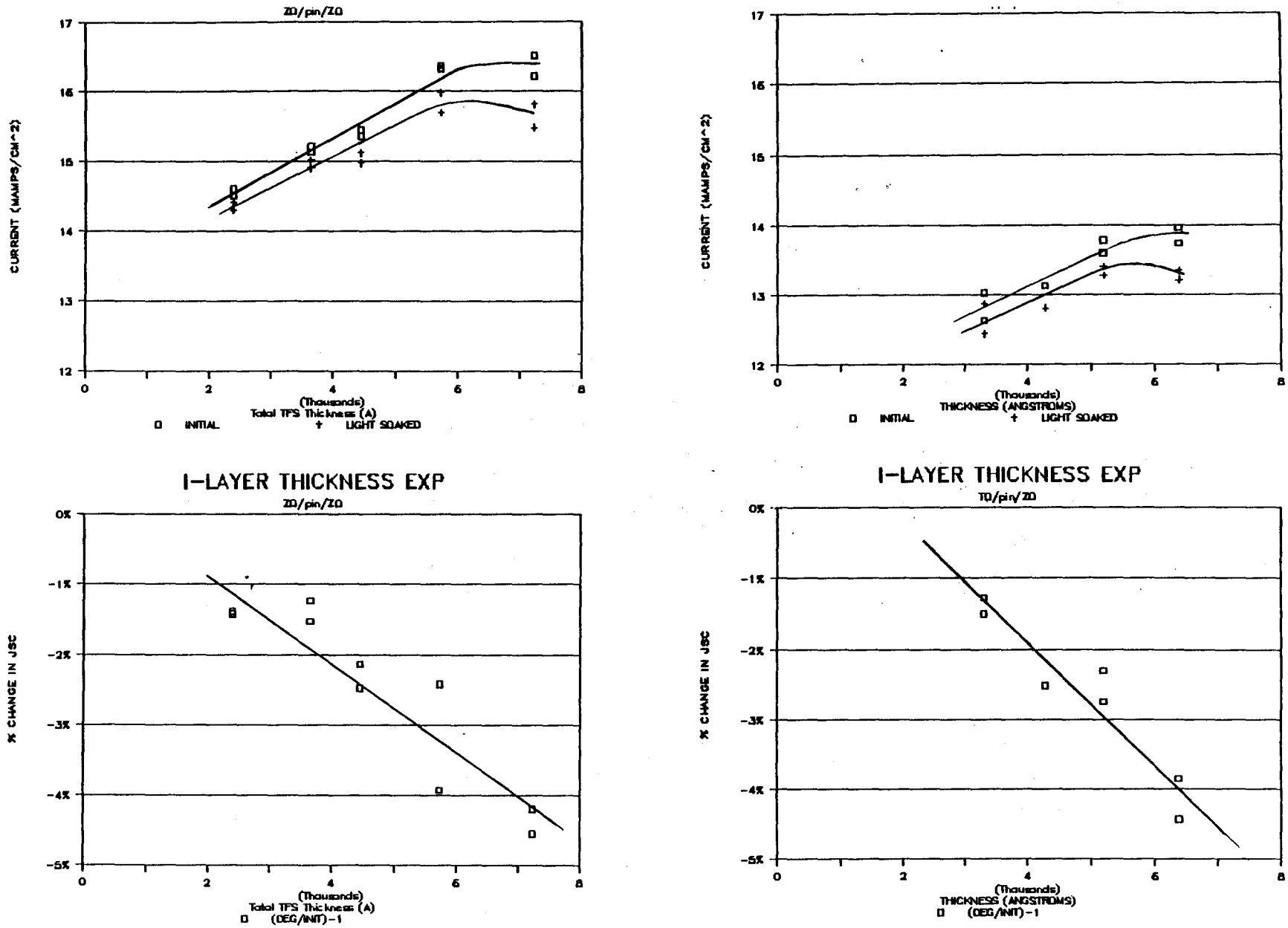

Fig. 1-13. Changes in current for (left) ZnO/TFS/ZnO cells and (right) TO/TFS/ZnO cells.

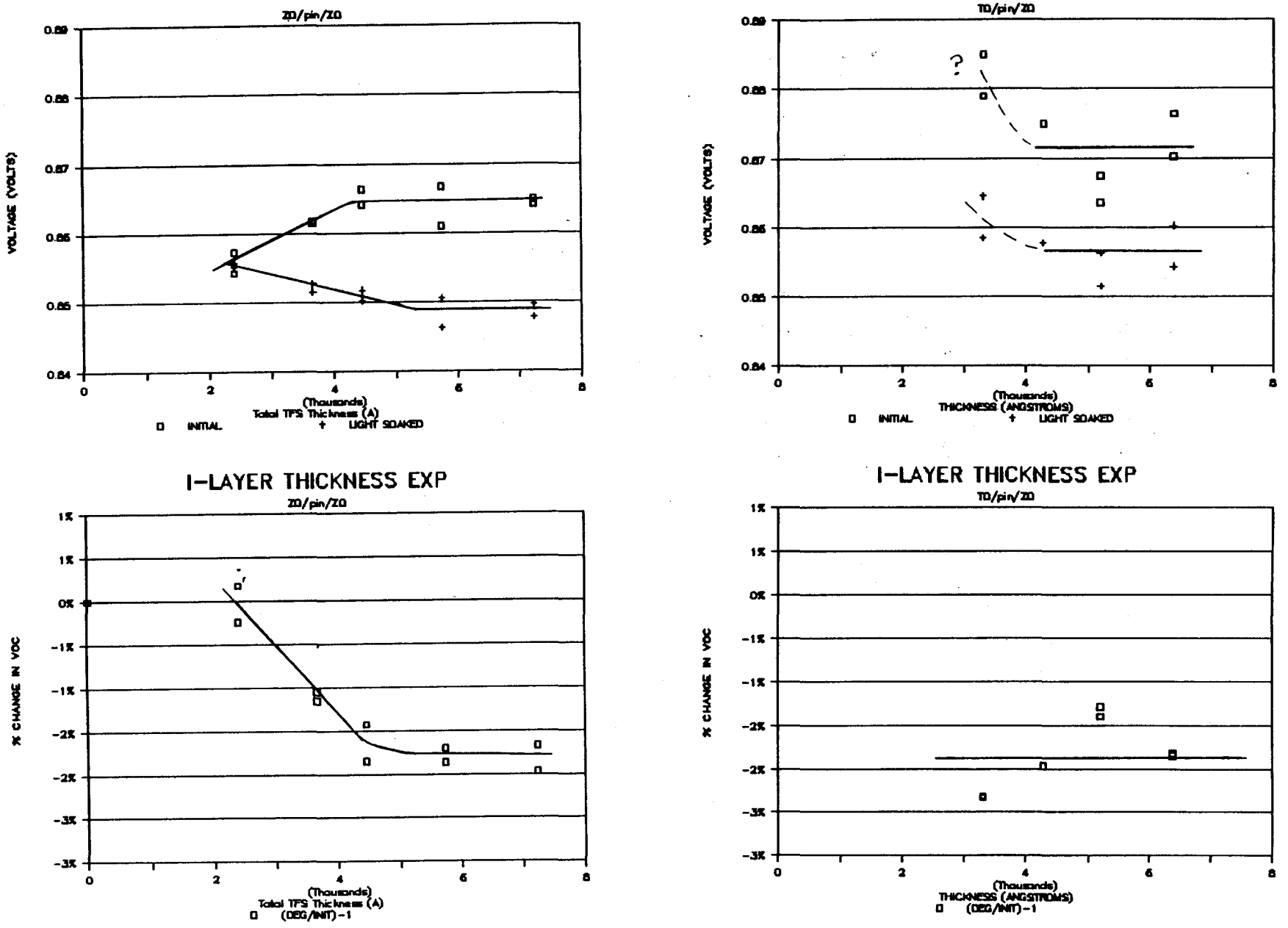

Fig. 1-14. Changes in voltage for (left) ZnO/TFS/ZnO cells and (right) TO/TFS/ZnO cells.

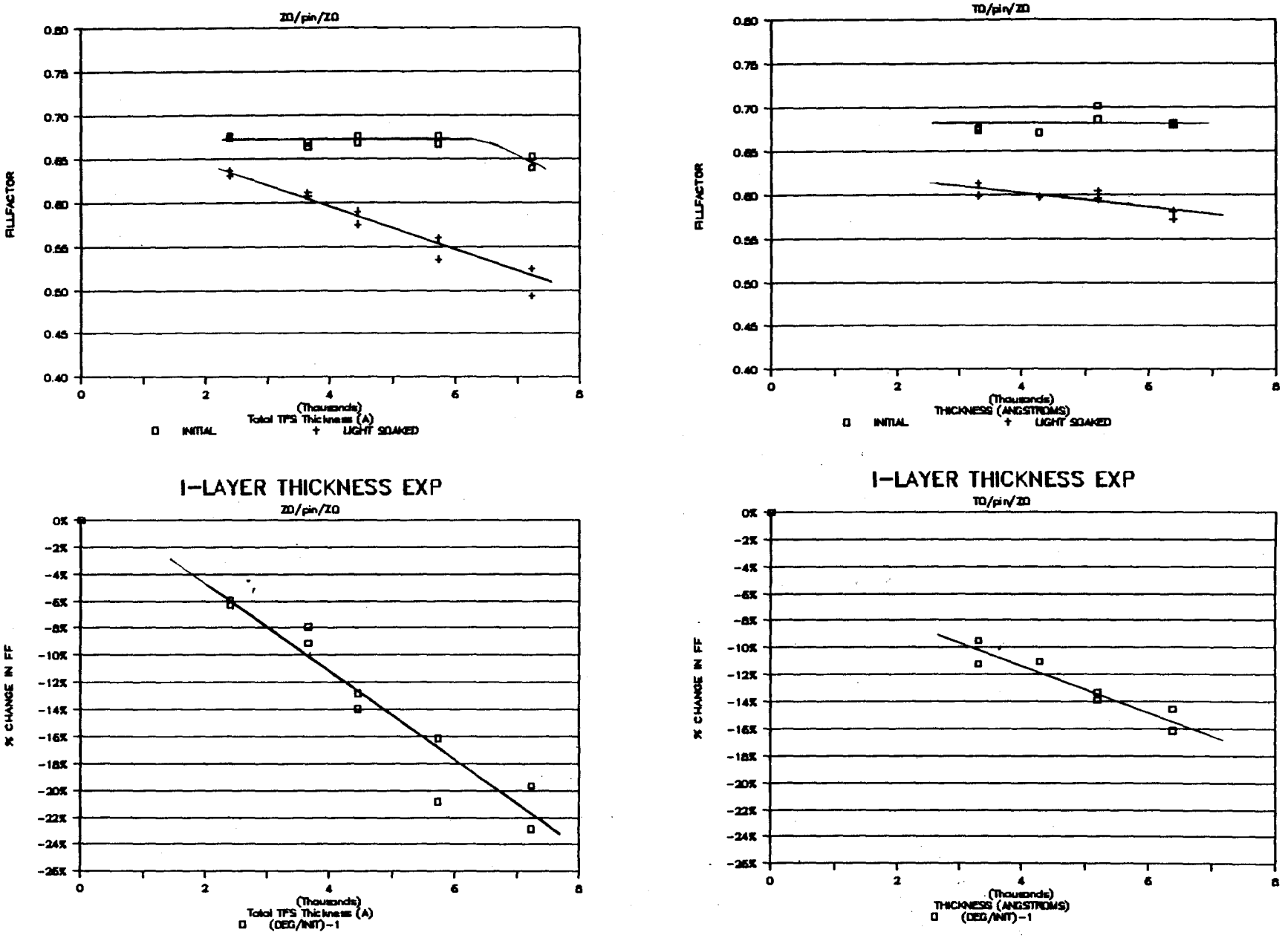

Fig. 1-15. Changes in fill factor for (left) ZnO/TFS/ZnO cells and (right) TO/TFS/ZnO cells.

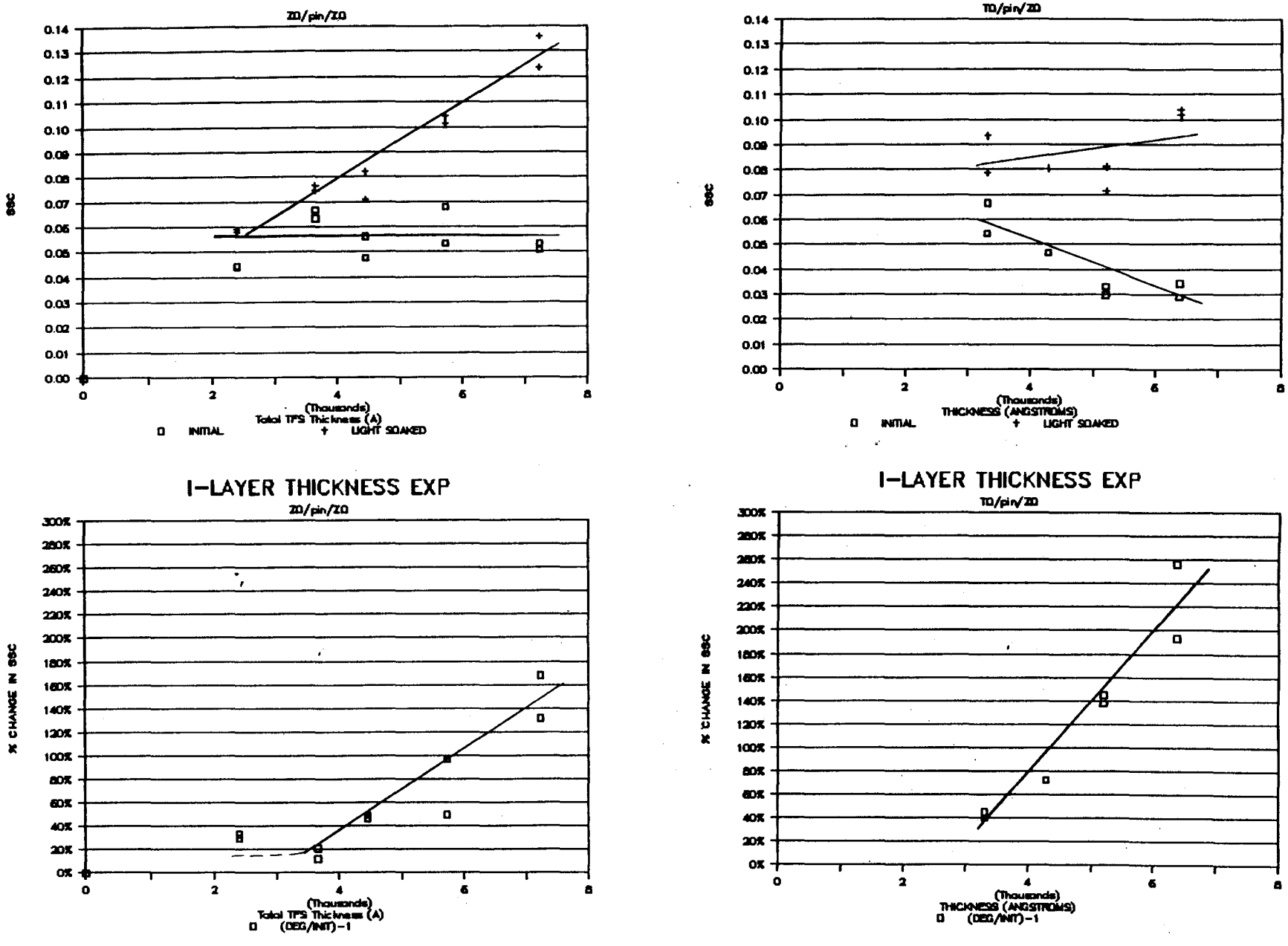

Fig. 1-16. Changes in shape at J_{SC} (S_{SC}) for (left) ZnO/TFS/ZnO cells and (right) TO/TFS/ZnO cells.

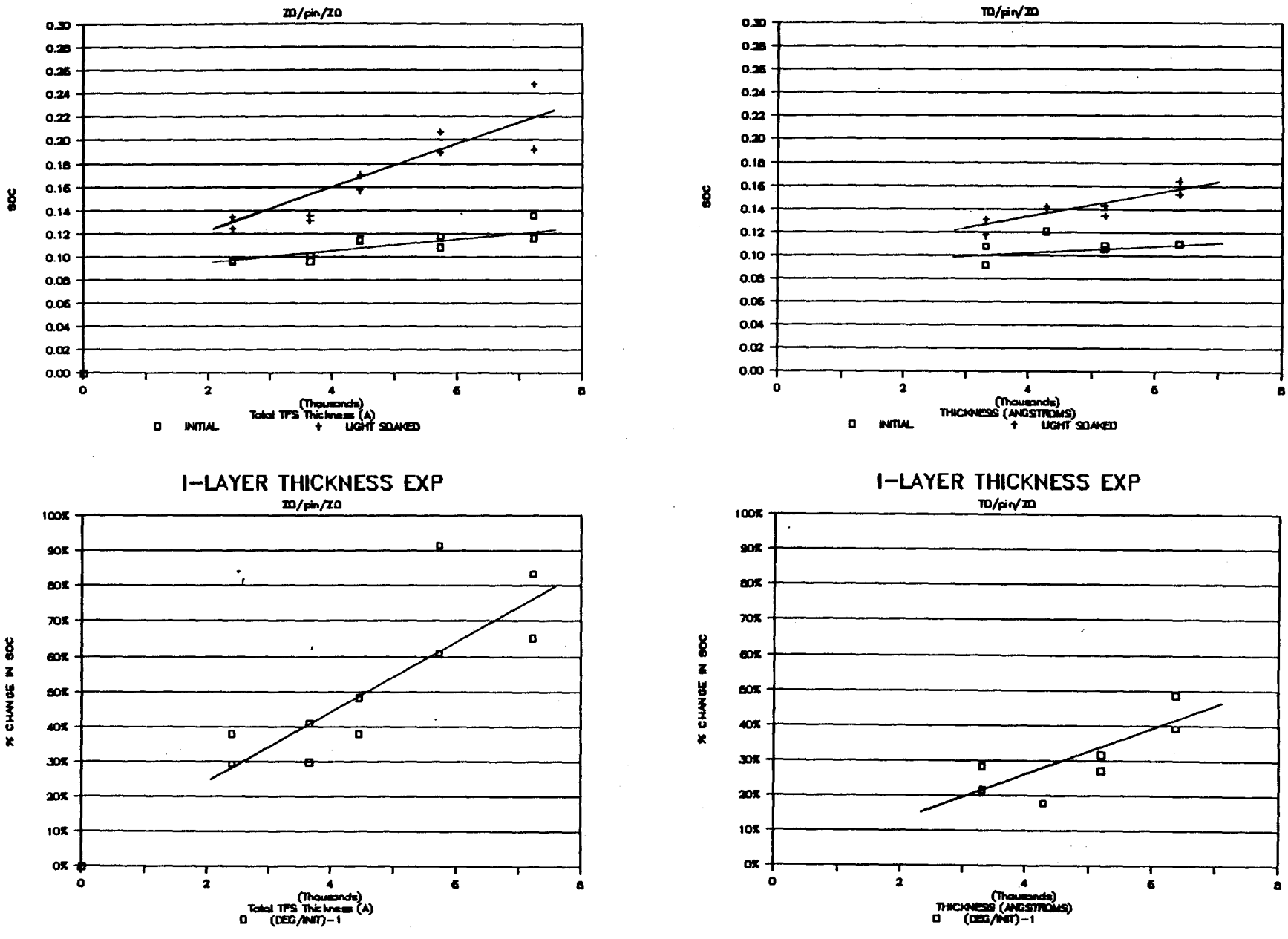

Fig. 1-17. Changes in shape at V_{OC} (S_{OC}) for (left) ZnO/TFS/ZnO cells and (right) TO/TFS/ZnO cells.

Overall efficiency is illustrated in Fig. 1-12. Performance of ZnO/TFS/ZnO cells is more strongly leveraged by i-layer thickness than is that of the TO/TFS/ZnO cells, and is dominated by strong changes in generated current (Fig. 1-13).

In contrast, variations in cell voltage are small (Fig. 1-14). While trends may exist, the range of changes is less than 2-3% and may more reflect variations in cell preparation. To first order V_{oc} is constant for these cells, with TO-based cells exhibiting perhaps slightly higher values than ZnO-based cells. One consistent trend is that cells with higher initial voltages tend to experience the largest loss in voltage, i.e. light-soaked TFS cell voltage tends toward a common range.

Initial cell fill factor is the same for all cells except perhaps for those with the thickest i-layer (Fig. 1-15). In contrast, light-soaked fill factor is strongly dependent upon i-layer thickness and, as expected, dominates the losses. ZnO-based cells show a stronger dependence than TO-based cells; this may be a function of their overall higher current generation density. The shapes at J_{sc} (S_{sc}) and V_{oc} (S_{oc}) in Figs. 1-16 and 1-17 indicate the contribution to fill factor behavior by the shunt-like and series-like components respectively.

Two points from Fig. 1-12 are especially noteworthy:

1. For today's TFS material 300-350 nm is the optimal i-layer thickness for highest light-soaked efficiency for either device structure.

2. Comparison of "% Change in Efficiency" permits different inferences about the nature of stability losses in the two device structures. If projected to zero bulk i-layer thickness, TO-based cells would exhibit a residual loss while ZnO-based cells would be completely stable. This suggests that ZnO-based cells avoid a non-bulk, possibly interface, stability loss that is present in TO-based cells -- an interesting clue in the photostability problem.

1.2.2.3 Cell Performance vs. p+ Layer Thickness

The TFS p+ layer is a key component of the cell, intimately involved in the active junction. This study aimed at determining cell performance sensitivity to variations in p+ layer thickness. This was of special interest because of the significant difference in texture, and possibly coverage requirements, of ZnO and TO.

The standard p+ was varied in thickness from 0 to 400 Å for two separate groups of cells: one group the new ZnO/TFS/ZnO and the other a conventional TO/TFS/aluminum structure. Results are compared in Fig. 1-18. A first observation is that the trends are essentially the same for the two structures, suggesting that the cell junction is not significantly different. Moreover, the

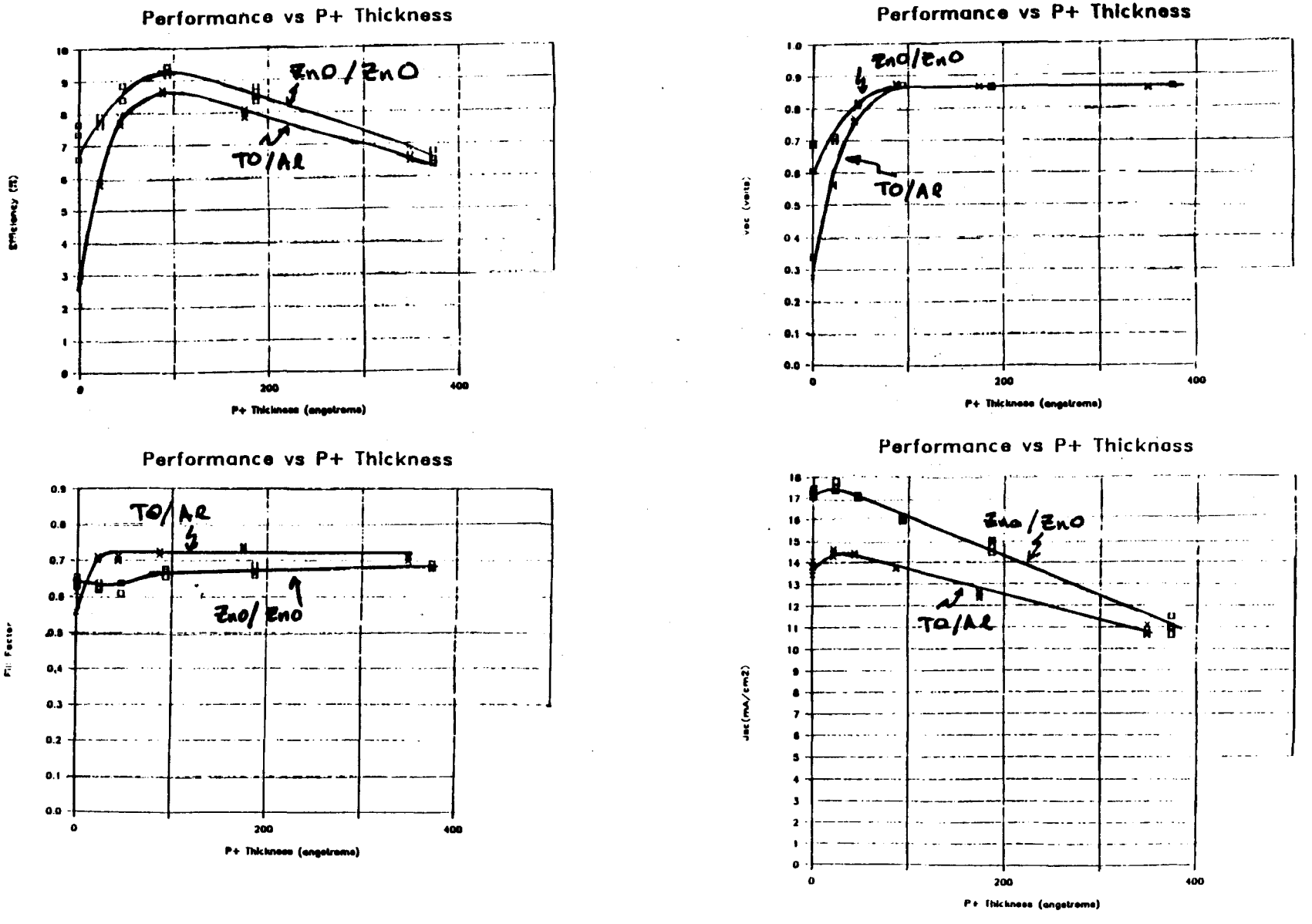

Fig. 1-18. Effect of changes in p+ thickness on performance of ZnO/TFS/ZnO and TO/TFS/aluminum cells.

100 Å optimum thickness is not sharply peaked -- variations of 20% to 30% result in less than 5 parts per hundred change in cell efficiency -- a result of the balance between voltage and current generation. As expected, the ZnO/TFS/ZnO cells generate higher current densities, but otherwise the differences are not especially significant. (In this comparison the ZnO/TFS/ZnO cells have consistently lower fill factor than the conventional TO/TFS/Al cells, but subsequent development work, e.g. use of enhanced microcrystallinity n+ layers, has raised the fill factor of the ZnO/TFS/ZnO cells to about the same level).

One final point is particularly interesting: cell fill factor is independent of p+ thickness from 50 Å up to 400 Å, implying that losses due to p+ bulk resistance must be negligible. This is further suggested by the constant values of S_{OC} in this range shown in Fig. 1-19. This conclusion has two corollaries:

1. Any photoinduced loss in p+ conductivity is unlikely to have an impact on cell performance.

2. High performance reported for cells with highly conductive enhanced microcrystallinity p+ probably does not derive, per se, from reduced bulk p+ resistance. This suggests an altered junction in these reported devices.

1.2.3 Enhanced Microcrystallinity Doped Layers

1.2.3.1 n+ Layers

High bulk dark conductivity -- about 10 $(ohm\text{-}cm)^{-1}$ -- n+ layers have been achieved. Conductivity is most of all a strong function of RF power density, but can be somewhat enhanced by

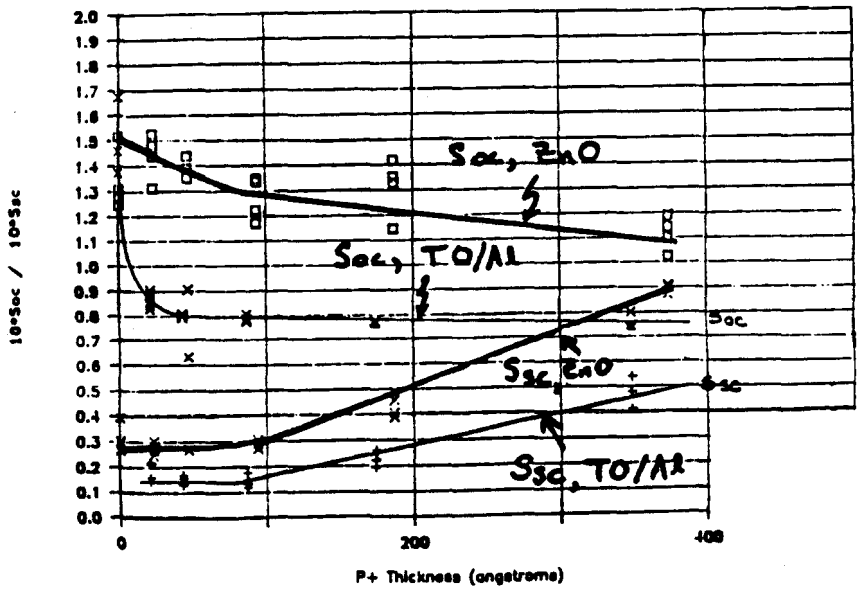

Fig. 1-19. Effect of changes in p+ thickness on shape at J_{SC} (S_{SC}) and shape at V_{OC} (S_{OC}) for ZnO/TFS/ZnO and TO/TFS/Al cells.

fuel flow depletion and/or by addition of argon to the fuel mix (silane, hydrogen, and phosphine). Conductivity and deposition rate versus relative RF power density are illustrated in Fig. 1-20. Four different fuel conditions are represented: a low (150 sccm) and a high (450 sccm) fuel flow rate, both with (1/1) and without the addition of argon. The use of argon did allow peak conductivity at lower power levels, but also resulted in an undesirable level of dust generation and deposition non-uniformity. Normal deposition fuel mixes did not suffer from these drawbacks but did require the highest power level to obtain the peak conductivity.

The use of enhanced microcrystallinity n+ yields a reduced series resistance and improved fill factor when compared to otherwise identical cells which use a conventional n+ layer. The performance is independent of n+ thickness in the range 200-800 Å. The gain is useful but relatively small, about 0.02-0.03 (e.g., an increase in fill factor from 0.67 to 0.69-0.70). That this gain is not observed in "conventional" cells with aluminum back contacts indicates that the n+/back-contact contact resistivity is dependent on the resistivity of both materials.

Figure 1-21 shows the gradual variation in cell performance with n+ conductivity. (A range of n+ growth conditions was used in preparation of this set.)

1.2.3.2 p+ Layers

High bulk conductivity p+ layers have also been achieved. The conductivity and Tauc optical gap are contrasted with those of a "standard" p+ in Fig. 1-22. These values compare favorably with those cited in the literature in association with very high voltage TFS cells. However, high cell voltages have not yet been obtained through the use of these doped layers.

1.3 TFS SUBMODULE PERFORMANCE PROGRESS

TFS submodules are fabricated on 30×30 cm glass plates. These monolithic integrated circuits cover an approximately 850 cm^2 aperture area and contain 50 individual series connected cells.

The best modules perform at a level close to that which can be projected from the average performance of test cells which are "witnesses" to the modules. These devices all have a "standard" structure using a 350 nm thick TFS i-layer. There are two main sources of loss in going from cell to module:

1. Module I_{sc} is limited by the active fraction of the circuit area; this is controlled by interconnect dead area losses. Typical interconnects by two different patterning methods are shown in Figs. 1-23 and 1-24; both figures illustrate the three pattern lines necessary for circuit integration. These figures also demonstrate the significant gains in active area possible with laser patterning techniques.

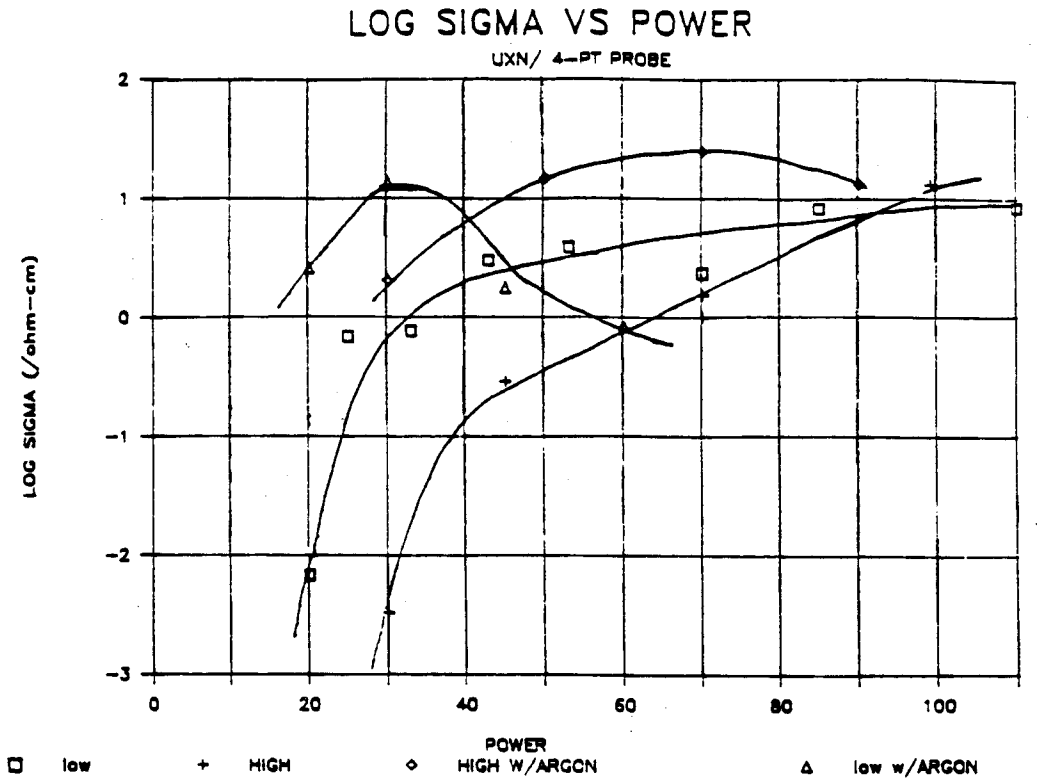

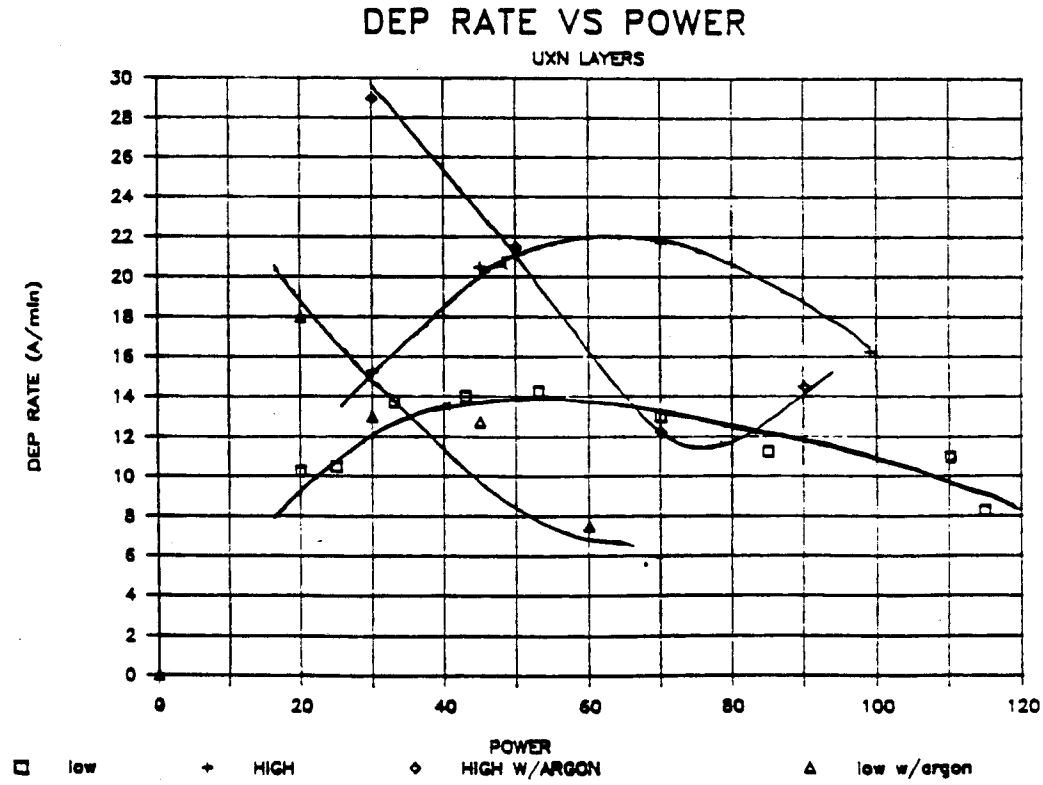

Fig. 1-20. Dark conductivity and deposition rate vs. relative power density.

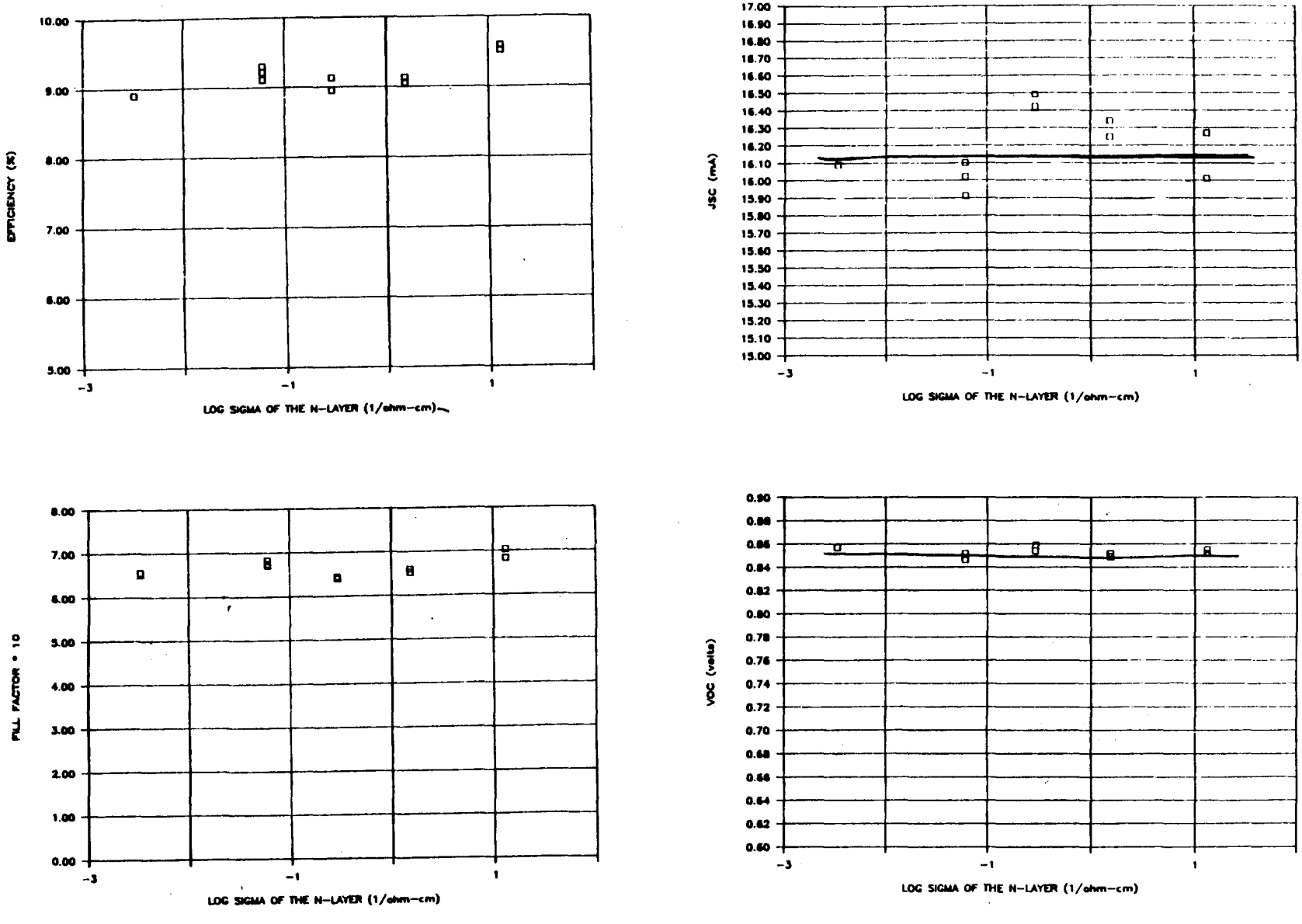

Fig. 1-21. Changes in cell performance and n+ conductivity.

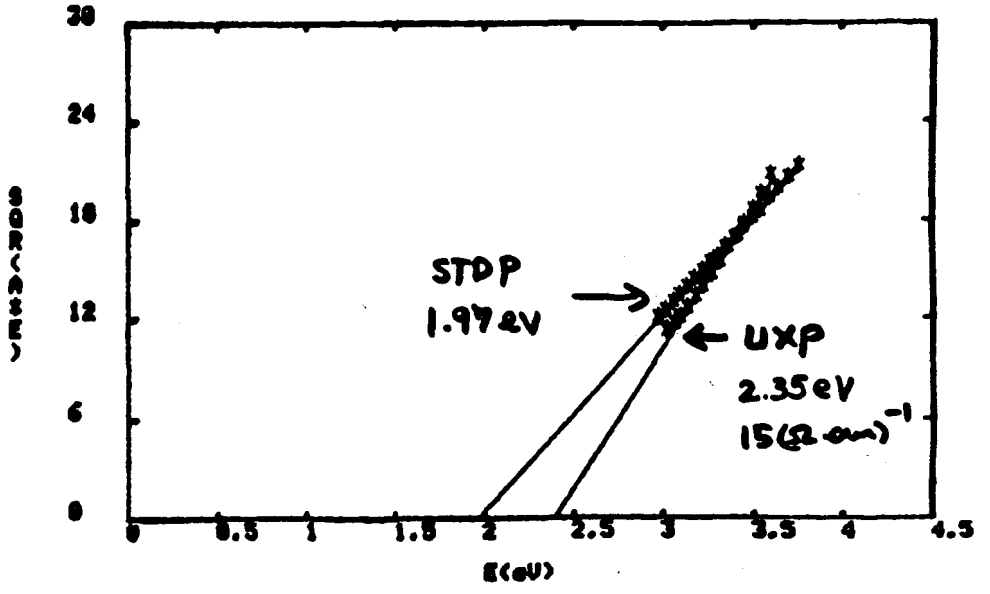

Fig. 1-22. Tauc optical band gap of p+ layers.

2. Module fill factor is reduced from cell fill factor due to less favorable current collection geometry; this series resistance loss is limited by the sheet resistance of the ZnO layers. For these devices this loss will be approximately 3-5%. (The model that allows quantitative assessment of this loss is discussed in more detail elsewhere.)

The average measured performance of the "witness" cells is:

V_{oc} = 860 mV
J_{sc} = 16.1 mA/cm^2 Efficiency = 9.7%
FF = 0.70

Taking account of the loss terms discussed above, the expected module performance can be <u>projected</u>:

V_{oc} = 860 mV	x 50		= 43 V
I_{sc} = 16.1 mA/cm^2	x 17 cm^2	x 0.91-0.98	= 250-268 mA
FF = 0.70	x 0.95-0.97		= 0.66-0.68

Aperture Efficiency = 8.3-9.2%

These projections can be seen to agree well with measured module performance illustrated in Figs. 1-25 and 1-26.

(As an additional point of interest these modules were tested with a white rear reflector, a configuration that could be used if a tandem module were not desired or needed. This simple reflector enhances current generation about 10%.)

1.4 TFS DEVICE STABILITY STATUS

It is widely recognized that the stability of TFS devices is not only dependent on the device structure and preparation but also

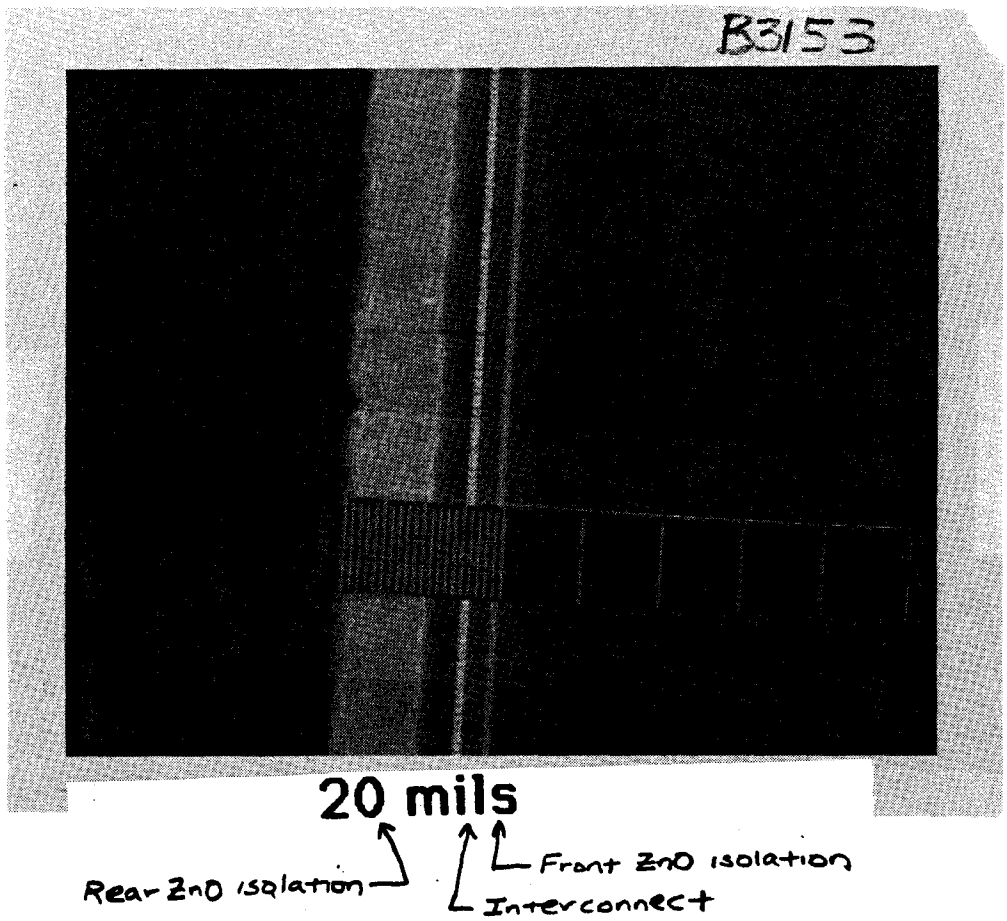

Fig. 1-23. Laser/print patterning. Total cell width = 0.227 in. Active fraction = (0.227 in. - 0.020 in.)/0.227 in. = 91%.

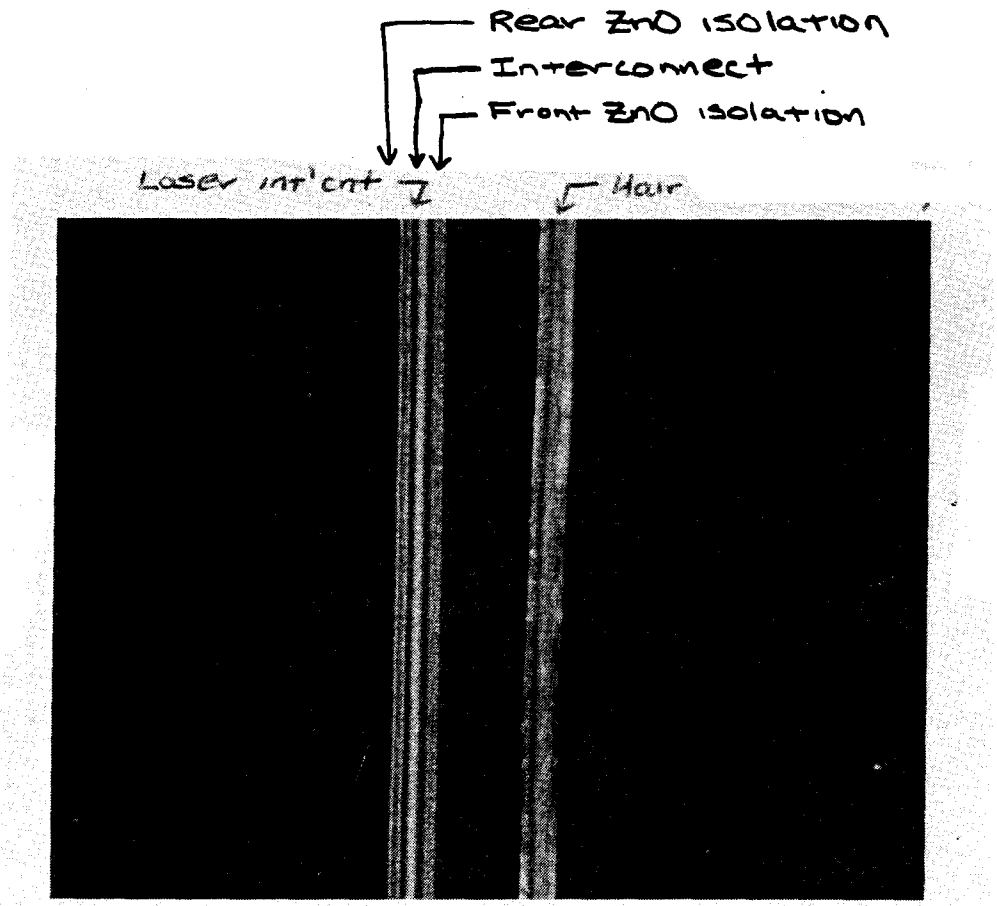

Fig. 1-24. All laser patterning. Total cell width = 0.227 in. Active fraction = (0.227 in. - 0.005 in.)/0.227 in. = 98%.

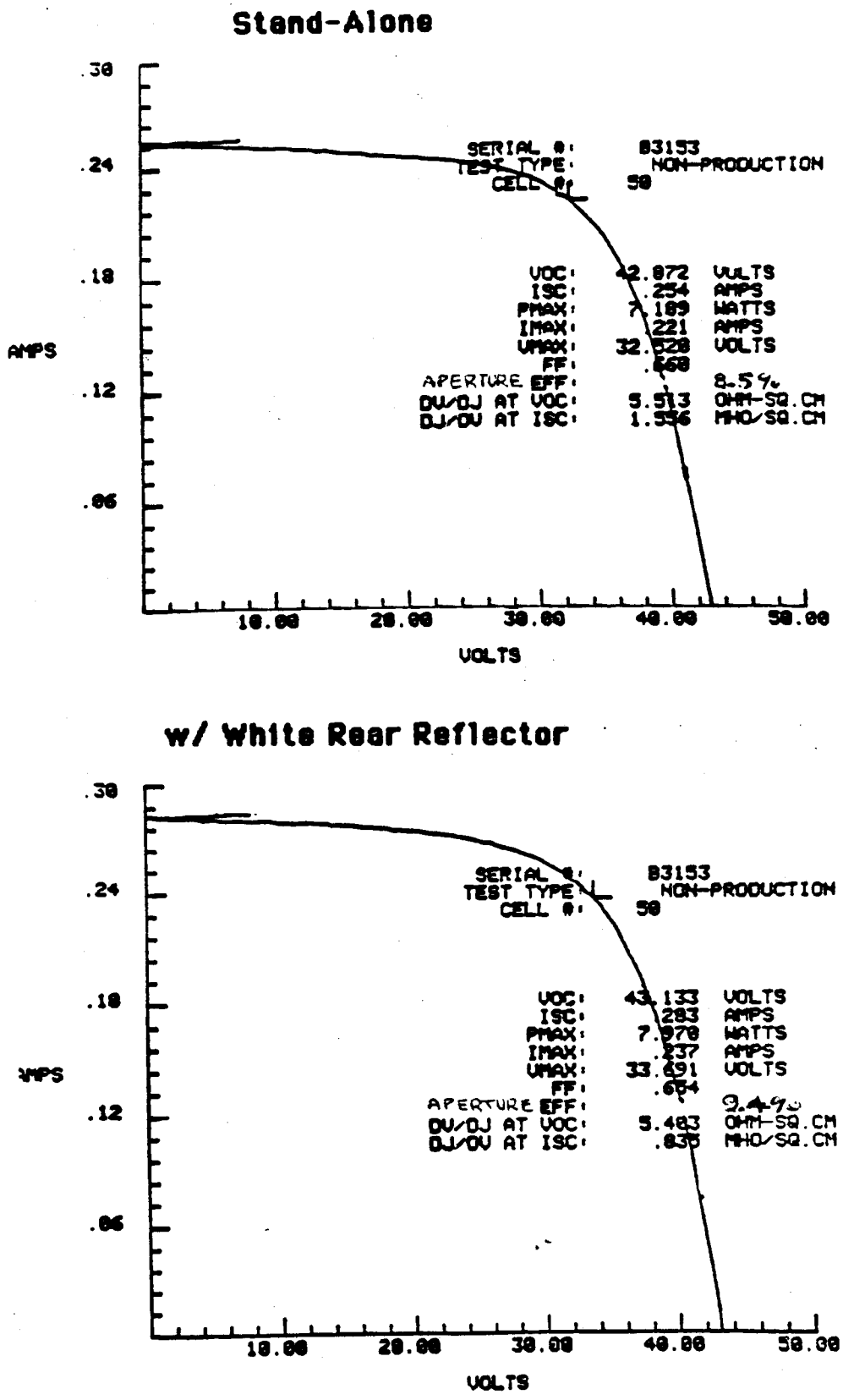

Fig. 1-25. Measured performance of module with laser/print patterning in stand-alone configuration (top) and with white rear reflector (bottom).

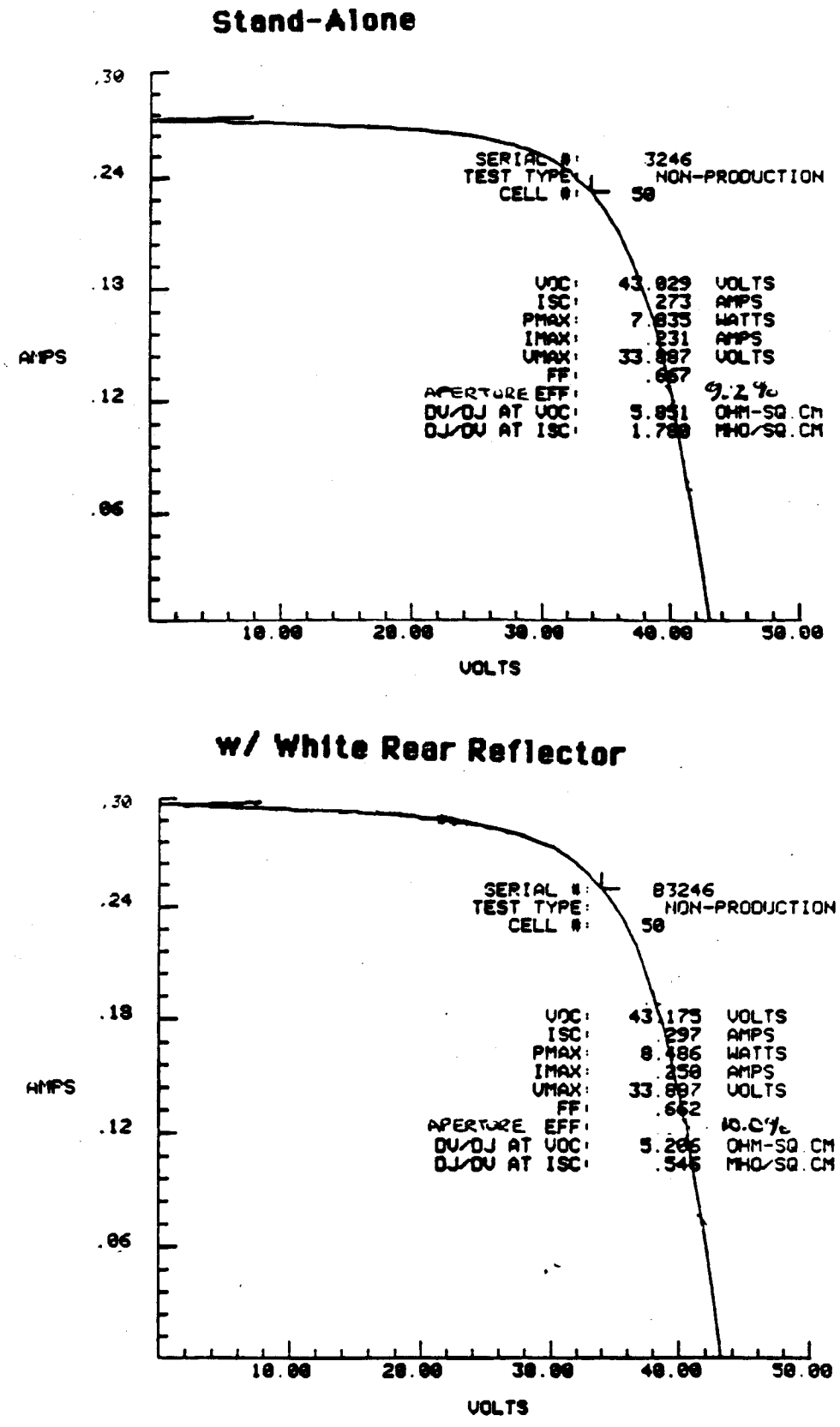

Fig. 1-26. Measured performance of module with all laser patterning in stand-alone configuration (top) and with white rear reflector (bottom).

strongly upon the exposure environment, particularly upon the ambient temperature. For experimental convenience, an arbitrary but reasonable and self-consistent exposure method has been employed at ARCO Solar. The standard exposure cycle is:

20 hours @ 1 sun/50°C in a xenon Weather-ometer
4 hours @ dark rest/25°C

The 4-hour dark rest period also allows for device test after each cycle if desired. Typically this simulated exposure will be repeated for up to 10 consecutive cycles in order to define the steady-state "stabilized" performance attributes of a device.

Figure 1-27 illustrates this for two groups of "standard" cells. About three-quarters of the total drop is realized in the first light soak cycle, and steady state is reached after about five cycles. Standard cells with 350 nm TFS i-layers lose about a fifth (20 "points") of their initial performance.

The stability of devices is monitored on a regular basis. Over a three-month period consistent behavior was observed:

ZnO/TFS(pin)/ZnO cells: Steady state loss = 21 +/- 3 points (18 groups)

TO/TFS(pin)/Al cells: Steady state loss = 20 +/- 2 points (8 groups)

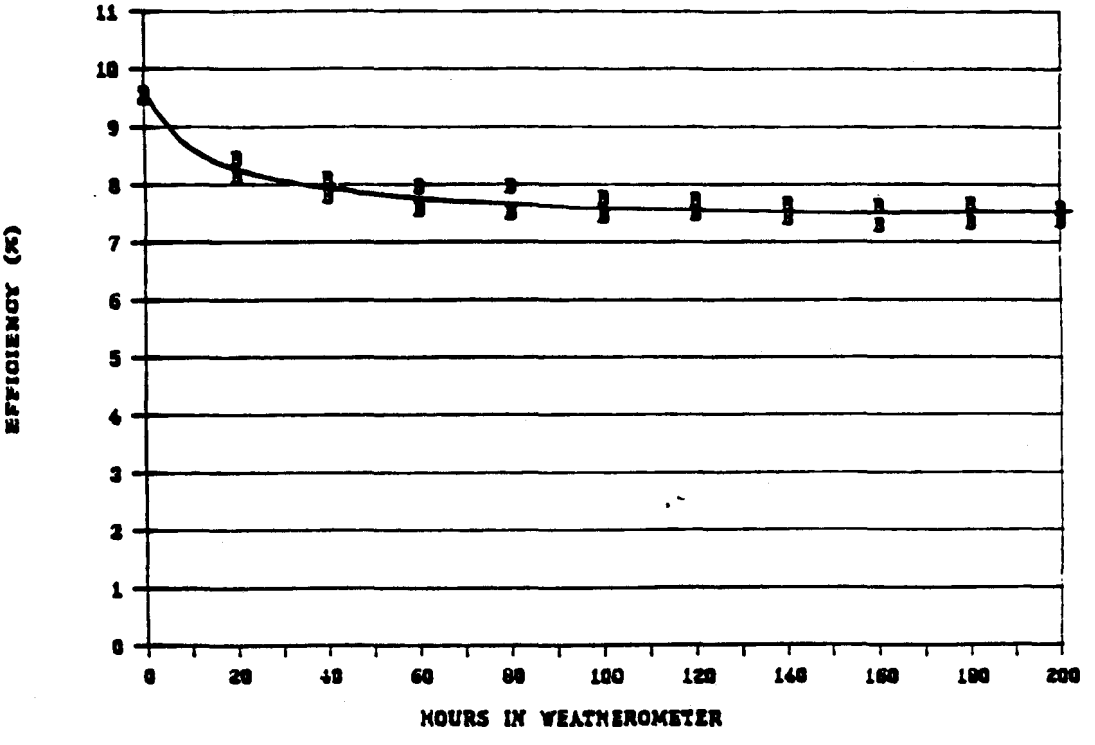

Fig. 1-27. Stability of standard ZnO/TFS(pin)/ZnO cells after standard exposure cycle.

The typical observed loss from initial performance consists of:

V_{oc}: 2 points
J_{sc}: 5 points Total = 100 x (1-0.98•0.95•0.86) = 20 points
FF: 14 points

Efficiency and fill factor data for representative examples of test cells and of 50-cell submodules are illustrated in Figs. 1-28 and 1-29, respectively; all exhibit the same behavior. (A note: in these groups of devices some were light soaked with a black background and some with a white background in order to test for incremental loss from a reflector. All were tested without reflector).

The results of this simulated environment generally agree well with the results of "real world" exposure, where "real world" is defined by the Chatsworth, California, insolation and climate.

Figure 1-30 shows output power and fill factor data for two groups of 50-cell modules exposed outdoors; the 17-22 point drop supports the "reasonableness" of the Weather-ometer testing. (As might be anticipated, devices exposed in the "real world" stabilize more favorably in the warm summer and less favorably in the cool winter; results of spring and fall exposures show better agreement with those from simulated exposure.)

1.5 TFS DEVICE TANDEM FILTER QUALITY

Since these TFS devices are intended to be one component of a tandem module it is important to have a method to characterize their transmission characteristics. One useful method defines the measurement of "Relative Filter Quality":

$$\text{Relative FQ} = J_{sc}(\text{int;filtered}) \,/\, J_{sc}(\text{int;unfiltered})$$

J_{sc}(int) is the calculated current density of a chosen standard CIS reference cell, determined by integrating its measured quantum efficiency with the SERI standard solar spectrum. Relative FQ of any TFS device is determined by making this CIS spectral response measurement first without ("unfiltered") and then with ("filtered") the TFS device in place over the CIS cell.

This method allows any TFS device to be characterized, on a self-consistent relative basis, in terms of the fractional response that it allows for the underlying CIS device. However, of course, in any given tandem device the absolute value of the fraction will depend on the spectral response of the specific CIS device and will vary.

Section 1.2 explored the sensitivity of TFS cell performance to changes in structure and layer thickness. Figure 1-31 illustrates the impact of those changes on relative filter quality.

The thickness of the front ZnO layer is the key variable and shows the most dynamic range of FQ values. While not revealed in

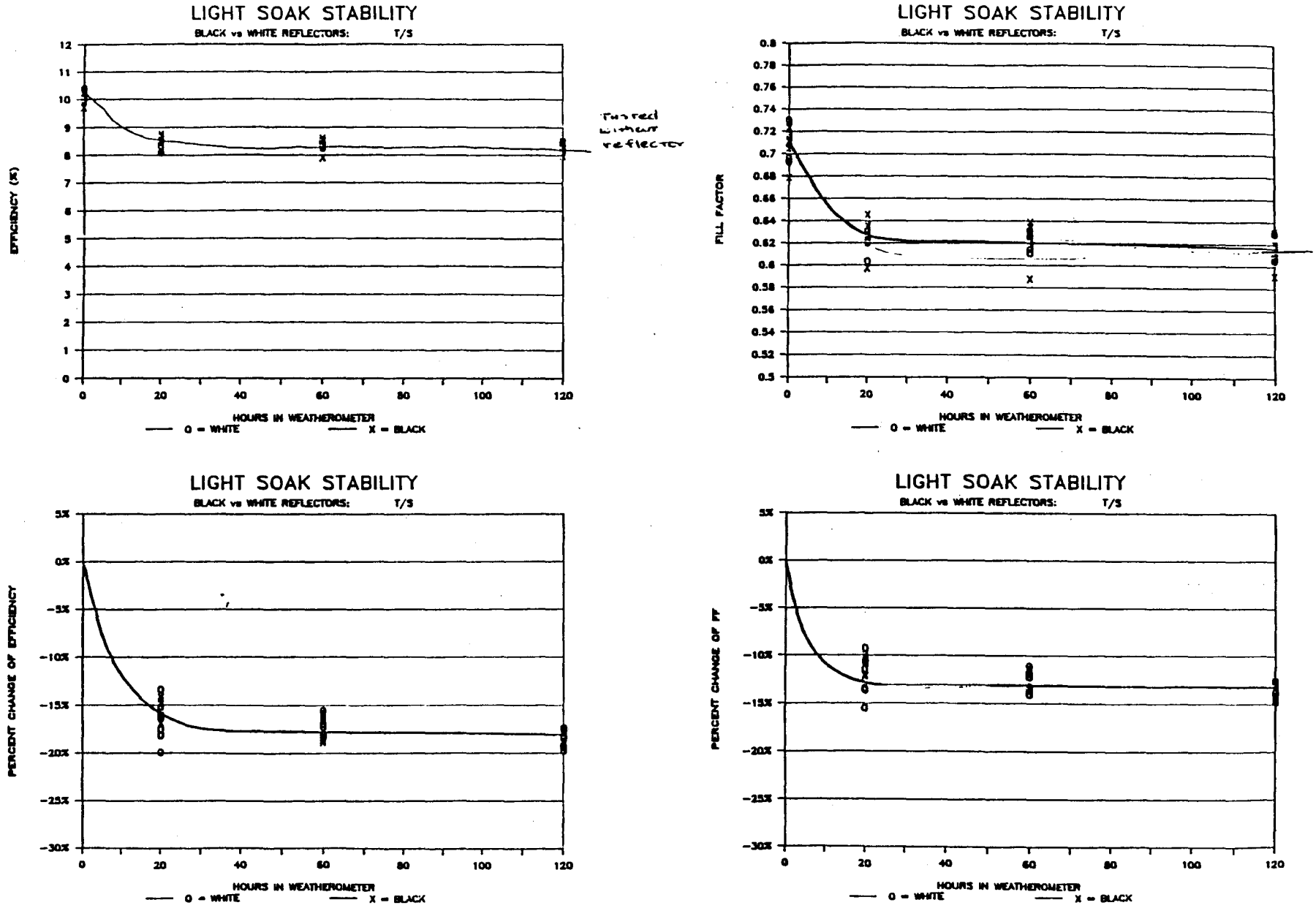

Fig. 1-28. Efficiency and fill factor stability for test cells in simulated environment.

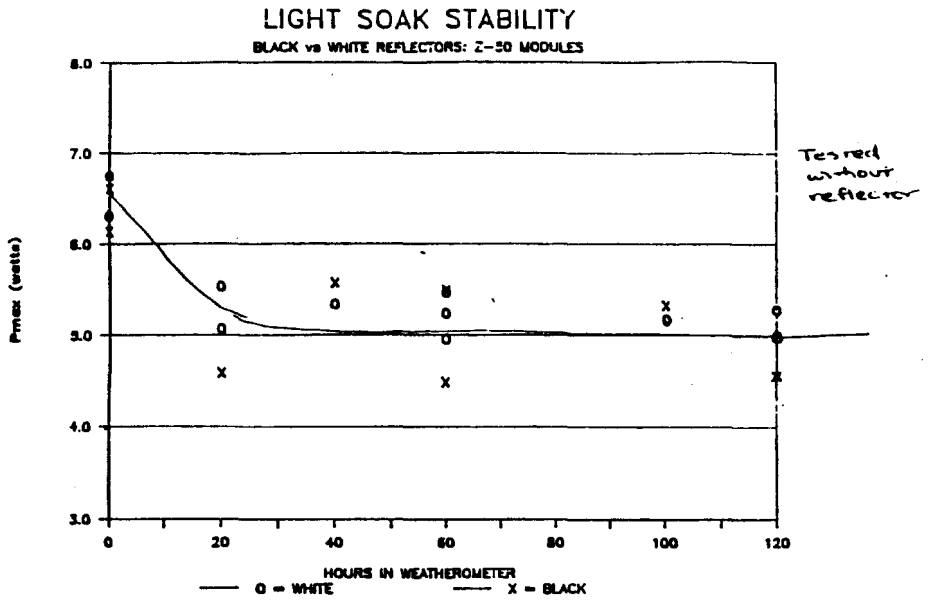

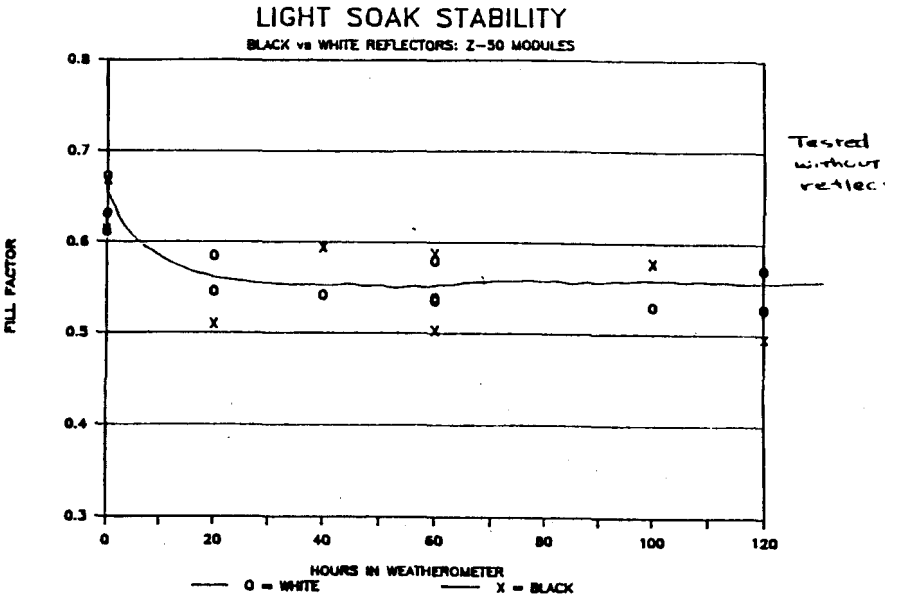

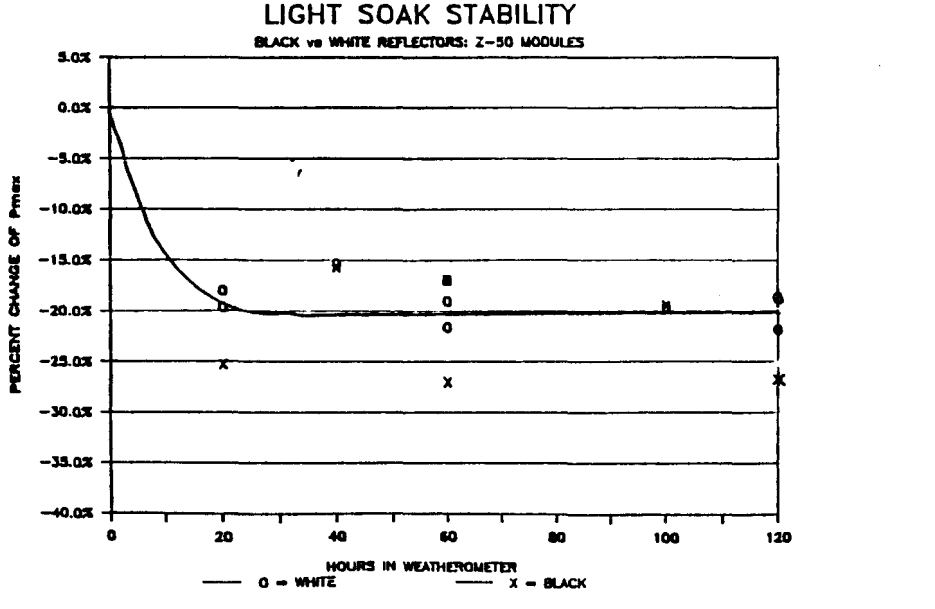

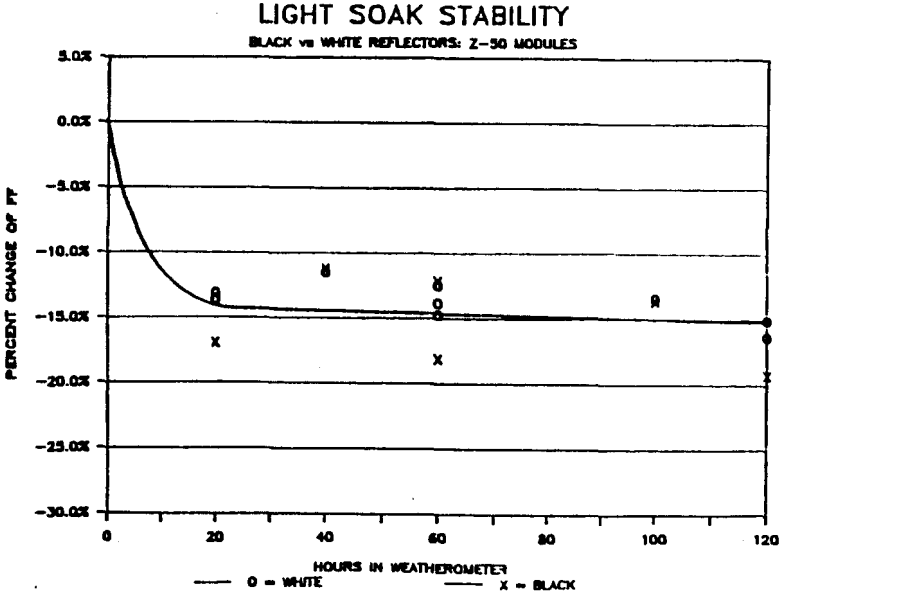

Fig. 1-29. Efficiency and fill factor stability for 50-cell submodules in simulated environment.

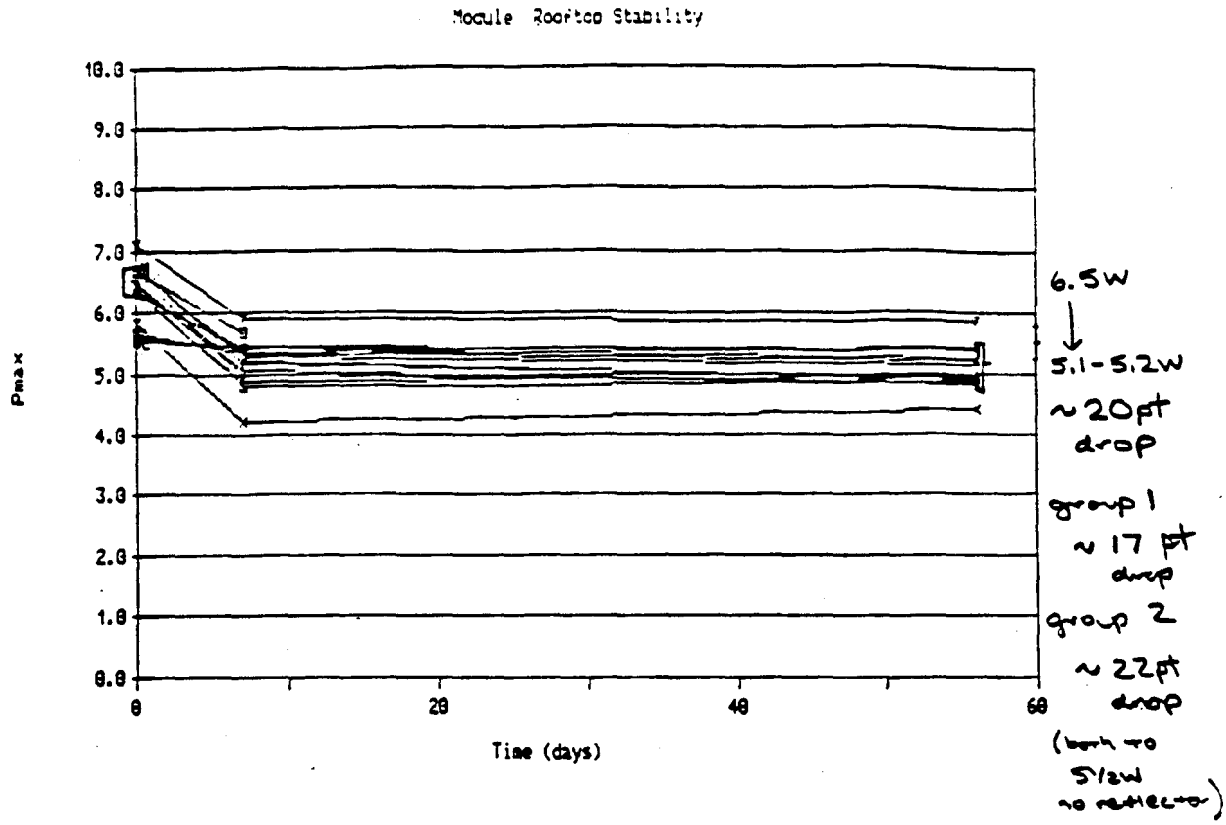

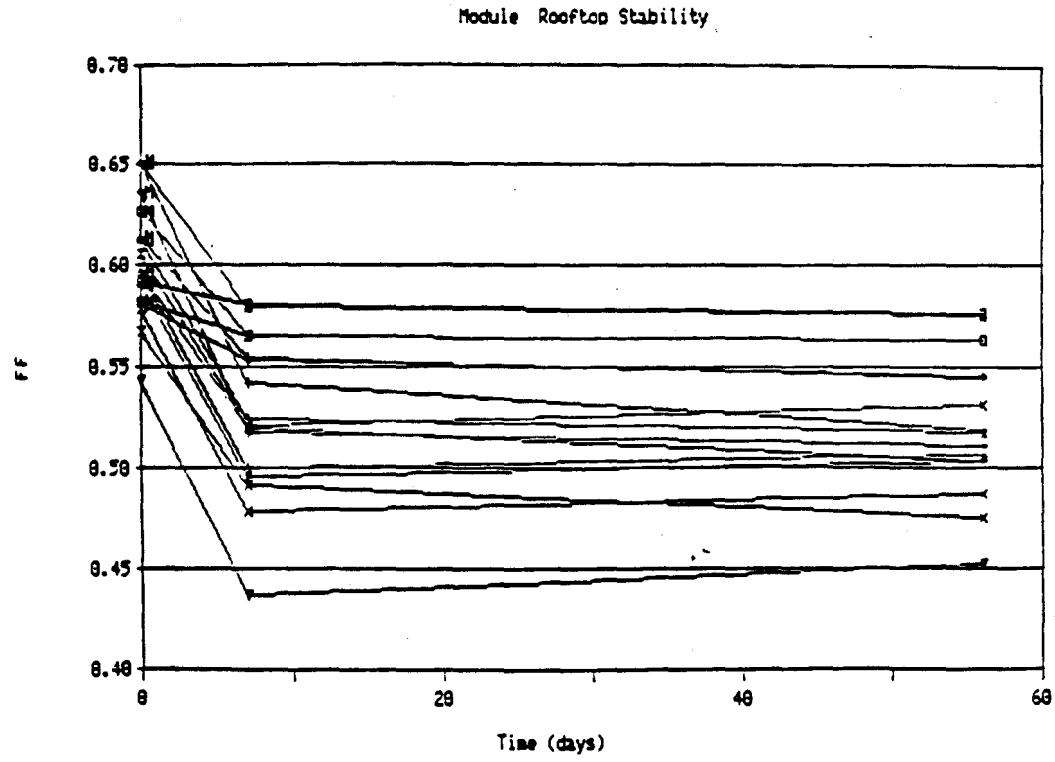

Fig. 1-30. Output power and fill factor stability for 50-cell modules exposed outdoors.

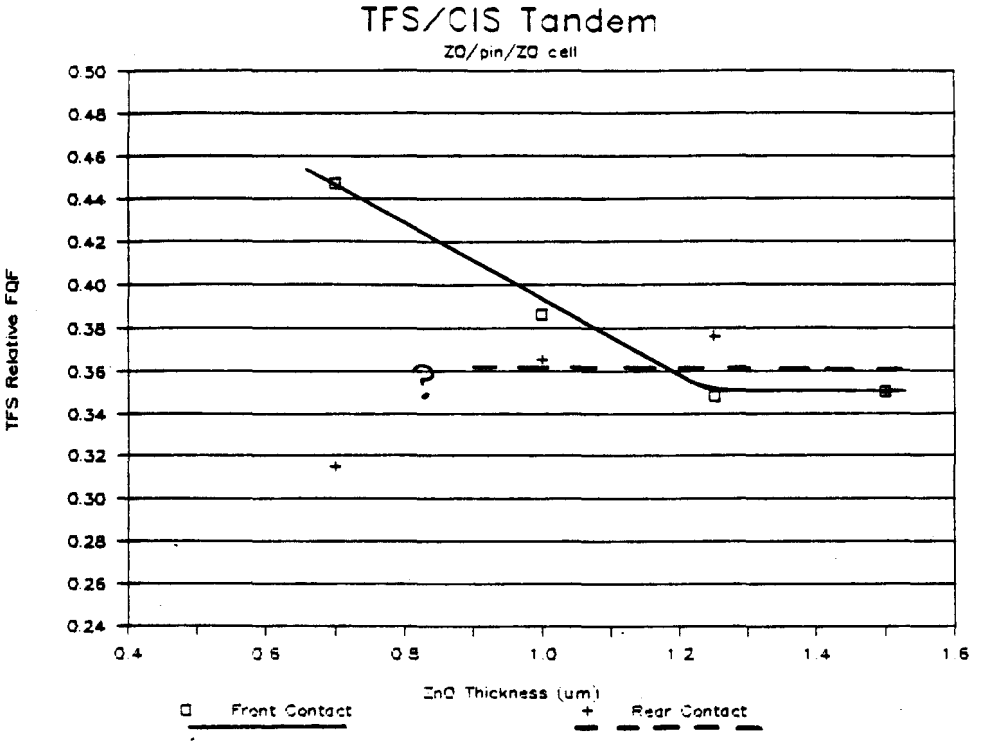

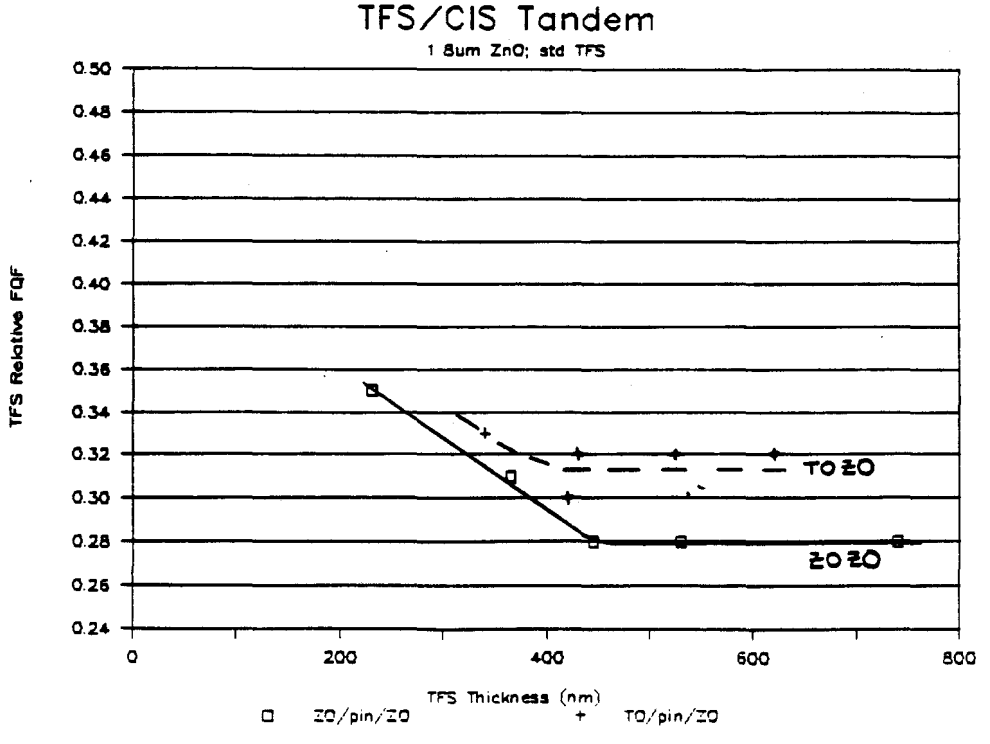

Fig. 1-31. Effect of changes in TFS cell structure and layer thickness on relative filter quality.

these data, this parameter affects both the absorption ("red") edge and the average longwave transmission. In contrast, changes in rear ZnO layer thickness have essentially no impact. These data imply that scattering/light trapping in the TFS device, rather than bulk absorption in the ZnO, is more important in determining filter quality.

The thickness of the TFS layers is less important but filter quality does decline as TFS thickness increases. More detailed examination shows that primarily the absorption ("red") edge is affected, while average longwave transmission is relatively constant: more light is retained in the TFS layers. This is why, on the average, ZnO/TFS/ZnO cells have lower filter quality than TO/TFS/ZnO cells -- they trap more light and generate more current (but this is exactly what is desirable in a tandem device). This illustrates a limitation of a single parameter description of a complex system.

1.6 REFERENCES

1. M. Green et al. High Efficiency Silicon Concentrator Solar Cells. Sandia Report SAND 87-7007 (May 1987).

1.7 APPENDIX: Device Parameters

In addition to the usual photovoltaic parameters -- V_{OC}, J_{SC}, fill factor, and efficiency -- I-V curve "slopes" are often cited as parameters which can be related to shunt and series resistance. In this report these "slopes" are normalized to dimensionless "shape" parameters in a manner similar to that used for curve "fill factor", to allow direct comparison between devices regardless of current and voltage levels. The definitions are:

Shape at Open Circuit, S_{OC}

$S_{OC} = d(V/V_{OC})/d(J/J_{SC})$ at open circuit

$= (J_{SC}/V_{OC}) \times dV/dJ$ "

$= (J_{SC}/V_{OC}) \times$ (inverse) slope at open circuit

Shape at Short Circuit, S_{SC}

$S_{SC} = d(J/J_{SC})/d(V/V_{OC})$ at short circuit

$= (V_{OC}/J_{SC}) \times dJ/dV$ "

$= (V_{OC}/J_{SC}) \times$ slope at short circuit

SECTION 2
CIS PROGRESS

2.1 INTRODUCTION

This section presents the status of work on the CIS portion of the contract. Prior to the contract, 12.5% efficient 3.6 cm^2 CIS devices had been achieved. Transfer of this level of performance to 30x30 cm scale processes was emphasized during this initial phase. A 7.8 watt, 50-cell 30x30 cm CIS module is demonstrated. A test structure fabricated in parallel with this module measures 11.1% active area efficiency. Several diagnostic tools are developed during this period. Uniformity studies of the ZnO and CIS layers were initiated. Preliminary analysis and modeling of CIS module and junction performance are carried out.

2.2 BACKGROUND

CIS provides an important complement in multi-junction submodules to the TFS-based high band gap junction structures. CIS with a band gap near 1 eV is an ideal match to TFS at 1.7 eV for achieving high efficiencies based upon detailed multi-junction device modeling [1-3]. No low band gap TFS-based alloy solar cell presently matches the CIS high cell performance and broad photoresponse out to infrared wavelengths of 1.3 μm [4], as illustrated by the spectral response curve in Fig. 2-1. Prior to the contract, ARCO Solar demonstrated 12.5% efficient CIS solar cells fabricated on 10x10 cm glass substrates [5], as shown in the current-voltage curve in Fig. 2-2. For a 3.6 cm^2 active area, the short-circuit current J_{SC} is 36.7 mA/cm^2, the open-circuit voltage V_{OC} is 487 mV, and the fill factor (FF) is 0.70.

The baseline CIS design consists of glass/Mo/CIS/CdS/ZnO/Ag grid. As shown in Fig. 2-3, the CIS thickness is 2 μm. The CdS window layer is less than 500 Å in order to increase the blue spectral response above the 0.52 μm (2.4 eV) CdS band gap, as shown by the CIS spectral response in Fig. 2-1. A 41.1 mA/cm^2 short-circuit current, among the highest reported for CIS, has been measured under 1985 ASTM 1.5 Air Mass global simulated spectrum [6] and verified by the spectral response curve in Fig. 2-1. Suppression of optical reflection by the textured front ZnO transparent electrode contributes to the high quantum efficiencies. The ZnO thickness is in the range of 1.5 to 3.0 μm.

The major technical problem areas for the semiconductor layers in this program which impact large area submodule performance are: (1) demonstration over large areas of uniform CIS and window layer thicknesses, film stoichiometries, and structural and optical properties; (2) elimination or passivation of defects which result in shunting of the devices over large areas; and (3) improved CIS electronic properties including control of the Fermi level profile and minority carrier properties which impact the reverse saturation current, photocarrier collection, and

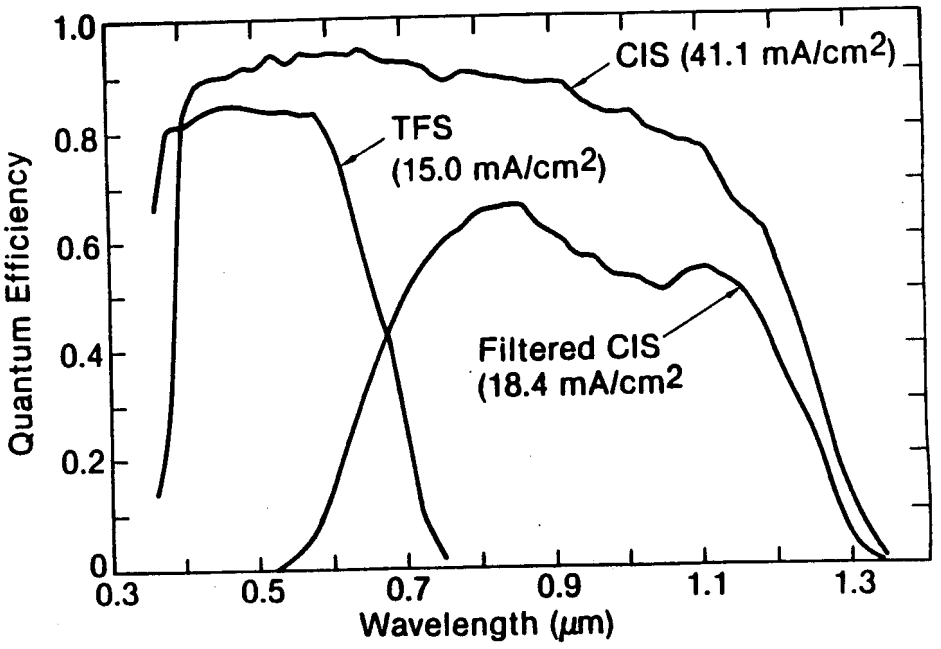

Fig. 2-1. Measured spectral response of TFS, CIS and filtered CIS.

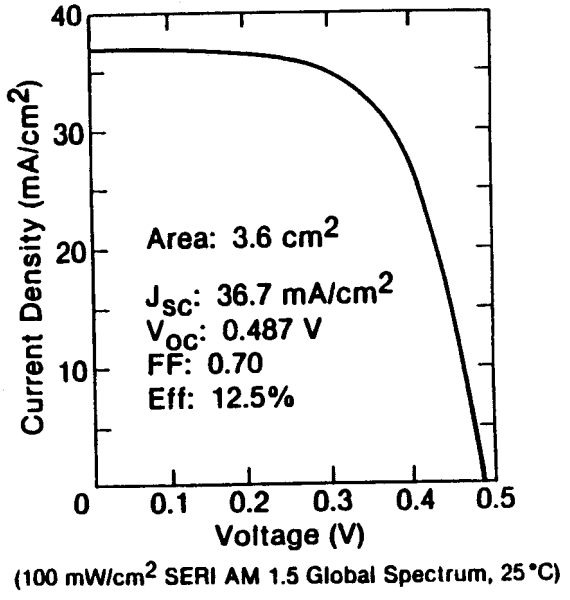

Fig. 2-2. CIS/(CdZn)S/ZnO solar cell current vs. voltage.

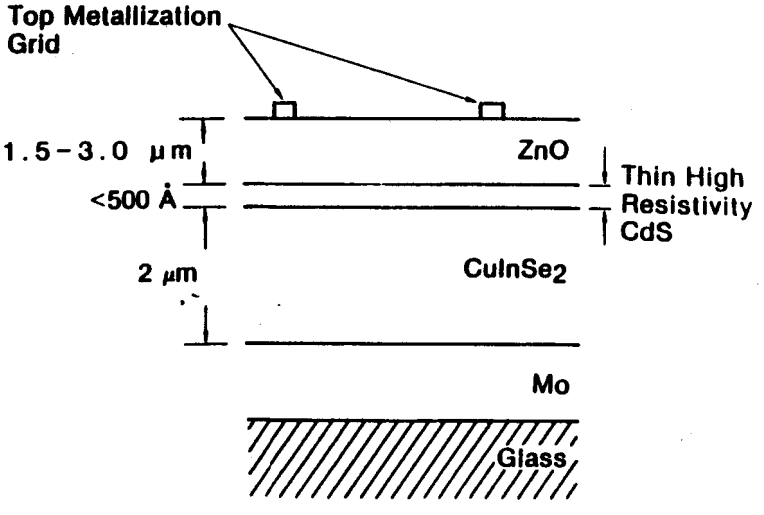

Fig. 2-3. $CuInSe_2$ solar cell cross section.

resultant photovoltaic properties.

The major non-semiconductor technical problem areas for CIS to be assessed are: (1) substrate effects including glass type and properties, impact of glass size and thickness on processing, and impact of glass handling, cleaning, and surface features on subsequent coatings; (2) back contact effects including contact resistance to the CIS or at the interconnect, sheet resistance, bulk layer and surface morphology, and chemical interface reactions; (3) transparent conducting electrode effects including sheet resistance, contact resistance to the ZnCdS or at the interconnect, film morphology, optical transmission, reflection, and absorption including plasma absorption, carrier concentration and mobility; and, as necessary, (4) grid electrode effects including optical shadowing losses and bulk and contact resistance to the transparent electrode or at the interconnect.

2.3 LAYER DEVELOPMENT

Development of all CIS-related deposition processes for coating 30×30 cm areas has been successfully demonstrated. CIS and ZnO layers on 30×30 cm glass plates have been fabricated for delivery to SERI.

As required by Subtask Research Activity (SRA) #1 at the beginning of the contract, CIS was selected as the primary low band gap semiconductor material. The heterojunction contact to CIS will be ZnCdS, CdS, ZnO or similar suitable window layers. Minimization of Cd will be pursued. For controlling and verifying feedstock purity, atomic absorption (AA), inductively coupled plasma (ICP) spectroscopy and gas chromatography/mass spectroscopy (GCMS) are routinely applied to our feedstock characterization.

Assessments of the uniformity of the CIS semiconductor and ZnO transparent conducting contact films are part of SRA #5 and #16 respectively. For ZnO, maps of the thickness, sheet resistance, and optical transmission of a ZnO layer deposited on a 30×30 cm glass plate are shown in Fig. 2-4. The averages are 2.91 μm for thickness, 5.42 ohms/square for sheet resistance, and 0.70 for broad band optical transmission. The ZnO resistivity is about 1.5 milliohm-cm. The thickness is measured on a Tracor Northern Model TN-1710 optical spectrometer from optical interference maxima and minima. Sheet resistance is measured on a Magne-Tron Instruments Model M-700 four-point probe. The broad band transmission is the ratio of currents measured by a EG&G silicon detector with and without the ZnO/glass sample using an Oriel Model 6140 1 kW tungsten halogen light source. For this film, thickness varies less than 7.3%, sheet resistance less than 12%, and broad optical transmission less than 5.5%.

These variations in ZnO properties are projected to have little negative impact on CIS module performance. For example, the modeled fill factor change with ZnO sheet resistance, as shown in

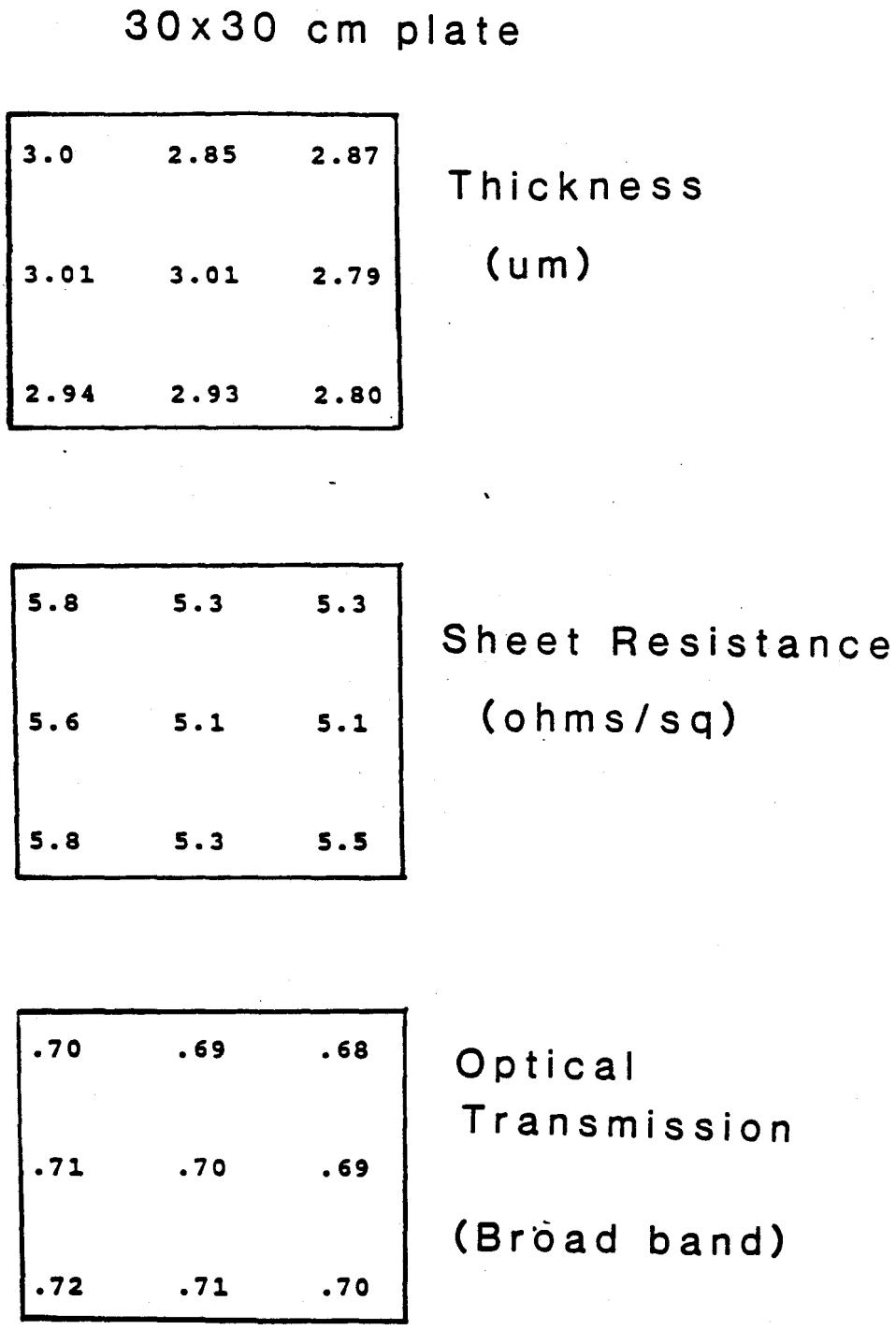

Fig. 2-4. Map of ZnO uniformity.

Fig. 2-5, is:

J_{sc} (mA/cm^2)	50-cell module	75-cell module
40	0.0067	0.0029
20	0.0033	0.0014

expressed as absolute fill factor decrease per ohm/square change. Thus, if the ZnO sheet resistance for the entire module was 5.8 ohms/square (the maximum value for the layer discussed above) rather than the average value of 5.4, the decrease in fill factor for a 50-cell module would be only 0.001 and 0.003 for 20 and 40 mA/cm^2 J_{sc}. For a 75-cell module, the fill factor decrease would be even less. Since only a small portion of the 30×30 cm area has the higher ZnO sheet resistance and other areas have less than the average sheet resistance, the effect on fill factor of the ZnO sheet resistance non-uniformity is considered negligible.

Characterization of the CIS layer over 30×30 cm areas, including thickness, stoichiometry, resistivity and optical properties are in process and will be discussed in the Final Report.

2.4 MODULE DEVELOPMENT

Substantial effort has focused on the design, fabrication, and characterization of 30×30 cm CIS modules. In addition, new techniques have been developed to characterize module performance. The baseline CIS module configuration is 50 series-connected cells as shown in Fig. 2-6. The design aperture area is 844 cm^2 (28.7×29.4 cm), allowing for bus bars at opposite ends

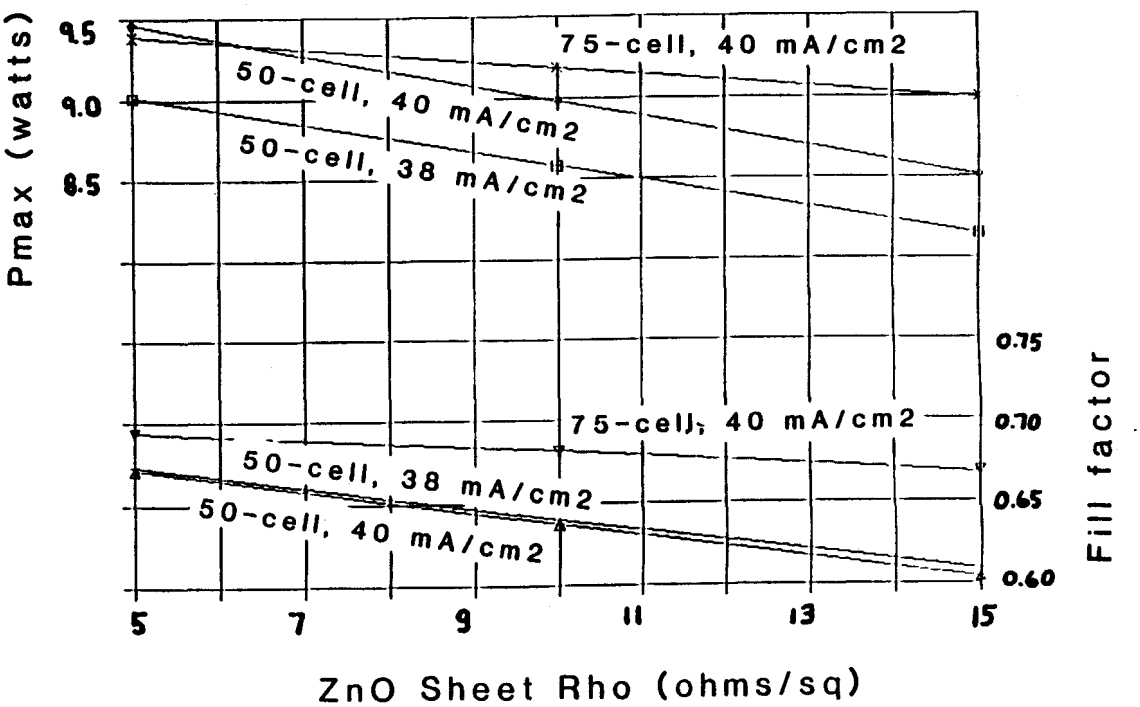

Fig. 2-5. Projected P_{max} and fill factor vs. ZnO sheet rho.

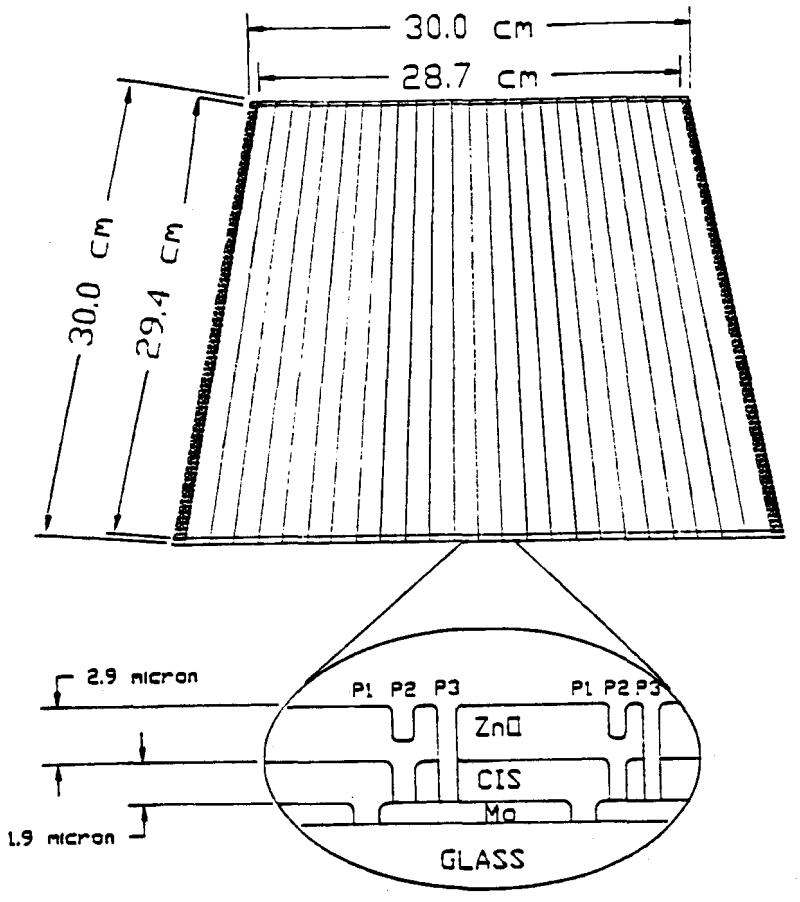

Fig. 2-6. CIS module layout.

of the module and borders along the edge of the module for isolation of individual cell segments. Electrical interconnects, as shown, between the front ZnO layer of one cell and the back Mo layer of the adjacent cell are made through vias created in the CIS. The interconnect regions also provide for electrical isolation between adjacent front ZnO layers and adjacent back Mo layers.

2.4.1 7.8 Watt CIS Module

The current-voltage (I-V) characteristic of a 7.8 watt, 50-cell CIS module is shown in Fig. 2-7, as measured on a Spectrolab large area pulsed solar simulator (LAPSS) calibrated to the ASTM Air Mass 1.5 global spectrum. The short-circuit current is 595 mA, the open-circuit voltage is 21.567 V (431 mV/cell), and the fill factor is 0.61. The 7.8 watt power output translates to an aperture area efficiency of 9.2% and an active area efficiency of 10.0%. A preliminary evaluation of the factors limiting the power output to 7.8 watts is presented below.

2.4.2 Open-Circuit Voltage Mapping

Detailed analysis of the properties of a module is complicated and usually requires destruction of the module to determine the

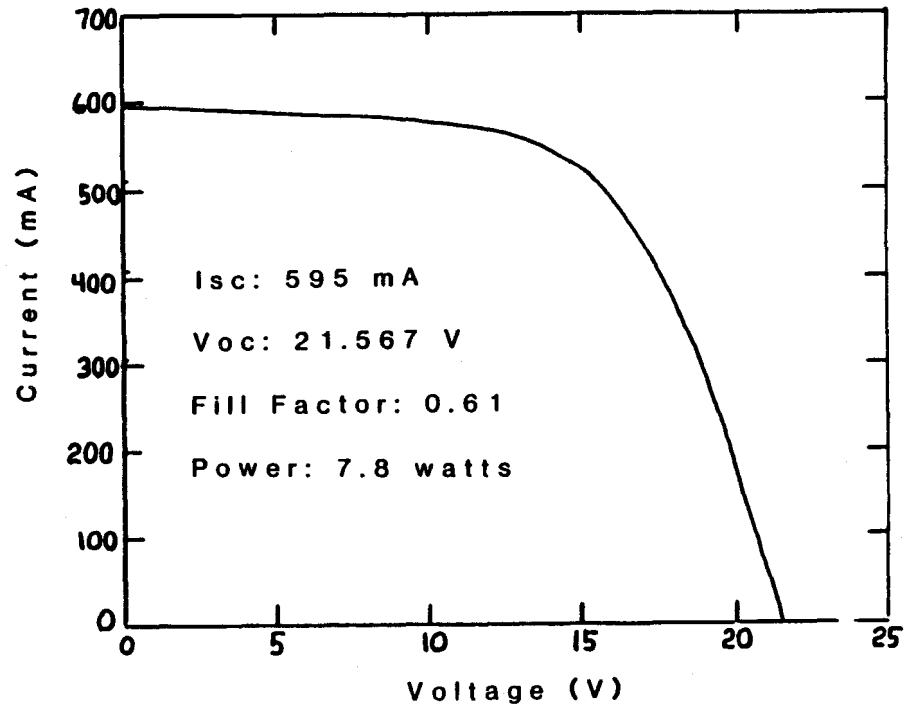

Fig. 2-7. I-V curve of 50-cell CIS module on 30×30 cm plate.

individual cell properties. In the case of long narrow cells as shown in Fig. 2-6, individual cell I-V curves measured from the edge of the cells would be dominated by the series resistance involved with transporting current the long length of the cell. One option is to map the cell V_{OC}'s since no current flows to the external circuit at V_{OC}. A fixture and data acquisition system have been developed for mapping the 50 individual cell V_{OC}'s. The V_{OC} mapper has been successful in measuring the relative V_{OC} outputs of each of the cells. For many modules, the cell V_{OC}'s are similar to one another except possibly for a few cells with reduced V_{OC} caused by localized shunts.

2.4.3 Test Structure Witness Plates

Another approach to evaluate the CIS junction quality is the development of 30×30 cm test structure witness plates, which replicate a 10×10 cm standard test structure pattern nine times over the 30×30 cm area. Sixteen 4 cm^2 CIS devices are laid out in two rows of 8 over the 10×10 cm areas. All of the existing fixtures for the computer-assisted testing CIS cells on 10×10 cm substrates can be utilized.

The uniformity of CIS junction quality can thus be evaluated by mapping the photovoltaic characteristics of the 96 cells over the 30×30 cm area. Cell efficiency, V_{OC}, J_{SC}, and fill factor for one CIS witness plate are profiled in Figs. 2-8 through 2-11. Trends are discernable, although the statistics are not exact due to variations in the fabrication of individual cells or damage to test structures during their fabrication or handling. Overall performance is remarkably uniform. In certain cases, local defects can be identified which reduce the cell performance.

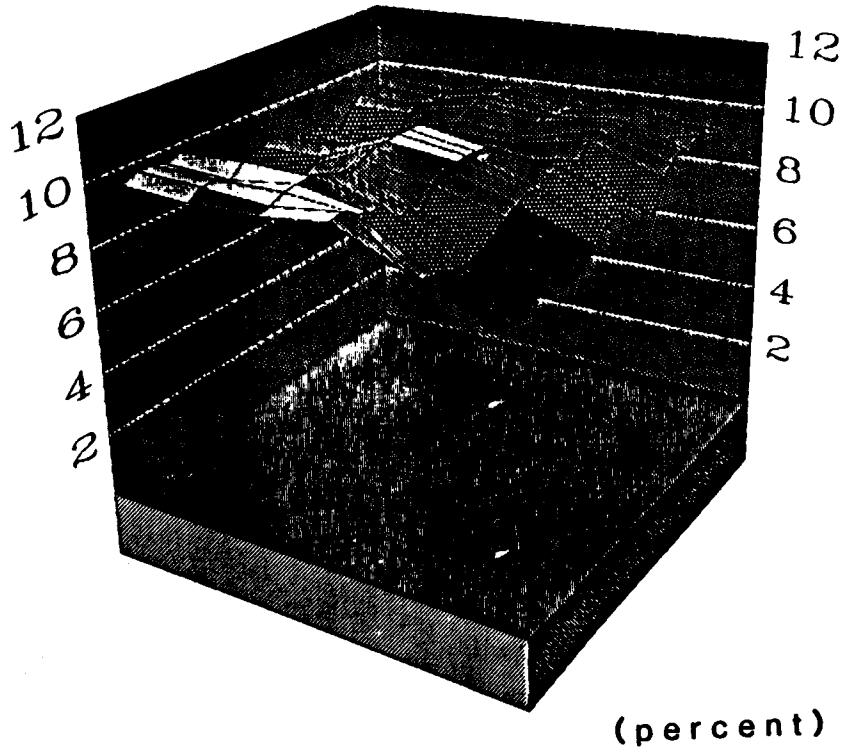

Fig. 2-8. Efficiency performance map of test structures on 30x30 cm witness plate.

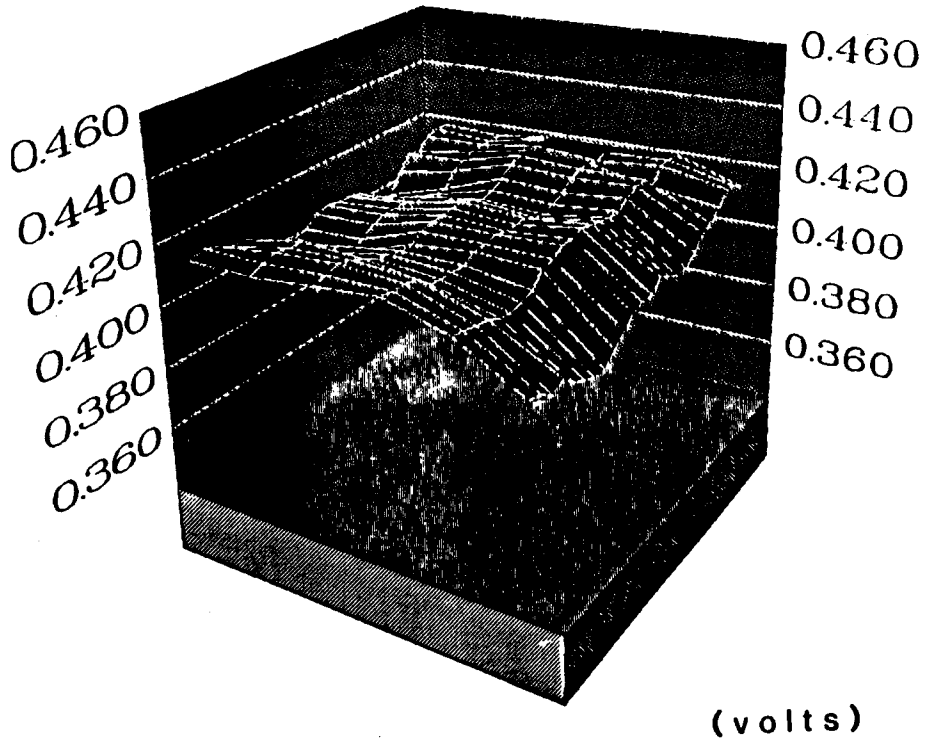

Fig. 2-9. V_{OC} performance map of test structures on 30x30 cm witness plate.

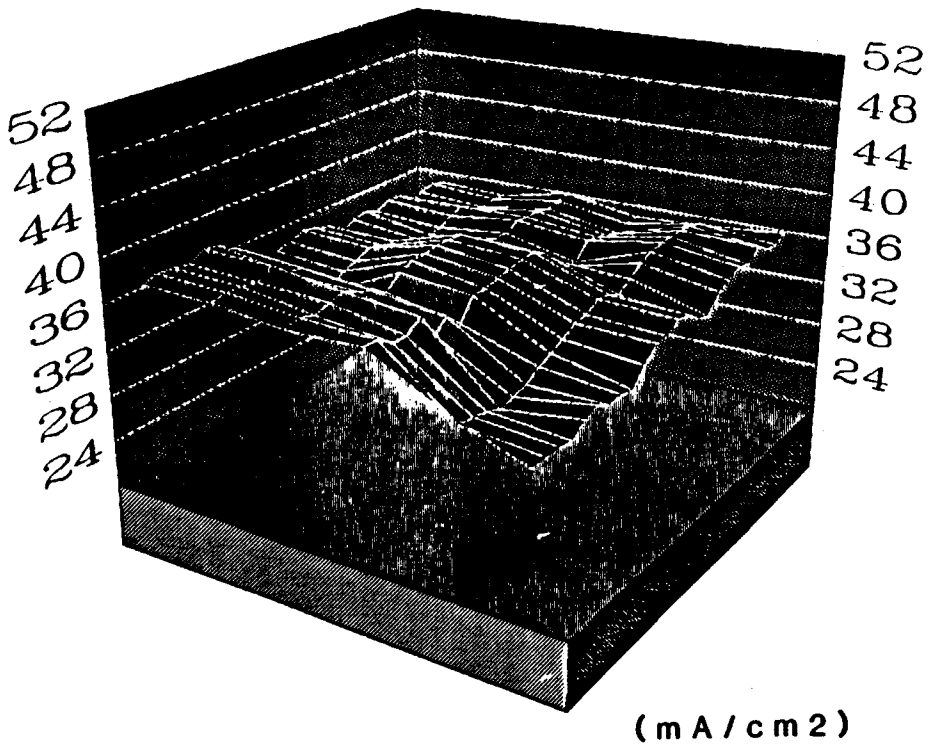

Fig. 2-10. I_{sc} performance map of test structures on 30x30 cm witness plate.

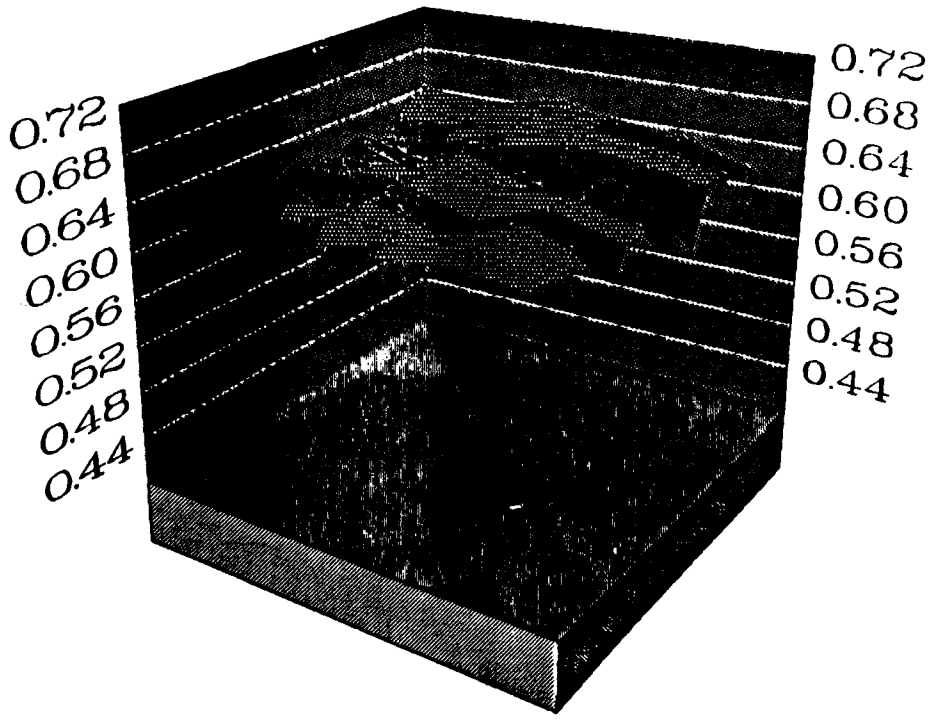

Fig. 2-11. Fill factor performance map of test structures on 30x30 cm witness plate.

2.4.4 Interconnect Losses

Problems associated with module interconnects can lower module output in several ways: (1) voltage drop at the interconnects due to high ZnO/Mo contact resistance; (2) electrical shunting in the interconnect region between adjacent back Mo layers or front ZnO layers, or between the front ZnO and back Mo layer of an individual cell; or (3) loss of active area because of excessive area between the back Mo isolation cut and the front ZnO isolation cut (defined as P1 and P3 in Fig. 2-6).

Contact resistance and layer sheet resistances can be determined by passing a constant current through the ZnO into the ZnO/Mo contact and profiling voltage versus position. As shown in Fig. 2-12, the ZnO/Mo contact resistance measures 9.4×10^{-3} ohm-cm^2. Auger analysis of these contacts, shown in Fig. 2-13, reveals the presence of a thin (50 Å) MoSe layer at the ZnO/Mo interface which contributes to contact resistance.

2.4.5 Module Analysis

The current-voltage characteristic of a 4 cm^2 CIS test structure with similar processing to the module above is shown in Fig. 2-14. The 3.6 cm^2 active area efficiency is 11.1%, with a 38.6 mA/cm^2 J_{SC}, 436 mV V_{OC}, and 0.66 fill factor. The corresponding spectral response curve is given in Fig. 2-15. Comparing the test structure to the module, the primary difference in performance is due to the lower module fill factor of 0.61. Computer modeling indicates that the lower module fill factor can be attributed to the ZnO/Mo interconnect resistance. Reducing the contact resistance from 9.4×10^{-3} to less than 1×10^{-3} ohm-cm^2 is necessary. The lower average V_{OC} for the module of 431 mV versus 436 mV is due to slight cell-to-cell variations. The aperture area efficiency of the module can also be improved by reducing the area loss associated with the interconnects. Finally, higher module power output will result from improved junction quality, primarily from a higher V_{OC} and increased fill factor. As noted in Section 2.2, the 12.5% efficient CIS cell has a 487 mV V_{OC}. Improving the active area J_{SC} from 38.6 to above 40 mA/cm^2 will also contribute to module output.

2.5 CIS DEVICE ANALYSIS

Long term performance gains in CIS module performance will be driven by the CIS junction quality. Thus, it is necessary to understand the fundamental mechanisms controlling the photovoltaic properties of CIS devices. This section presents preliminary analysis of the CIS optical properties, spectral response, I-V versus temperature, and capacitance-voltage.

2.5.1 CIS Optical Properties

Optical transmission and reflection are measured for CIS deposited on glass using a Perkin-Elmer Model 330

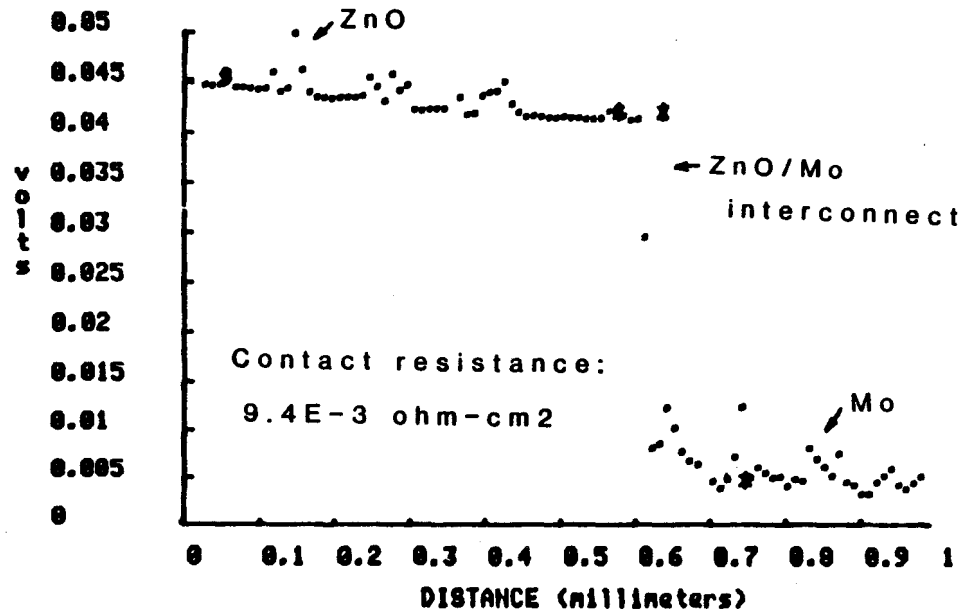

Fig. 2-12. ZnO/Mo contact resistance voltage profile.

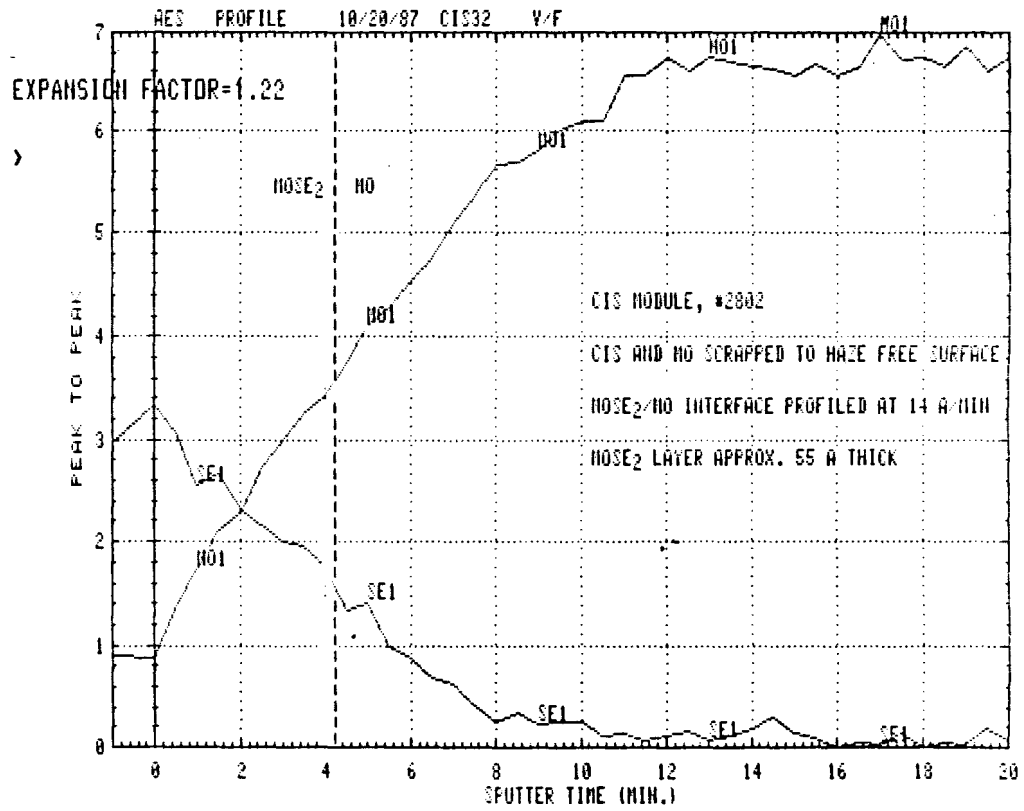

Fig. 2-13. Auger analysis of ZnO/Mo contact.

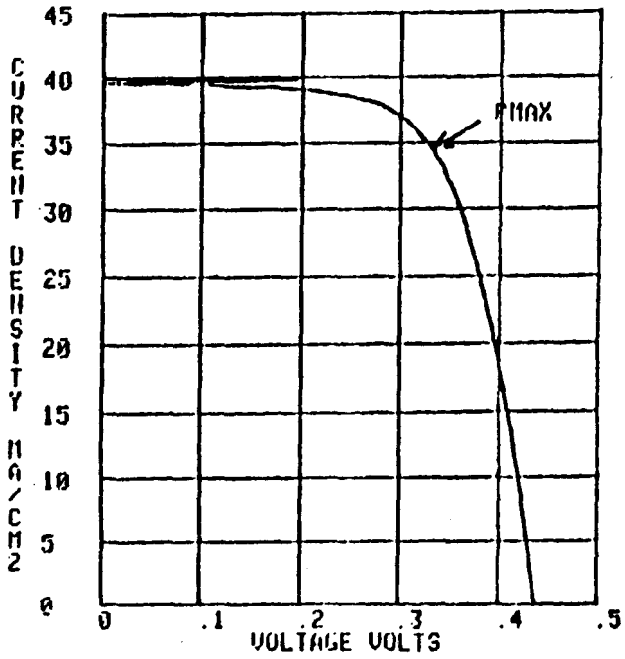

Active Area:
3.6 cm2

Jsc: 38.6 mA/cm2

Voc: 0.436 V

FF: 0.66

Eff: 11.1%

Fig. 2-14. I-V curve of 4 cm^2 CIS test structure on 30×30 cm witness plate.

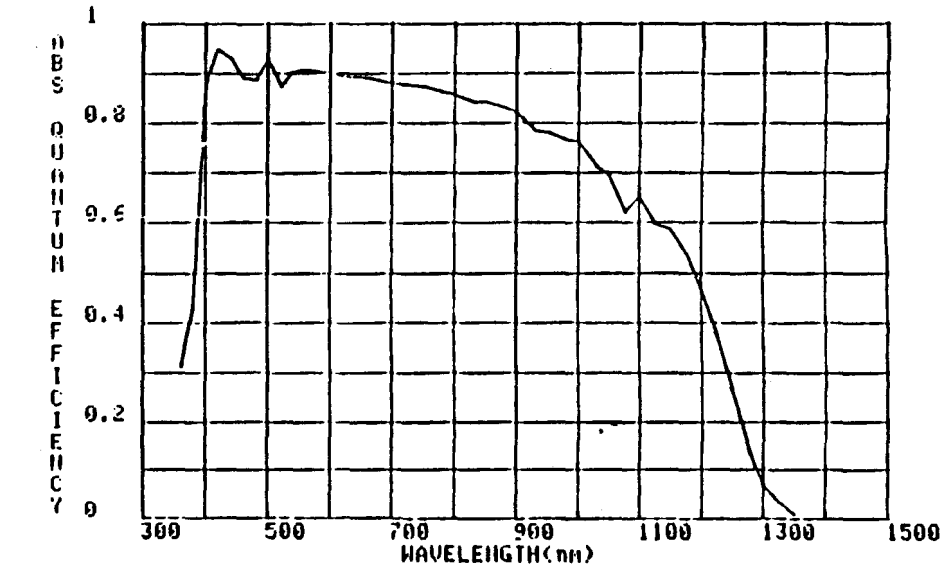

Jsc= 38.63 ma/cm2(AM1.5 GLOBAL ASTM 1985)

Fig. 2-15. Spectral response of 4 cm^2 CIS test structure on 30×30 cm witness plate.

spectrophotometer with a 60 mm integrating sphere. Figure 2-16 shows the results for a 2.06 μm thick CIS film. The corresponding plot of calculated CIS optical absorption coefficient versus wavelength is given in Fig. 2-17. The textured morphology of the CIS films was found to cause light scattering and introduce errors in the optical data below the CIS band gap, implying artificially high CIS optical absorption values. In addition, more accurate determination of the short wavelength absorption coefficients requires analysis of a series of thinner CIS films. Optical data from a more extensive study by J. Tuttle, SERI [7], also plotted in Fig. 2-17, is considered consistent with the properties of our CIS films.

2.5.2 CIS Spectral Response

The absolute spectral response of CIS junctions is measured using an ARCO-designed spectral response station. Quantum efficiency (QE) is determined by focusing all incident light on the device using an aperture and measuring the induced current. Forty-four narrow band interference filters are used to cover the wavelength range from 360 nm to 1350 nm. The incident light intensity is calibrated using reference Si and Ge detectors. Fluctuations in the light intensity during the measurement are monitored and corrections made. The incident light is optically chopped and lock-in amplifiers are used to detect the light induced in-phase signal.

A comparison between the measured and modeled CIS spectral response is illustrated in Fig. 2-18 for a CIS device with 37.1 mA/cm^2 J_{SC}, indicating reasonable agreement. The calculated QE is given by:

$$QE = (1-R)\cdot\exp[-\alpha_{ZnO}\cdot t_{ZnO}]\cdot\exp[-\alpha_{CdS}\cdot t_{CdS}]\cdot$$

$$[1-\exp(-\alpha_{CIS}\cdot W_{CIS})/[1+\alpha_{CIS}\cdot L_{CIS}]] \qquad (2\text{-}1)$$

where R is the front reflection loss, α is the optical absorption coefficient versus wavelength and t is the thickness of the respective layers, W is the depletion width, and L is the minority carrier diffusion length. A front reflection loss of 12% was measured for this device using the Perkin-Elmer Model 330 spectrophotometer. The CdS thickness is less than 500 Å which makes the CdS absorption term negligible. A CIS space charge depletion width of 0.4 μm is determined from capacitance-voltage measurements. A CIS minority carrier diffusion length of 0.5 μm is assumed. The short wavelength cut-off at about 380 nm is due to the ZnO band gap. The roll-off of response at longer wavelengths is consistent with the CIS optical absorption coefficients and device properties. The ZnO plasma absorption must be considered for wavelengths longer than 900 nm, as shown in Fig. 2-18. The ZnO absorption data is measured with the Perkin-Elmer spectrophotometer for ZnO layers deposited on glass.

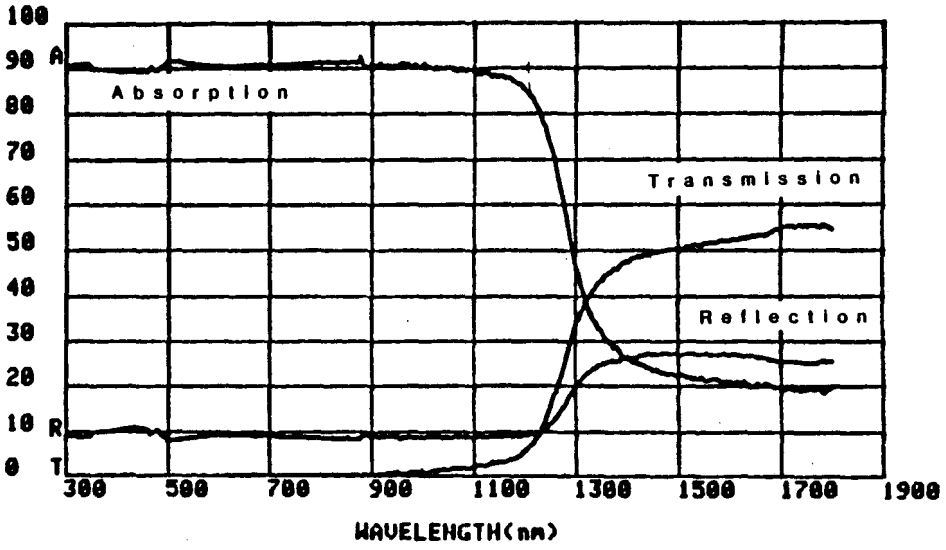

Fig. 2-16. Optical transmission/reflection of 2.06 μm CIS film on glass.

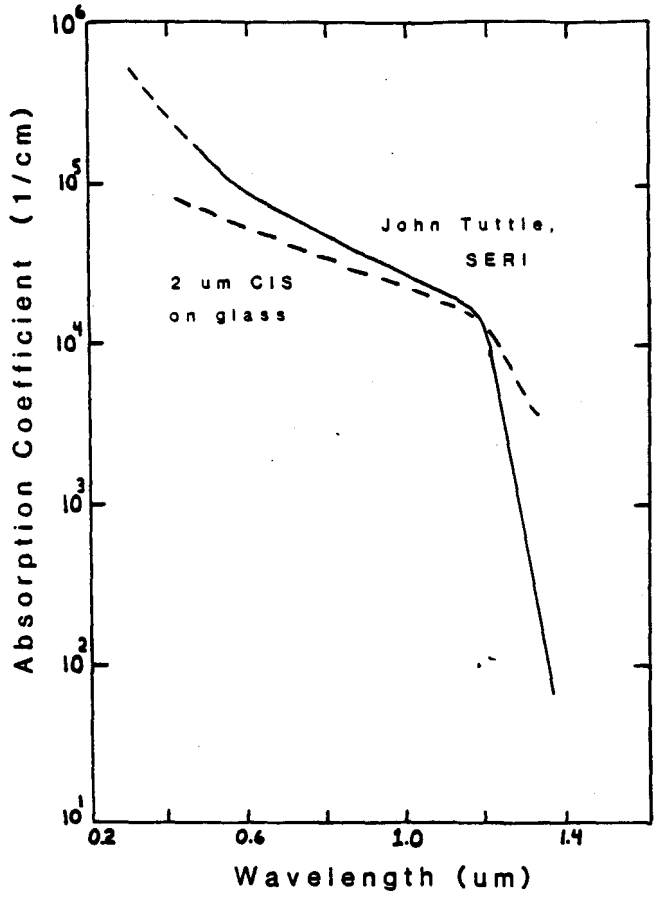

Fig. 2-17. Optical absorption coefficient vs. wavelength for 2.06 μm CIS film.

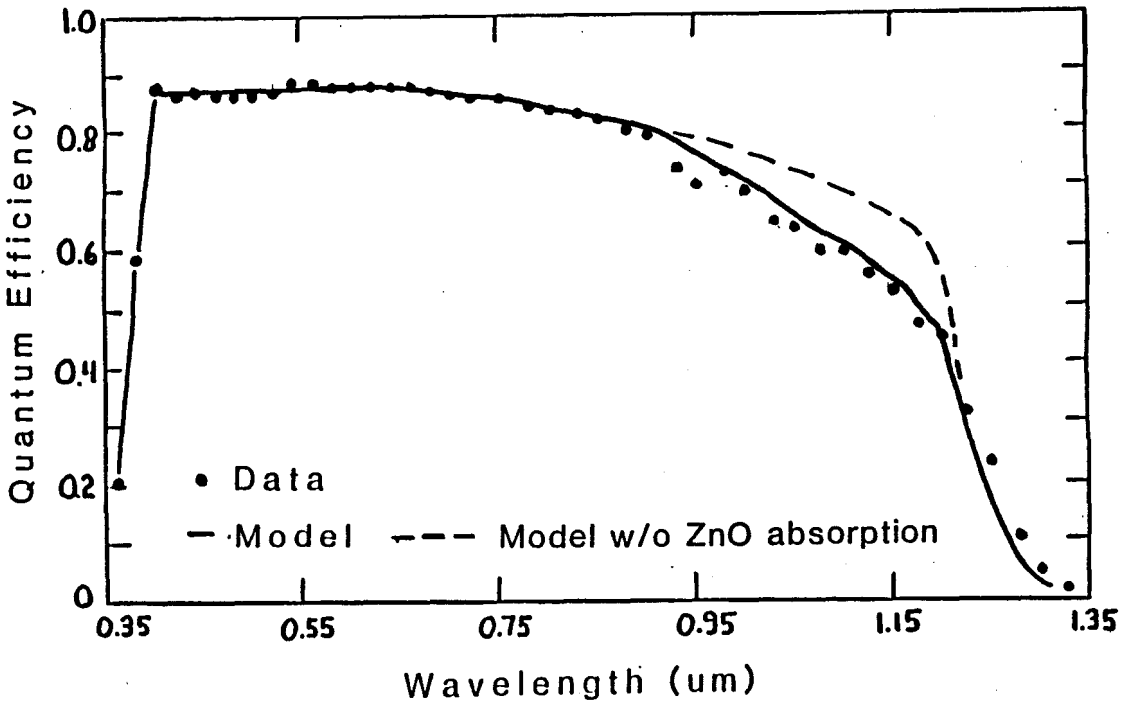

Fig. 2-18. Measured and modeled spectral response for CIS devices.

The spectral response for the 41.1 mA/cm^2 J_{SC} cell shown in Fig. 2-1 is achieved by reducing the front reflection and ZnO plasma absorption losses, in agreement with the above modeling. The high current CIS device is 9.8% efficient with 436 mV V_{OC} and 0.546 fill factor. The low fill factor is due to high (100 ohms/square) ZnO sheet resistance. These results demonstrate that the ZnO absorption losses can be minimized. Trade-offs between ZnO sheet resistance and optical properties need to be evaluated since ZnO sheet resistance in the 5 to 15 ohms/square range is desirable for modules as shown in Fig. 2-5. Presently 20 ohms/square has been achieved with the low optical loss ZnO.

2.5.3 Current-Voltage vs. Temperature

Understanding the CIS junction mechanism will contribute to achieving high V_{OC} and resultant performance. To accomplish this, a station has been set up to measure I-V versus temperature for test structures on 10x10 cm substrates using a Ransco Model 934 Bench Chamber with a temperature range of 77K to 400K. Installation of a light source inside the chamber allows light as well as dark I-V to be measured. The present measurements assume that the light source intensity does not vary as the temperature is changed. This needs to be verified using a fiber optic probe and sensor to monitor the light intensity.

The light and dark I-V characteristics versus temperature were measured for two CIS cells, Q8829C11 with a 400 mV V_{OC} and Q8705C6 with a 450 mV V_{OC}. Results are summarized in Table 2-1

Table 2-1. I-V characteristics vs. temperature for CIS cells.

Cell Q8829C11 (400 mV V_{OC} at 25°C):

Temp (K)	J_{SC} (mA/cm^2)	V_{OC} (mV)	FF	Eff (%)	dark J_o (A/cm^2)	A	n
314	38.4	375	0.562	8.1	5.5E-6	20.3	1.8
300	38.6	401	0.580	9.0	3.3E-6	20.8	1.9
281	37.7	438	0.601	9.9	8.5E-7	21.3	1.9
261	37.4	469	0.609	10.7	1.4E-7	23.7	1.9
222	41.0	519	0.586	12.5	2.5E-8	25.4	2.1
205	41.6	532	0.578	12.8	5.9E-9	26.3	2.1
186	40.6	548	0.567	12.6	5.2E-9	23.7	2.6
164	41.1	551	0.558	12.3	n/a	n/a	n/a

Cell Q8705C6 (450 mV V_{OC} at 25°C):

Temp (K)	J_{SC} (mA/cm^2)	V_{OC} (mV)	FF	Eff (%)	dark J_o (A/cm^2)	A	n
299	38.3	443	0.635	10.8	3.0E-6	19.0	2.0
280	36.9	485	0.655	11.7	1.4E-6	19.0	2.2
262	36.9	517	0.668	12.6	2.5E-7	20.8	2.1
241	36.1	560	0.681	13.8	9.1E-8	21.6	2.2
219	35.4	608	0.684	14.7	2.4E-8	28.3	1.9
201	35.0	639	0.680	15.2	2.4E-8	26.9	2.1
181	34.4	674	0.667	15.5	8.1E-9	27.6	2.3
138	33.0	732	0.630	15.2	1.0E-8	22.5	3.7
119	31.4	747	0.603	14.1	1.0E-8	18.4	5.3
98	29.7	756	0.579	13.0	1.0E-8	15.3	7.7

where dark J_o, A, and n are the implied junction reverse saturation current, voltage coefficient, and diode factor derived from a log (dark current) versus voltage plot, assuming the dark junction I-V after correcting for series and shunt resistance is of the form:

$$J_{dark} = J_o\ [\exp(A \cdot V) - 1] = J_o\ [\exp(q \cdot V/nkT) - 1] \qquad (2\text{-}2)$$

The light current-voltage curves for the 450 mV V_{OC} cell at 303K, 200K, and 100K are shown in Figs. 2-19 through 2-21. V_{OC}, fill factor, and efficiency increase as temperature decreases, until current transport begins to be suppressed, probably at the Mo/CIS electrical contact. The highest V_{OC} measured is 756 mV at 100K. If the measured J_{SC} of 34.4 mA/cm^2 is correct at 181K, the CIS efficiency at this temperature is 15.5% with a 674 mV V_{OC} and 0.667 fill factor.

Jsc : 38.313 ma/cm2
Voc : 0.443 volts
Jpn : 32.067 ma/cm2
Vpn : 0.336 volts
Pdn : 10.769 mw/cm2
FF : 63.5 %
Eff : 10.77 %
dV/dJ
@Voc : 1.73 ohm-cm2
SOC: 0.150
dJ/dV
@Jsc : 2.27 mS/cm2
SSC: 0.026

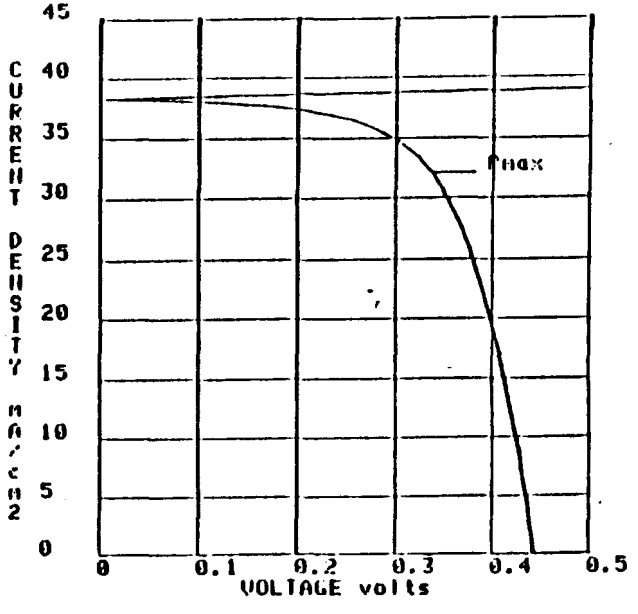

Fig. 2-19. 303 K (30°C).

Jsc : 35.014 ma/cm2
Voc : 0.639 volts
Jpn : 30.360 ma/cm2
Vpn : 0.501 volts
Pdn : 15.211 mw/cm2
FF : 68.0 %
Eff : 15.21 %
dV/dJ
@Voc : 2.60 ohm-cm2
Cor.C: 1.000
dJ/dV
@Jsc : 1.08 mS/cm2
Cor.C: 0.964

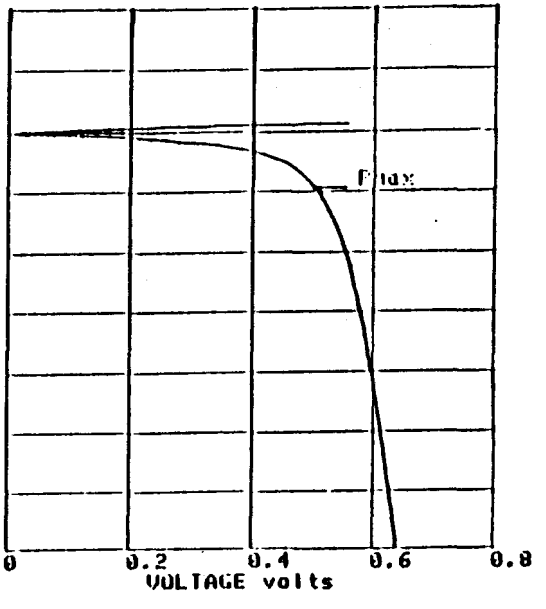

Fig. 2-20. 200 K (-73°C).

Jsc : 29.741 ma/cm2
Voc : 0.756 volts
Jpn : 24.863 ma/cm2
Vpn : 0.524 volts
Pdn : 13.028 mw/cm2
FF : 57.9 %
Eff : 13.03 %
dV/dJ
@Voc : 464.20 ohm-cm2
Cor.C: 0.428
dJ/dV
@Jsc : 1.46 mS/cm2
Cor.C: 0.974

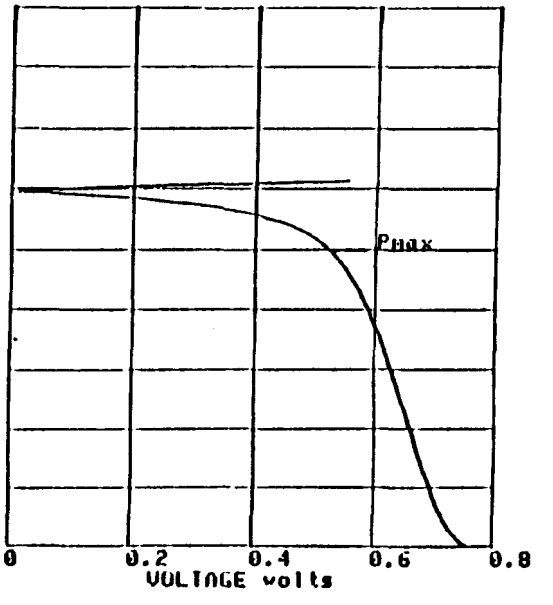

Fig. 2-21. 100 K (-173°C).

CIS I-V vs. temperature:

The plot of J_o versus inverse temperature for the 400 mV cell is shown in Fig. 2-22. At higher temperatures (above 260K), J_o is thermally activated, fitting the form:

$$J_o = J_{oo} \exp(-E_a/kT) \qquad (2\text{-}3)$$

where J_{oo} equals 415 A/cm^2 and E_a equals 0.491 eV. At lower temperatures, J_o is less sensitive to temperature, dominated possibly by tunneling or charge injection.

V_{OC} versus temperature for the two cells is plotted in Fig. 2-23. The extrapolation of V_{OC} versus temperature to 0K which is representative of the junction built-in voltage V_b gives 0.931 V and 1.025 V for the 400 mV and 450 mV V_{OC} cells. Their respective $V_{OC}(T)$ slopes are -1.77 mV/K and -1.95 mV/K.

A preliminary discussion of the above measurements is presented in Section 2.5.5. Further measurements are required for complete analysis. As noted above, for example, a fiber optic detector needs to be installed in order to verify that the light intensity is held constant during the measurements. The values of J_o, A, and n are difficult to interpolate from the data and require curve fitting in order to confirm their values.

2.5.4 Capacitance vs. Voltage

Capacitance versus voltage and frequency is another tool for characterizing CIS junction properties. Depletion width versus applied voltage, carrier concentration versus position, and effective built-in voltage (voltage intercept of $1/C^2$ versus V) are typical results derived from C-V data. Proper interpretation of C-V data is difficult. For example, trap states at the interface or within the space charge region result in a frequency dependence of the data. The voltage intercept of the $1/C^2$ versus V plot becomes no longer simply the junction built-in voltage but is shifted by the presence of the interface states. Compensated doping due to the presence of both acceptors and donors also complicates the interpretation of the data. In the case of ZnO/thin CdS/CIS devices, the CdS layer (less than 500 Å) is fully depleted and the depletion width shift versus voltage occurs in the CIS.

CIS junction capacitance measurements were made using a HP Model 4192A LF Impedance Analyzer (5Hz - 13.MHz) coupled to a Tektronix 4052 computer terminal. Plots of $1/C^2$ versus voltage and depletion width versus voltage for the 400 mV cell discussed in Section 2.5.3 are shown in Fig. 2-24. The voltage intercept of $1/C^2$ versus voltage is 0.938 V, in agreement with the zero Kelvin V_{OC} intercept of 0.931 in Fig. 2-23. The depletion width at zero bias is 0.3 μm at 50 kHz, assuming a dielectric constant for CIS of 13 [8].

The data fit the form given by an abrupt junction model where the depletion width W is predominately in the CIS:

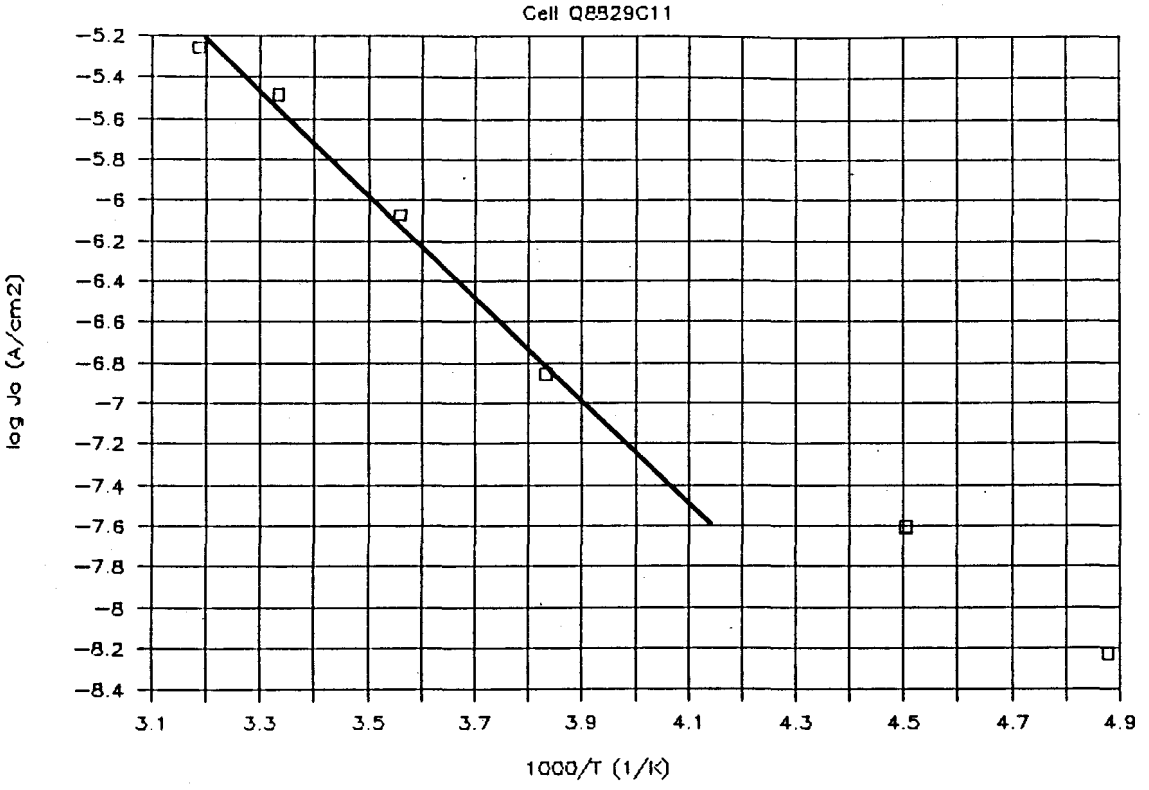

Fig. 2-22. CIS J_o vs. temperature.

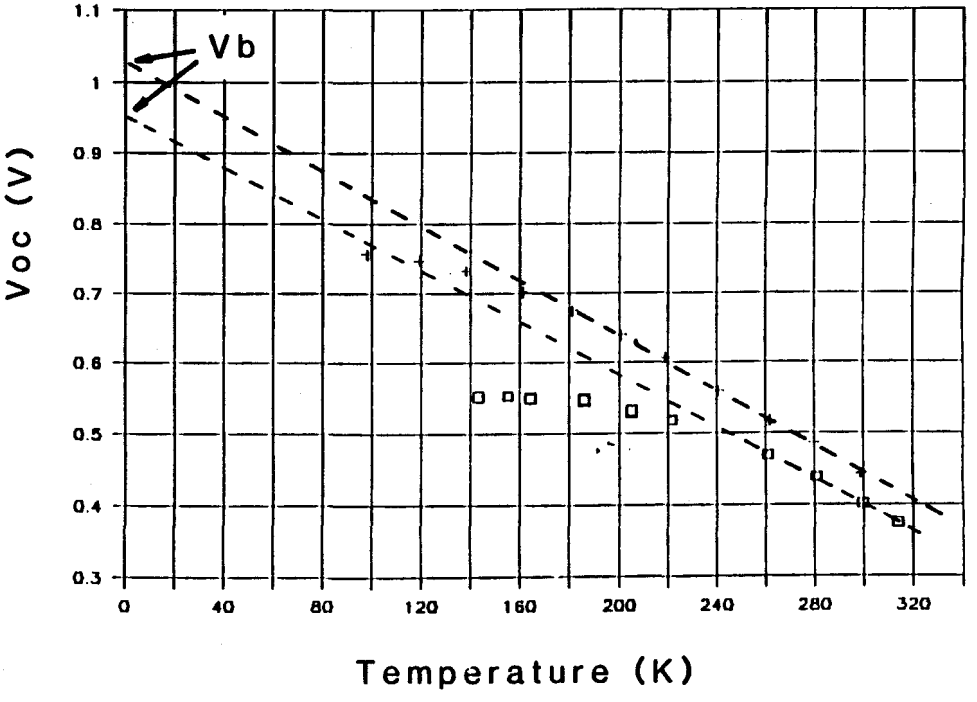

Fig. 2-23. CIS V_{OC} vs. temperature.
□ = 400 mV V_{OC} cell. + = 450 mV V_{OC} cell.

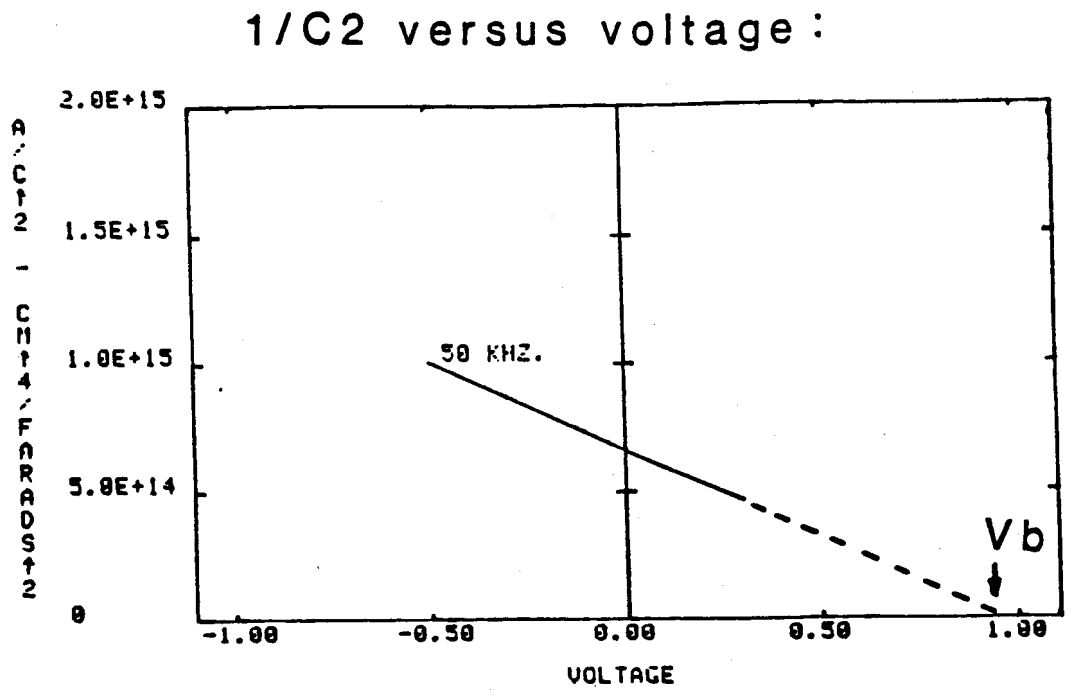

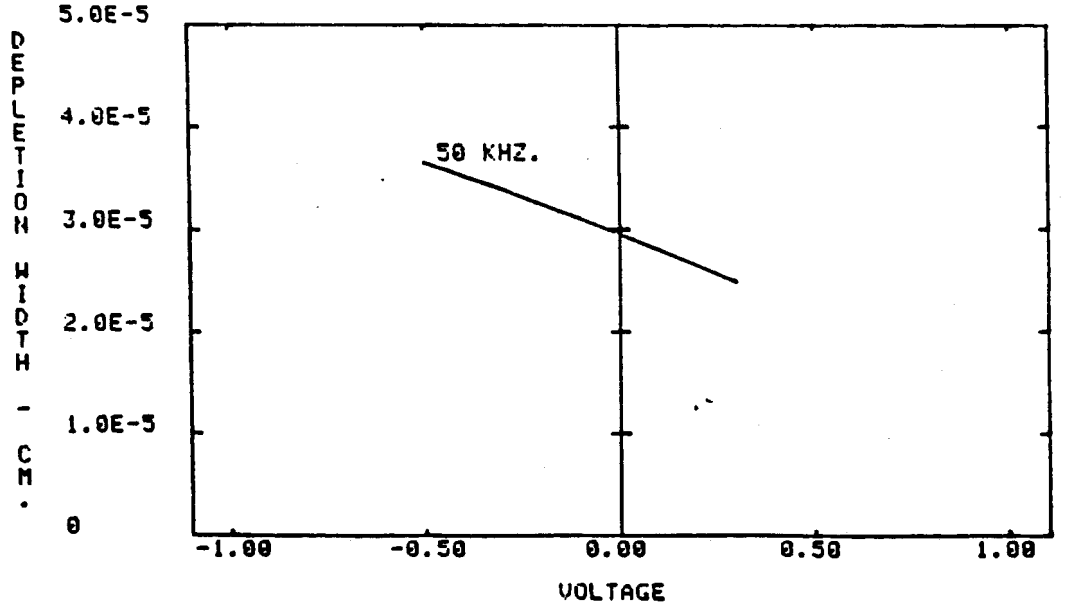

Fig. 2-24. CIS junction capacitance.

$$W = [2 \cdot \varepsilon \cdot \varepsilon_o \cdot (V_b - V)/q \cdot N_A]^{1/2} \quad (2\text{-}4)$$

where ε_o is the free space dielectric constant (8.86E-14 Farads/cm), and the apparent acceptor concentration N_A varies with frequency from 1.6×10^{16} cm^{-3} at 50 kHz to 1.8×10^{16} cm^{-3} at 10 kHz.

2.5.5 CIS Device Analysis Discussion

The previous sections have presented preliminary measurement results with the objective of understanding the mechanisms that control the photovoltaic performance of CIS junctions. The purpose of this section is to integrate these different types of data into an unified perspective of the CIS device.

Photocarrier generation and collection is evaluated in the first two sections on the optical properties of CIS layers and the spectral response of CIS devices. The CIS spectral response data is fit by Eq. 2-1, using the CIS optical data of J. Tuttle [7], the measured depletion widths, and the measured ZnO optical data. Although not addressed in this report, measurement of CIS spectral response under voltage bias does demonstrate a voltage-dependent quantum efficiency in forward bias which must be considered in the analysis of the fill factor. This voltage dependence also causes J_{sc}-V_{oc} plots to deviate from the dark J-V plots. The solar cell equation without series and shunt resistance would take the form of [9]:

$$J_{light} = J_{dark} - H(V) \cdot J_{photon} \quad (2\text{-}5)$$

and

$$J_{dark} = J_o \, [\exp(qV/nkT) - 1] \quad (2\text{-}6)$$

where J_{light} is the junction current under illumination, J_{dark} is the dark junction current, H(V) is the voltage-dependence of photocarrier collection, and J_{photon} is the absorbed photon current density (for CIS, approximated by J_{sc}).

In general, the junction mechanisms near room temperature for the 400 mV and 450 mV V_{oc} devices evaluated in Section 2.5.3 can be described as recombination controlled with respective diode factors of about 1.9 and 2.1. At low temperatures, the junction currents are less sensitive to temperature, dominated possibly by tunneling or charge injection. A simple expression for recombination controlled Jo in heterojunctions is given by [9]:

$$J_o = J_{oo} \exp(qV_b/nkT) \quad (2\text{-}7)$$

This implies from Eq. 2-3 that E_a equals qV_b/n or inversely that the junction built-in voltage V_b equals $n \cdot E_a/q$. For the 400 mV V_{oc} cell, V_b from J_o equals 0.933 V (1.9·0.491). This agrees with $_0$.931 V, the extrapolation of V_{oc} versus temperature to 0 K,

and with the voltage intercept of 0.938 V from $1/C^2$ versus V. Although the implied values of V_b determined by these three techniques correlate for this cell, further analysis is required to validate these interpretations.

The temperature dependence of V_{oc} derived from Eqs. 2-5, 2-6, and 2-7 is given by:

$$V_{oc}(T) = V_b(T) + n \cdot k \cdot \ln[H(V_{oc}) \cdot J_{sc}(T)/(H(0) \cdot J_{oo})] \cdot T \quad (2\text{-}8)$$

where $V_b(T)$ adjusts for the CIS band gap temperature coefficient (-3.1E-4 eV/K from Ref.10). For the 400 mV V_{oc} cell, the measured V_{oc} temperature coefficient of -1.77 mV/K is consistent with the calculated value of -1.86 mV/K from Eq. 2-8 using data from Section 2.5.3, but neglecting the J_{sc} temperature coefficient and the $H(V_{oc})/H(0)$ terms due to lack of data.

Modeling of the junction reverse saturation current J_{oo} term is currently in progress. Understanding the origin of J_{oo} is essential to improving the CIS V_{oc}. If it is controlled by interface recombination, then passivation of interface states is required. If it is controlled by recombination in the space charge region, then the minority carrier lifetime needs to be improved.

Additional measurements and analysis are required in order to further develop the device model and confirm the interpretations of the data above. These include measurements of the voltage-dependent spectral response to evaluate H(V) and its influence on device fill factor. The temperature coefficients of J_{sc} and the CIS band gap are needed. Van der Pauw measurements of CIS film transport properties versus temperature are required to determine carrier concentrations, carrier mobilities, and the doping activation energy. Measurement of minority carrier diffusion lengths and lifetimes are also required.

2.6 ALTERNATE CIS JUNCTION STUDIES

A Stanford University subcontract is involved in the basic study of the mechanisms controlling performance of CIS-based junctions using CIS/Mo/glass samples supplied by ARCO Solar. This work includes analysis of the transport mechanisms in CIS-based solar cells, investigation of the effects of CdS deposition on the CIS cell performance, evaluation of alternate window layers, and the study of the effects of heat treatment before and after junction formation. Preliminary investigation of ZnS and ZnSe window layers as replacements for CdS indicate that ZnS is too resistive and suppresses photocarrier collection, but that ZnSe warrants further study. Initial results for a cell with a 200 Å thick ZnSe intermediate layer and a thick CdS:In transparent conducting window layer are 7.5% active area (6% total area) efficiency, 430 mV V_{oc}, 29 mA/cm^2 J_{sc}, and 0.532 fill factor under simulated 90 mW/cm^2 Air Mass 1.5 spectrum. At 100 mW/cm^2, the short-circuit current would be 32.2 mA/cm^2. This cell has a dark J_o of 6.8×10^{-8} A/cm^2 and a 1.78 diode factor.

In studies at ARCO Solar, a 10.0% efficient ZnO/50 Å ZnSe/CIS solar cell was fabricated with a 40.9 mA/cm^2 J_{SC}, 382 mV V_{OC}, and 0.64 fill factor, as shown in Fig. 2-25. These initial results are encouraging, but extensive analysis is required to understand the nature and promise of these alternative interfacial layers.

2.7 REFERENCES

1. K.W. Mitchell, Proc. 1st International Photovoltaic Science and Engineering Conf., Kobe, Japan, pp. 691-694 (1984).
2. K.W. Mitchell, Proc. 15th IEEE Photovoltaic Specialists Conf., Kissimmee, FL, pp. 142-146 (1981).
3. A. Rothwarf, Proc. 17th IEEE Photovoltaic Specialists Conf., Kissimmee, FL, pp. 217-222 (1984).
4. K. Mitchell, C. Eberspacher, R. Wieting, J. Ermer, D. Willett, K. Knapp, D. Morel, R. Gay, Proc. Third International Photovoltaic Science and Engineering Conf., Tokyo, Japan, pp. 443-448 (1987).
5. R.R. Potter, C. Eberspacher, L.B. Fabick, Proc. 18th IEEE Photovoltaic Specialists Conf., Las Vegas, NV, pp. 1659-1664.
6. "Terrestrial Solar Spectral Irradiance Tables at Air Mass 1.5 for a 37 deg. Tilted Surface." ASTM Standard E892, 1985 (American Soc. for Testing and Materials, Philadelphia, PA).
7. J. Tuttle, R. Noufi, R.G. Dhere, Proc. Polycrystalline Thin Film Program Meeting, July 20-22, 1987, Lakewood, CO, pp. 127-132 (1987).
8. P.W. Li, R.A. Anderson, R.H. Plovnick, J.Phys. Chem Solids 40:333-334 (1979).
9. K.W. Mitchell, Evaluation of the CdS/CdTe Solar Cell, Doctoral Thesis at Stanford University (1976), Garland Publishing, New York, NY (1979).
10. C. Goradia, M. Ghalla-Goradia, A.M. Hermann, see Ref. 1, pp. 389-392 (1984).

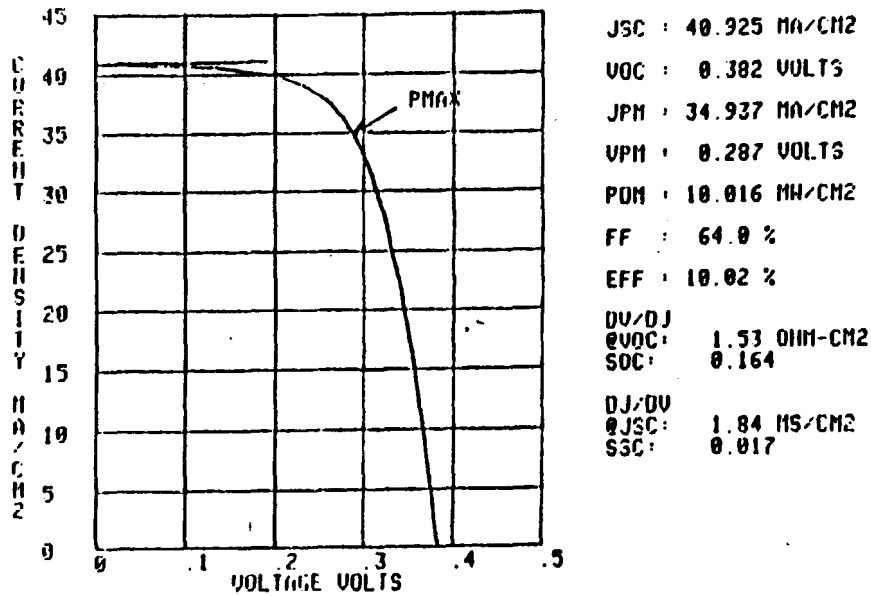

Fig. 2-25. I-V curve of ZnO/50 Å ZnSe/CIS solar cell.

SECTION 3.0
TFS/CIS TANDEM MODULE PROGRESS

3.1 EFFICIENCY RESULTS

The status of the TFS/CIS tandem module research is summarized in this section. Although the primary focus in this initial phase of the contract was on development of the individual TFS and CIS components, substantial results have been demonstrated for the TFS/CIS tandem device structures. A 14.2% active area (4 cm^2) efficiency has been measured on 4-terminal TFS/CIS tandem test structures. A 4-terminal 30×30 cm TFS/CIS tandem module with 10.35 watt output and a 12.3% aperture area efficiency was also achieved.

3.1.1 Background

PV modules with greater than 15% efficiency and less than $2/$watt_{peak}$ cost will be competitive in many markets including central grid-connected energy systems [1,2]. Multiple band gap PV converters have more potential to achieve high efficiencies than single junctions due to better utilization of the photon energy of sunlight. For polycrystalline materials, efficiencies up to 24% are predicted for two-junction tandem solar cells compared with 18% for single junctions [3,4]. Four- and two-terminal projected efficiencies as functions of top cell and bottom cell band gaps are shown in Figs. 3-1 through 3-4 for polycrystalline and TFS materials [3]. CIS with a band gap near 1 eV is an ideal match to TFS at 1.7 eV. Since both TFS and CIS have demonstrated individual device efficiencies above 11%, the combination of the two is a strong candidate for high efficiency thin film module development [5].

The design emphasized in our research is a semitransparent TFS submodule mounted above a CIS submodule. The structure is illustrated in Fig. 3-5. Since this tandem module is formed by laminating two submodules together, the process for each submodule can be individually optimized. The tandem can be designed for either four-terminal or two-terminal operation and the number of cells can be varied to provide either voltage or current matching of the submodules. The glass/glass construction provides a rugged, environmentally durable package.

3.1.2 Tandem Cell Performance

The objective of tandem cell measurements is to evaluate the individual properties of the CIS and semitransparent TFS junctions in both optically stacked and stand-alone configurations. Light I-V and spectral response of the individual cells can be measured. Sixteen 4 cm^2 test cells are fabricated on 10×10 cm glass substrates as two rows of 8 cells each. Metallization grids are used in order to facilitate probing the devices without damage to the junctions and to

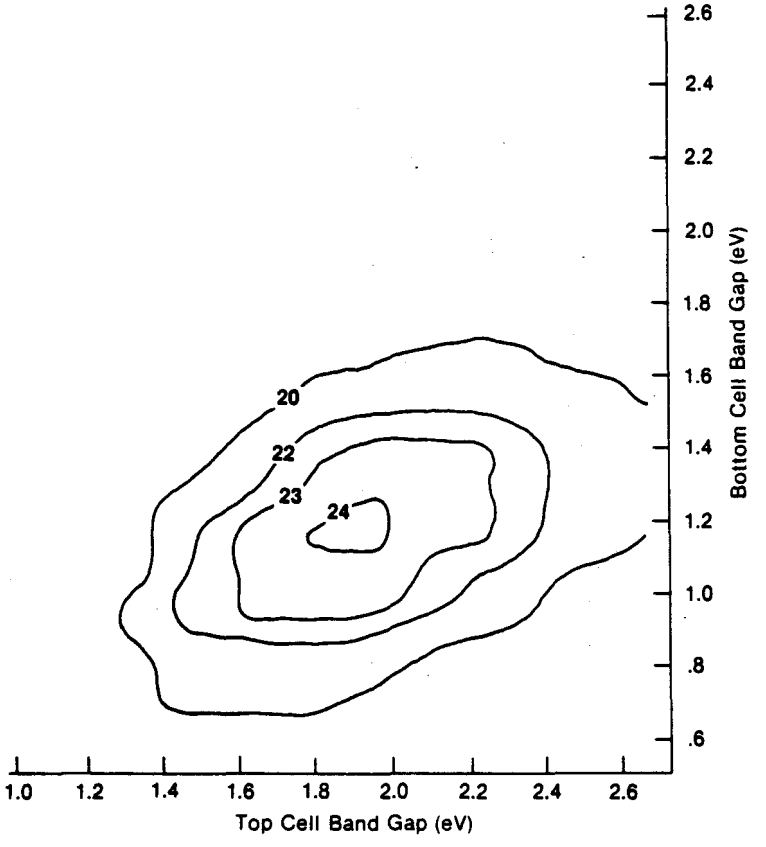

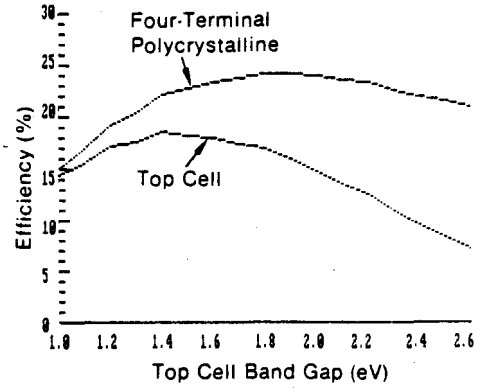

Fig. 3-1. Four-terminal AM 1.5 global PV efficiency for polycrystalline thin film devices.

At left: Multiple-junction efficiency vs top cell and bottom cell band gap.

Above: Top cell and total efficiency vs top cell band gap.

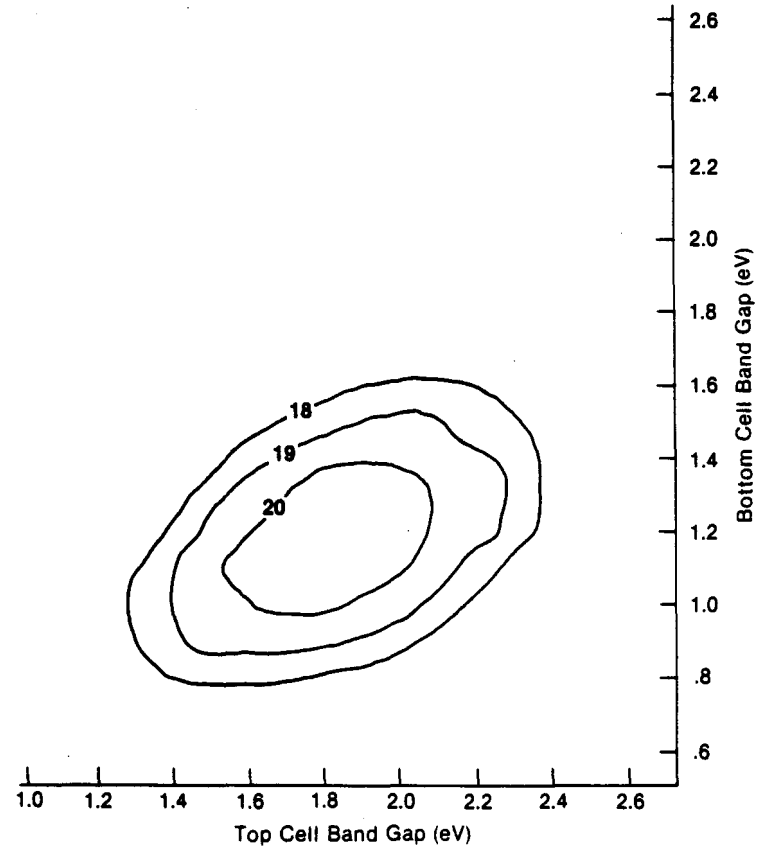

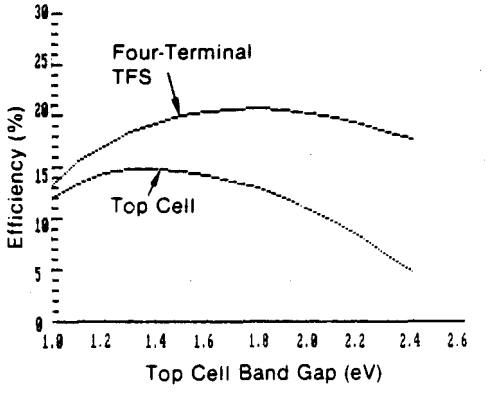

Fig. 3-2. Four-terminal AM 1.5 global PV efficiency for TFS devices.

At left: Multiple-junction efficiency vs top cell and bottom cell band gap.

Above: Top cell and total efficiency vs top cell band gap.

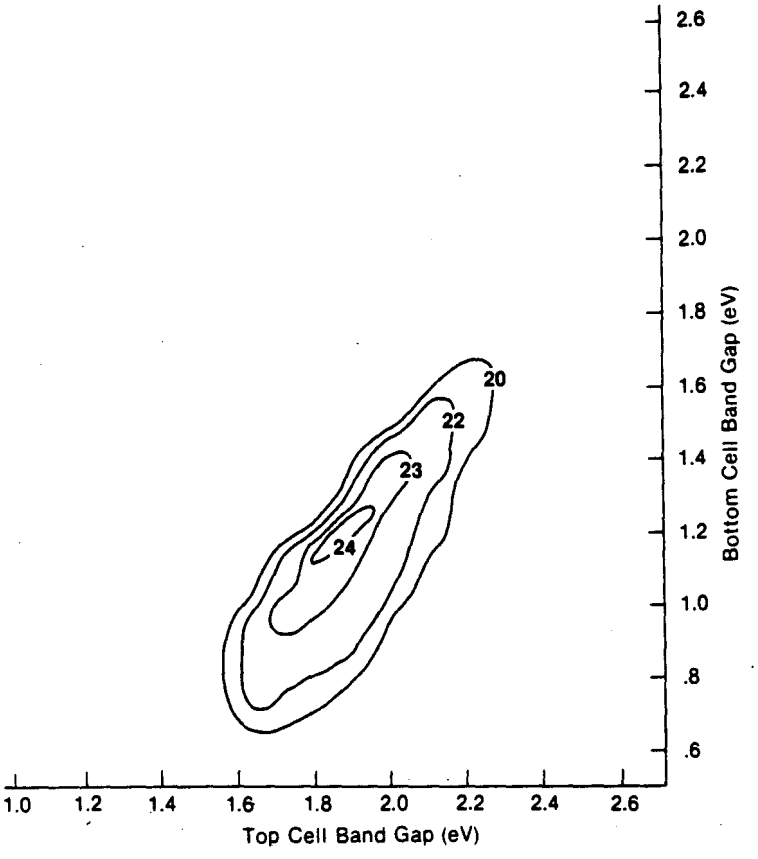

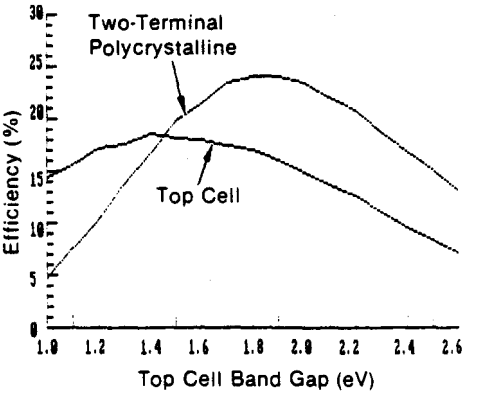

Fig. 3-3. Two-terminal AM 1.5 global PV efficiency for polycrystalline thin film devices.

At left: Multiple-junction efficiency vs top cell and bottom cell band gap.

Above: Top cell and total efficiency vs top cell band gap.

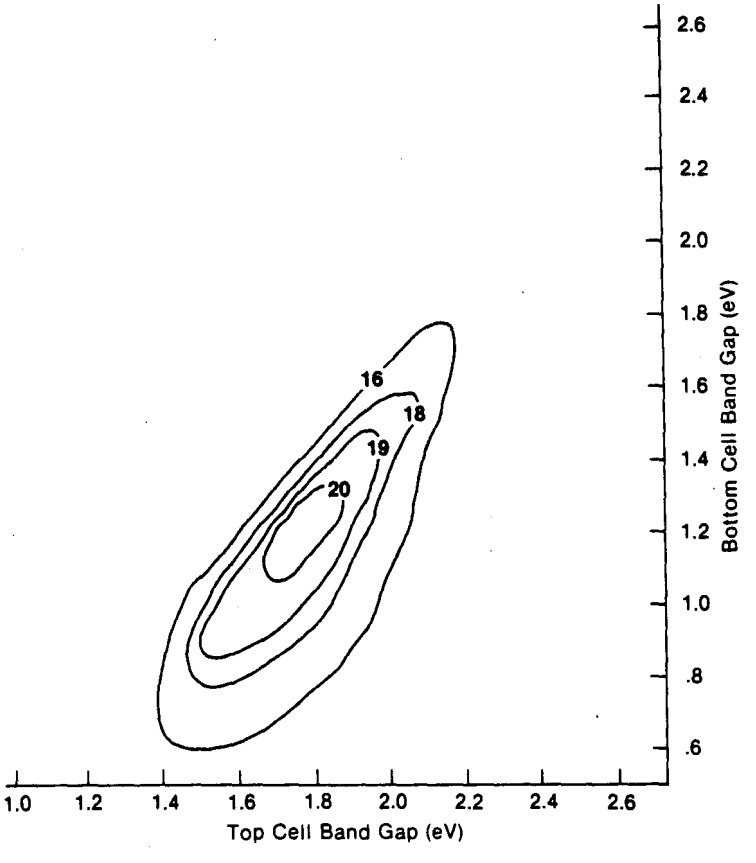

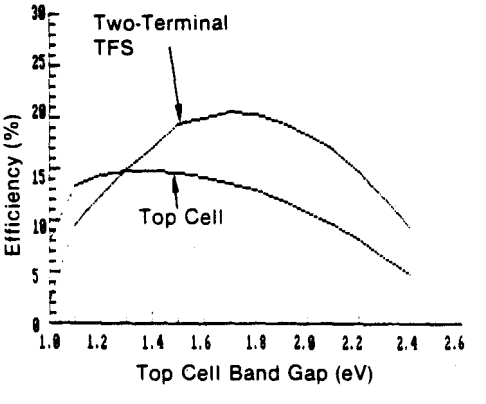

Fig. 3-4. Two-terminal AM 1.5 global PV efficiency for TFS devices.

At left: Multiple-junction efficiency vs top cell and bottom cell band gap.

Above: Top cell and total efficiency vs top cell band gap.

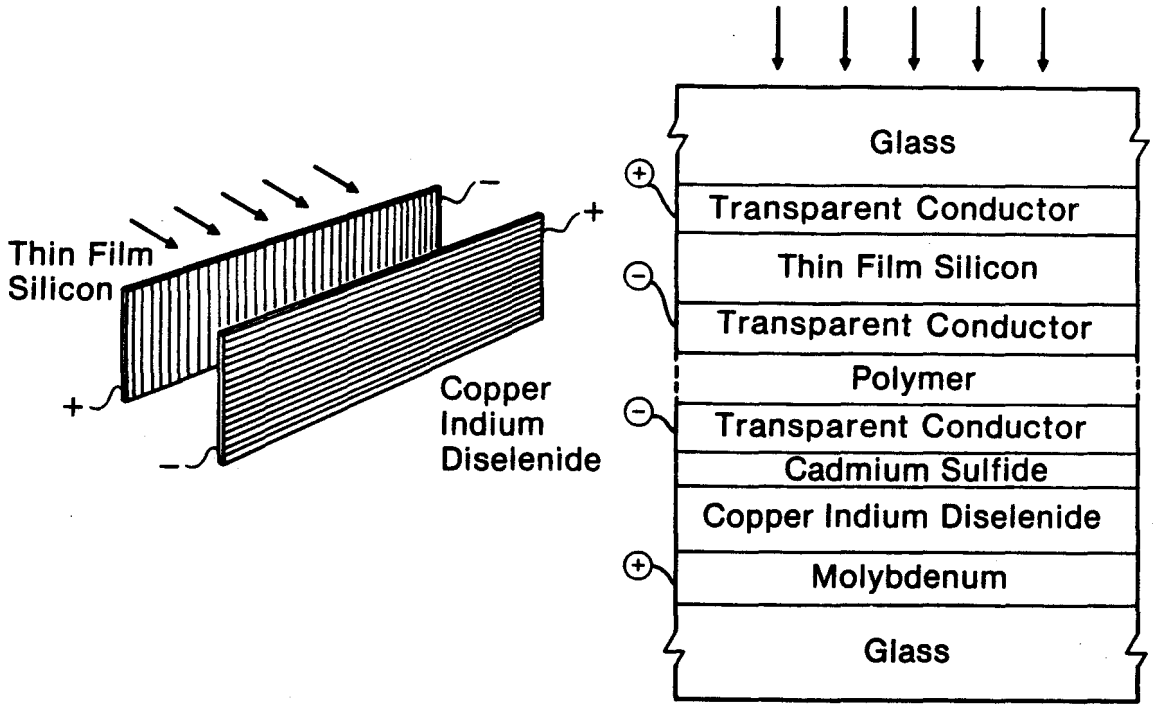

Fig. 3-5. Cross section of tandem module.

minimize series resistance losses from the transparent electrodes. One TFS cell on each test structure substrate does not have grids in order to be used as an TFS optical filter over CIS cells for CIS bottom cell tandem measurements. Existing fixturing and automated data acquisition are utilized. The analysis is based on active area in order to compare with module cell segments that have no grids.

A four-terminal tandem efficiency of 14.2% on 4 cm^2 has been demonstrated as summarized in Table 3-1. The semitransparent TFS cell is 9.62% efficient with a 15.8 mA/cm^2 J_{SC}, an 862 mV V_{OC}, and 0.705 fill factor. The filtered CIS cell contributes 4.55% efficiency with a 17.6 mA/cm^2 filtered J_{SC}, a 392 mV V_{OC}, and 0.66 fill factor. The stand-alone CIS cell is 8.71% efficient with a 33.0 mA/cm^2 J_{SC}, 411 mV V_{OC}, and 0.642 fill factor. The filtered-to-standalone CIS J_{SC} current ratio of 0.53 is high because of the use of a thick CdS window layer which reduces the stand-alone J_{SC}. The highest measured filtered CIS J_{SC} is 18.4 as documented by its spectral response curve shown in Fig. 2-1. The change in CIS V_{OC} from 411 mV to 392 mV and the increase in fill factor upon shadowing the cell with the semitransparent TFS cell is consistent with the CIS junction I-V and the reduced ZnO series resistance loss at the lower operating current.

3.1.3 Tandem Module Performance

Preliminary results for 30x30 cm tandem modules are promising. Power output higher than 10 watts has been achieved as summarized in Table 3-2. Based on aperture areas of 843 cm^2, the 7.69 watt

and 2.66 watt contributions from the TFS and CIS submodules translate to efficiencies of 9.1% and 3.2% respectively, for a total 12.3% aperture area efficiency. These data are measured at 25°C on a Spectrolab LAPSS calibrated to 100 mW/cm^2 ASTM air mass 1.5 global spectrum with an optical air gap between the two modules of about 2 cm.

The stand-alone CIS module produces 7.62 watts with 9.0% aperture area efficiency, a 611 mA I_{SC}, a 21.15 V V_{OC} (423 mV V_{OC} per cell), and a 0.59 fill factor. The semitransparent TFS module is 9.1% efficient with a 262 mA I_{SC}, a 43.45 V V_{OC} (869 mV V_{OC} per cell), and a 0.675 fill factor. The lower module fill factors compared to the test structures result from interconnect series resistance losses and to cell-to-cell variations as discussed in Section 2.4.5.

Table 3-1. 4-terminal tandem cell (4 cm^2) performance.

Device	Eff. (%)	J_{SC} (mA/cm^2)	V_{OC} (mV)	FF
Semitransparent TFS	9.62	15.8	862	70.5
Filtered CIS	4.55	17.6	392	66.0
Tandem	14.17%			
Stand-alone CIS	8.71	33.0	411	64.2

*ASTM air mass 1.5, global 100 mW/cm^2, 25°C.

Table 3-2. 4-terminal tandem module performance.

Type	Power (W)	Area** (cm^2)	Eff. (%)	I_{SC} (mA)	V_{OC} (V)	FF
Semitransparent TFS	7.69	843	9.1	262	43.45	0.675
Filtered CIS	2.66	843	3.2	228	19.15	0.608
Tandem	10.35		12.3			
Stand-alone CIS	7.62	844	9.0	611	21.15	0.590

*ASTM air mass 1.5, global 100 mW/cm^2, 25°C.
**Aperture area.

3.2 PERFORMANCE ANALYSIS

Performance model predictions for tandem photovoltaic modules show that substantial gains in the efficiency of PV modules can be made by coupling two absorbing systems together in a common module structure.[1-5] There are several important assumptions made in developing the model which require experimental testing to verify the range over which they are valid and the degree to which the model can predict performance. From an optical standpoint these assumptions are:

1. that the light in the absorption bands of both absorbers is efficiently coupled into the front cell;
2. that the light usable by the front absorber is efficiently converted into current;
3. that the light below the band gap of the front absorber is transmitted efficiently through the front absorber to the bottom absorber;
4. that the back absorber efficiently couples with the light to which it responds.

These assumptions are not necessarily consistent with the implied goal of optimizing the electrical performance of each of the absorber systems. For instance, there is a tradeoff of optical transmission and conductivity for most transparent conductors. High conductivity due to high carrier concentration causes high absorption losses in the near IR region due to plasma mode absorption of the free electrons. It is necessary to carry out a detailed investigation of the validity of the above assumptions under a range of cell fabrication parameters in order to be able to optimize the performance of tandem modules.

The model used to describe the optical transmission through the various layers does not take into account the detailed interference effects expected for thin films [1,6]. This is done because it is assumed that the interference effects will be averaged out over the wavelength range of each of the absorption bands of the tandem PV systems. In addition, the presence of rough surfaces in the thin film stack can significantly enhance the absorption in the active layers. The effect on tandem performance due to the presence of these rough surfaces must be determined to be able to examine the tradeoff of top cell performance versus bottom cell performance as a function of the surface roughness.

The description of the module being developed, as found in Section 3.1, shows that the two thin film absorber systems are separated by a layer of relatively thick organic material. This simplifies the optical coupling of the two systems because the coupling is incoherent. That is, the phase of the light as it traverses the thin film top absorber system is uncorrelated with the phase of the light as it traverses the bottom absorber system. The expected thin film interference effects then only need be evaluated for each system separately.

3.2.1 Simplified Performance Model

The optical model used in this study has been greatly simplified to highlight the primary dependencies of module performance on important parameters. There are two components of the model: a light transmission model and a carrier generation model. Figure 3-6 shows a view of the construction details of a thin film hybrid module. The top circuit, based on thin film silicon (TFS), is deposited on a glass substrate which faces towards the incident light. The bottom circuit, based on CIS, is deposited on a second piece of glass. The two systems are laminated together using a plastic material, ethylene vinyl acetate (EVA). Figure 3-7 shows the important optical factors in this system. The glass/TFS system acts optically as a front absorber with a characteristic transmission, T_1, front reflection, R_1, and back reflection, S_1. The absorption in the front combination is calculated by the formula:

$$A_1 = 1 - R_1 - T_1. \qquad (3\text{-}1)$$

The CIS/glass system has two important characteristics, a front reflection, R_2 and an absorption A_2. There is no transmission because of the bottom molybdenum layer. The only directly measurable optical parameter for the CIS/glass system is R_2. A_2 can be estimated from the quantum efficiency of the CIS device if assumptions about the depletion width can be made. (See Section 3.1)

It is important to note, as Fig. 3-7 shows, that the reflections S_1 and R_2 occur on interior surfaces where the index of refraction is not that of air but that of EVA. The index of refraction of EVA is about 1.5. This has the effect of lowering the reflectivity at these boundaries compared to that found with air boundaries.

The current generated in the TFS cell at each wavelength can be written as follows:

$$J_L(TFS,\lambda) = [1-R_1(\lambda)]\cdot[\exp(-\alpha_{ZnO}(\lambda)\cdot t_{ZnO})]\cdot[\exp(-\alpha_p(\lambda)\cdot t_p)]\cdot [1-\exp(-\alpha_i(\lambda)\cdot t_i)]\cdot q\cdot\Gamma(\lambda) \qquad (3\text{-}2)$$

where:

R_1	is the front reflectance of the glass/TFS combination
$\alpha_{ZnO}(\lambda)$	is the absorption coefficient for the ZnO
t_{ZnO}	is the thickness of the ZnO
$\alpha_p(\lambda)$	is the absorption coefficient of the p-layer
t_p	is the thickness of the p-layer
$\alpha_i(\lambda)$	is the absorption coefficient of the i-layer
t_i	is the thickness of the i-layer
q	is the electronic charge
$\Gamma(\lambda)$	is the photon flux of the radiation in units of photons/cm^2-sec.

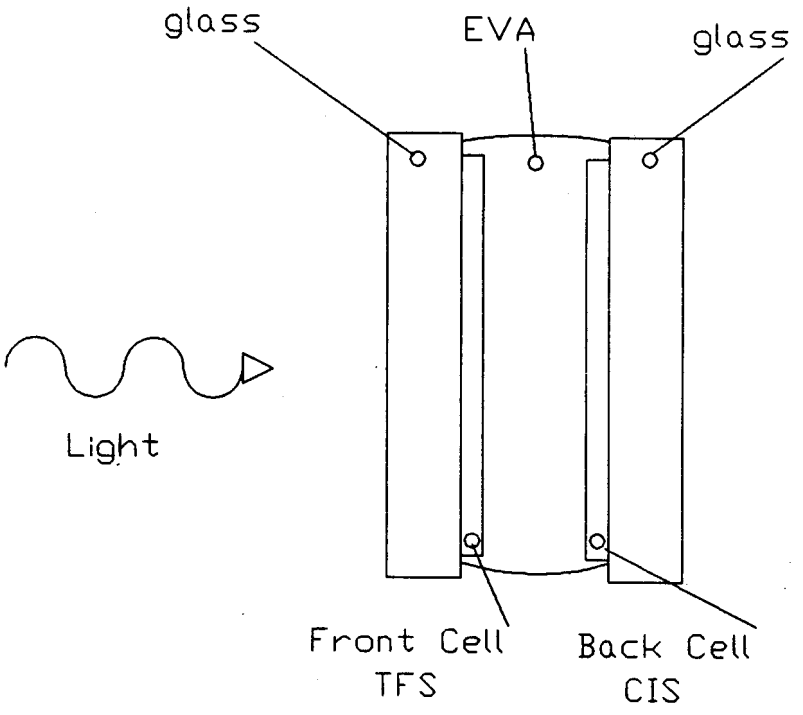

Fig. 3-6. Hybrid tandem module cross section.

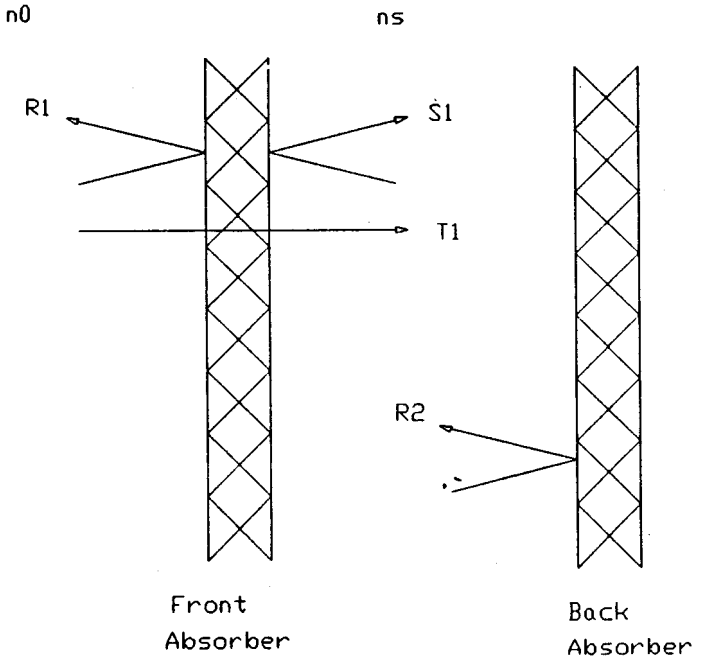

Optical Factors in Tandem Cells

Fig. 3-7. Optical factors in a laminated tandem structure.

The photon flux function used in this study is based on the SERI AM1.5 global (1983) spectrum. The use of Eq. 3-1 to calculate a spectrally integrated current density assumes that the effects of thin film interference are averaged out over the absorption band of the TFS. A more proper method for the calculation of the current density would use the method of characteristic matrices such as described in [7]. However, for the purposes of this initial survey the complications of this approach are not required.

The current generated in the CIS cell can be calculated on a similar basis:

$$J_L(CIS,\lambda) = T_1(\lambda)\cdot[1-R_2(\lambda)]\cdot[\exp(-\alpha_{ZnO}(\lambda)\cdot t_{ZnO})]\cdot [1-\exp(-\alpha_{CIS}(\lambda)\cdot W_{CIS}]\cdot q\cdot\Gamma(\lambda) \qquad (3-3)$$

where:

$T_1(\lambda)$	is the transmission of light through the TFS stack
$R_2(\lambda)$	is the reflection off the front CIS stack surface
$\alpha_{CIS}(\lambda)$	is the absorption coefficient of the CIS
W_{CIS}	is the depletion layer thickness of the CIS.

A direct calculation of the transmission through the TFS layer is difficult because of the problems in modeling the optical properties of the rough surfaces found in the TFS stack. As will be seen in subsequent development, the measured transmission will be used for comparative performance purposes. Integration of Eq. 3-1 and 3-2 over the incident spectral range yields the current density. From an optical point of view the important parameters are R_1, T_1, A_1, R_2 and A_2.

The objective of the subsequent analysis is to develop a set of easily obtained measures which can be used to predict the performance of the two elements of the tandem system in combination. The measures used in this study are weighted averages of the measured transmission and reflection values for the separate cells in a laminated configuration. One outcome of this approach is to obtain an estimate of the optical losses in the system which decrease the power output from that expected. By examining the dependence of these losses on film parameters it is possible to determine the elements of the system which can be improved.

3.2.2 Weighted Optical Quantity Average Calculation Method

We would like to obtain a set of optical parameter numbers for each thin film configuration fabricated that are simple to measure or calculate and that capture most of the variations between samples. For the TFS case we require that the weighting function employed depends on the quantum efficiency of the TFS and the SERI AM1.5 global spectrum as shown in Eq. 3-4, 3-5, and 3-6. The quantum efficiency for TFS used in the average is from

a very good cell shown in Fig. 3-8a. The weighting value for the spectrum is in units of photons/μm-cm^2-sec.

$\langle T_1 \rangle_{tfs}$ is a measure of the light which is transmitted through the TFS stack which could have been used by the top TFS cell. This number should depend significantly on the i-layer thickness. $\langle R_1 \rangle_{tfs}$ is a measure of the radiation which is reflected from the front optical combination surface which could have been used by the TFS cell. This value should be as small as possible. For the optical configuration used in hybrid tandem modules $\langle S_1 \rangle_{tfs}$ has little importance.

$$\langle T_1 \rangle_{tfs} = \frac{\int T_1(\lambda) \cdot QE_{tfs}(\lambda) \cdot I_{SERI}(\lambda)\, d}{\int QE_{tfs}(\lambda) \cdot I_{SERI}(\lambda)\, d} \qquad (3\text{-}4)$$

$$\langle R_1 \rangle_{tfs} = \frac{\int R_1(\lambda) \cdot QE_{tfs}(\lambda) \cdot I_{SERI}(\lambda)\, d}{\int QE_{tfs}(\lambda) \cdot I_{SERI}(\lambda)\, d} \qquad (3\text{-}5)$$

$$\langle S_1 \rangle_{tfs} = \frac{\int S_1(\lambda) \cdot QE_{tfs}(\lambda) \cdot I_{SERI}(\lambda)\, d}{\int QE_{tfs}(\lambda) \cdot I_{SERI}(\lambda)\, d} \qquad (3\text{-}6)$$

The case for the CIS averaging is a little more complicated. We require that the averaging process accounts for the absorption of the radiation in the TFS band that the CIS cannot receive as well as for the absorption of the radiation in the band that it can use. A simple way to do this is to construct a weighting function which is a product of the quantum efficiency of a standard CIS cell with the difference between 1 and the quantum efficiency of the standard TFS cell. Equations 3-7 through 3-10 show these averages. The TFS part of the average is normalized by dividing each QE_{tfs} value by the maximum QE_{tfs} value in the TFS band.

$$\langle T_1 \rangle_{cis} = \frac{\int T(\lambda) \cdot (1 - QE_{tfs}(\lambda)/QE_{tfs}(max)) \cdot QE_{cis}(\lambda) \cdot I_{SERI}(\lambda)\, d}{\int (1 - QE_{tfs}(\lambda)/QE_{tfs}(max)) \cdot QE_{cis}(\lambda) \cdot I_{SERI}(\lambda)\, d} \qquad (3\text{-}7)$$

$$\langle R_1 \rangle_{cis} = \frac{\int R_1(\lambda) \cdot (1 - QE_{tfs}(\lambda)/QE_{tfs}(max)) \cdot QE_{cis}(\lambda) \cdot I_{SERI}(\lambda)\, d}{\int (1 - QE_{tfs}(\lambda)/QE_{tfs}(max)) \cdot QE_{cis}(\lambda) \cdot I_{SERI}(\lambda)\, d} \qquad (3\text{-}8)$$

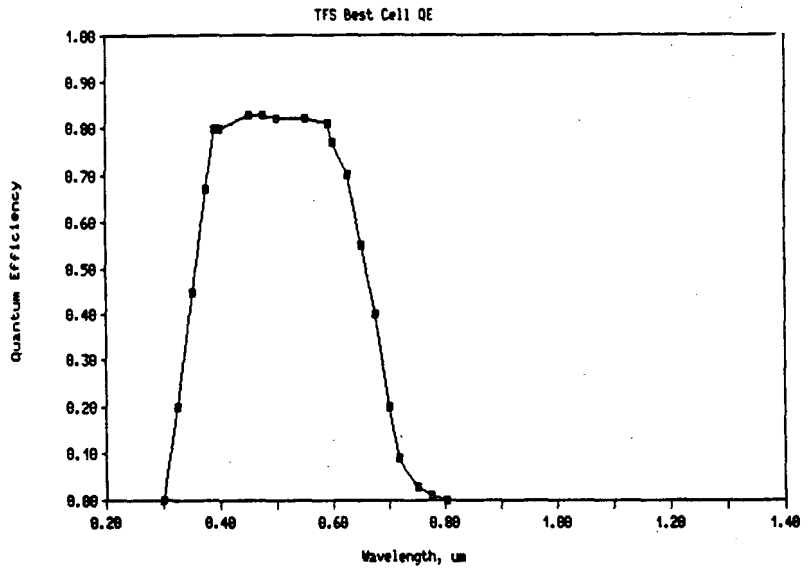

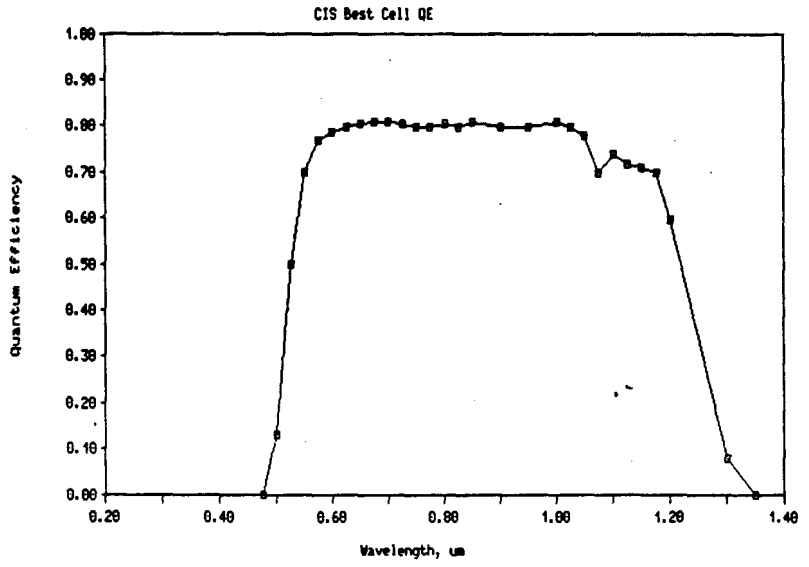

Fig. 3-8. Quantum efficiencies used for weighting calculations.

$$\langle S_1 \rangle_{cis} = \frac{\int S_1(\lambda) \cdot (1-QE_{tfs}(\lambda)/QE_{tfs}(max)) \cdot QE_{cis}(\lambda) \cdot I_{SERI}(\lambda)\ d}{\int (1-QE_{tfs}(\lambda)/QE_{tfs}(max)) \cdot QE_{cis}(\lambda) \cdot I_{SERI}(\lambda)\ d} \quad (3\text{-}9)$$

$$\langle R_2 \rangle_{cis} = \frac{\int R_2(\lambda) \cdot (1-QE_{tfs}(\lambda)/QE_{tfs}(max)) \cdot QE_{cis}(\lambda) \cdot I_{SERI}(\lambda)\ d}{\int (1-QE_{tfs}(\lambda)/QE_{tfs}(max)) \cdot QE_{cis}(\lambda) \cdot I_{SERI}(\lambda)\ d} \quad (3\text{-}10)$$

$\langle T_1 \rangle_{cis}$ is a measure of the radiation which passes through the TFS stack which can be used by the CIS cell. This value includes the losses due to all absorption processes in the TFS stack as well as losses due to scattering as might be expected from rough surfaces. This parameter is similar to the filter quality factor, Q_f, calculated by Tanner et al.(1) and discussed in Section 1. The primary differences are the use of a measured QE_{cis} value in our case instead of assuming a value of 1.0 and the use of a standardized cut-off factor to sharply extinguish radiation that the CIS cell never sees. As will be seen later, similar values are calculated. We expect that the values of $\langle T_1 \rangle_{tfs}$ calculated here will be lower. $\langle R_1 \rangle_{cis}$ is measure of the radiation which is reflected from the front of the tandem module which the CIS cell could use but does not receive. $\langle R_2 \rangle_{cis}$ is a measure of the radiation which is reflected from the CIS stack surface in the useful CIS band. $\langle S_1 \rangle_{cis}$ could be used to estimate the amount of reflected radiation from the front CIS surface which is returned to the CIS. The returned radiation fraction is generally less than 2-4% of that initially transmitted through the TFS stack.

3.2.3 Experimental Description

In a tandem module the top cell stack can be regarded as a filter which obscures the bottom cell. There are several factors which influence the combined performance of the two cells. In order to assess the relative importance of different factors on the performance of cells in a tandem module configuration a series of top TFS cells were fabricated with different layer thicknesses. By placing these 'filters' in front of a standard CIS cell the individual cell and tandem module performance was measured as a function of the variation in the TFS device layer thicknesses.

The experiment may be regarded as a three factor, three level test in which three layers: the front transparent conductor layer, the TFS i-layer, and the back transparent conductor layer were each fabricated with three different thicknesses as shown in Table 3-3.

Table 3-3. Factors and levels for TFS filters.

Layer	Thickness Range, micron
i-layer	0.15, 0.25, 0.35
Front TC	0.5, 1.0, 1.5
Back TC	0.5, 1.0, 1.5

The cell structure for the TFS device was glass/ZnO/pin/ZnO. Twenty seven 10x10 cm test structures of 15 cells each were fabricated using the cell pattern shown in Fig. 3-9a. The individual cells were approximately 0.8x4.2 cm in dimension. One of the positions was not converted into a cell so that it could be used as a window for the filter function in a tandem stack. Current-voltage measurements were made on all of the cells of the 27 test structures. The averaged values of the cell parameters were used as a basis for comparison of the effects of the variation in layer thickness on TFS cell performance. The test structures were laminated with EVA to 10x10 cm pieces of glass in order to assure that the optical configuration of the tandem cell measurements corresponded as closely as possible to the configuration in modules. Figure 3-10 shows the method to couple the TFS window to the standard CIS cell. The CIS cell was also laminated to a piece of clear glass with EVA. The two cell systems were coupled using the liquid glycerol. No reflections were expected at the various interfaces since glycerol, EVA and glass all have an index of refraction of 1.5 over the spectral range used. None of these materials absorbs light significantly in the spectral band from 0.3 to 1.3 micron. Thus the tandem test cell configuration in Fig. 3-10 is optically equivalent to the module configuration in Fig. 3-6. The advantage of this method is that many measurements can conveniently be made with the different TFS filters on top of the same CIS cell. The CIS test structure, as shown in Fig. 3-9b, consists of a laminated set of CIS cells of slightly smaller size than that found in the TFS test structure. The cell structure used for the CIS cell was: ZnO/CdS/CIS/Mo/glass. Leads were brought out before the lamination process to allow I-V and spectral response measurements to be made under different filter conditions.

Forward transmission and front and back surface reflection measurements were made on each of the 27 TFS cell stacks at position 13 on the test structure using a Perkin-Elmer Model 330 spectrophotometer from 0.3 to 1.8 micron. The front surface reflection of a CIS cell was also measured. These data were averaged using the weighting functions described in Eq. 3-4 through 3-10. The I-V curve was measured for a standard CIS cell without any filter and then with each of the 27 filters optically coupled on top. The quantum efficiency of the standard CIS cell was measured without a filter and with a selected set of three filters. The predicted integrated current density was used to verify the calibration of the light sources and monitor cells.

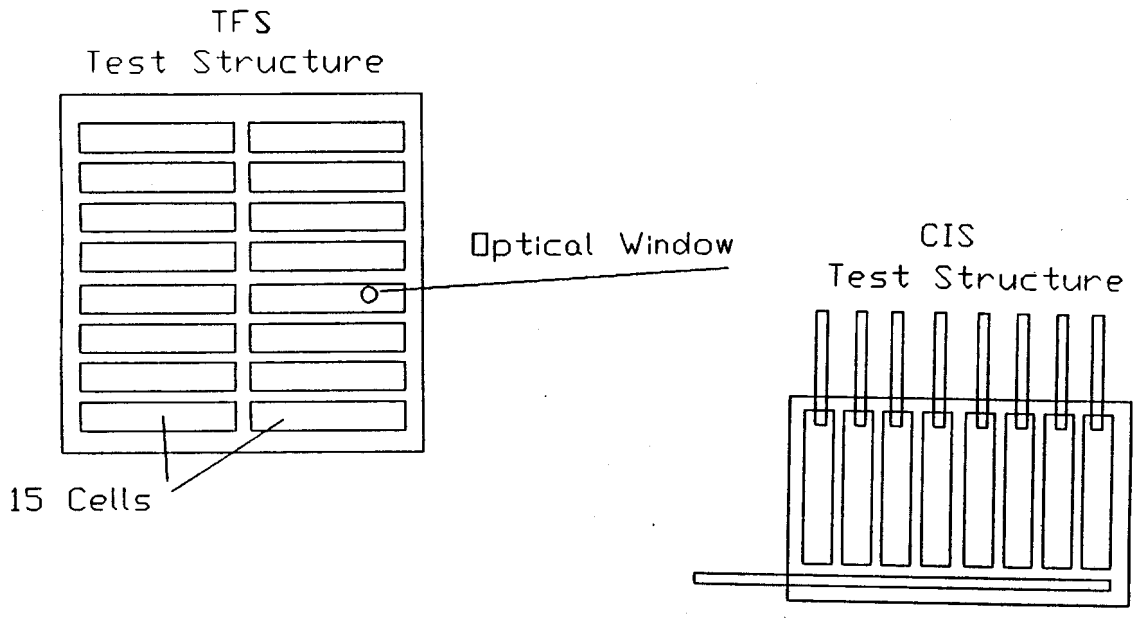

Fig. 3-9. Configuration of test structures for optical experiments.

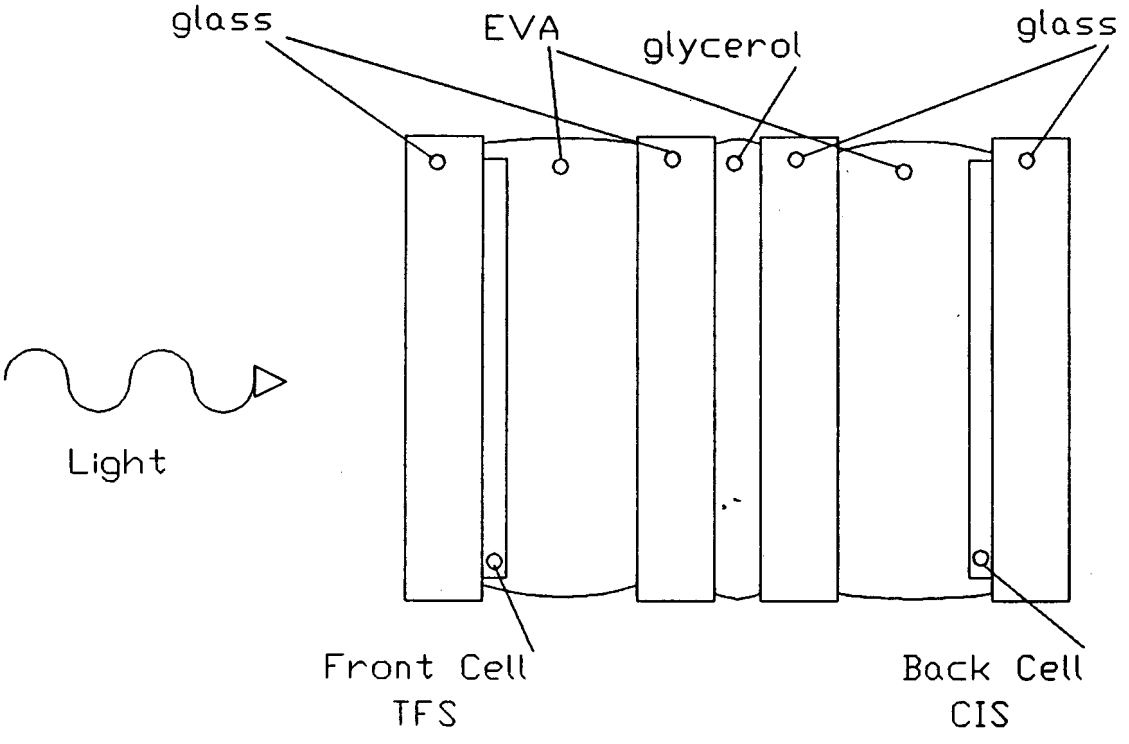

Fig. 3-10. View of optically coupled tandem test structures.

The results of these experiments are described in the next section.

3.2.4 Experimental Results

3.2.4.1 Optical Data

The transmission spectrum through the thinnest set of TFS device layers is shown as an example in Fig. 3-11. The undulations in the curve are interference fringes due to the thin film nature of the layers in the device. The transmission curve is quite similar to that reported by Tanner in their Fig. 4. Figure 3-12 shows the reflectance curve from a CIS cell structure. The rise in reflectivity above 0.9 micron is probably due to the anomalous dispersion at the onset of the plasma mode of absorption in the zinc oxide front transparent conductor. The value for $\langle R_2 \rangle_{cis}$ is 0.12 indicating that 12% of the light transmitted through the TFS stack is reflected away and not used by the CIS device.

The effect of varying front TC thickness on transmission is shown in Fig. 3-13. The strong decrease in the transmission with increased ZnO thickness at the TFS band edge is due to scattering of the radiation by the very rough ZnO surface. Figure 1-5 in Section 1 shows a SEM picture of a typical ZnO surface for a 1.28 micron layer. The enhanced Jsc of devices with thicker front ZnO layers is due to the scattering of light which is thought to cause an increase in absorption path length and light trapping. The correlation with front layer thickness and Jsc will be discussed later. Another effect which Fig. 3-13 shows is the increase in the IR absorption by thicker layers due to the plasma absorption process. These spectra show that the thicker, more scattering layers should have a strong effect on the CIS device performance.

The spectra in Fig. 3-14 show that the back ZnO TC layer on the TFS device has little effect on the increase of absorption in the TFS region, and that there are significant increases in near IR absorption for thicker layers as found for the front TC layer. The optimization process for the front cell requires the use of TC layers with the lowest sheet rho. The IR optical absorption has little impact on the performance of the TFS cell since it occurs outside of the TFS absorption band. Thus, the use of 1.5 micron, 9 ohm/[] ZnO TC layers is optimal for good TFS performance. We would expect that these thick layers would have an adverse effect on CIS performance in a tandem configuration.

The effect of varying i-layer thickness is much more complex as is shown in Fig. 3-15. At the band edge an effective shift of the absorption edge towards longer wavelengths is seen with thicker layers as expected. It would be expected that the TFS device short circuit current would increase. The thickness of the i-layer has an unexpectedly large effect on the transmission in the CIS absorption region with thicker layers being more absorbing. This effect does not have a simple explanation, but

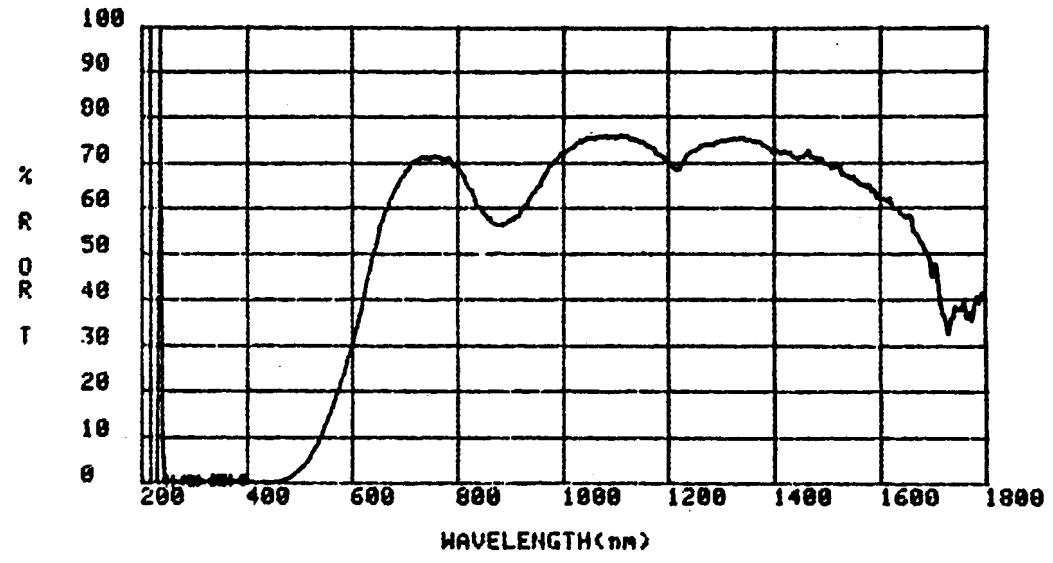

Fig. 3-11. Example of transmission spectrum.

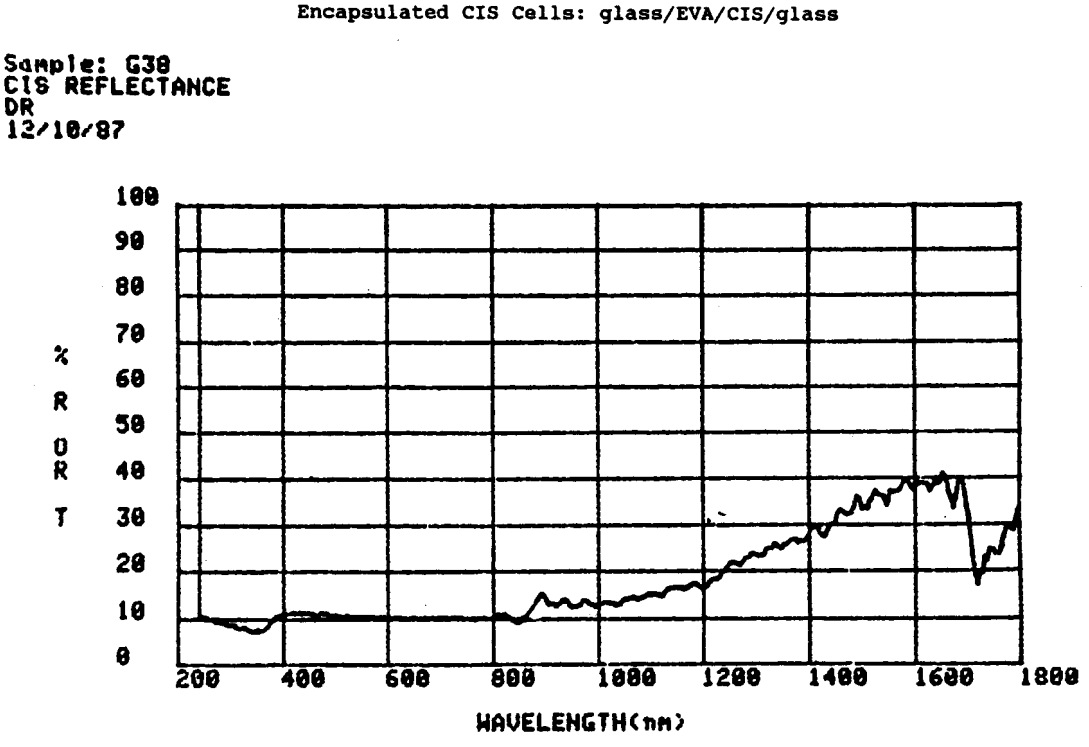

Fig. 3-12. Example of reflection spectrum.

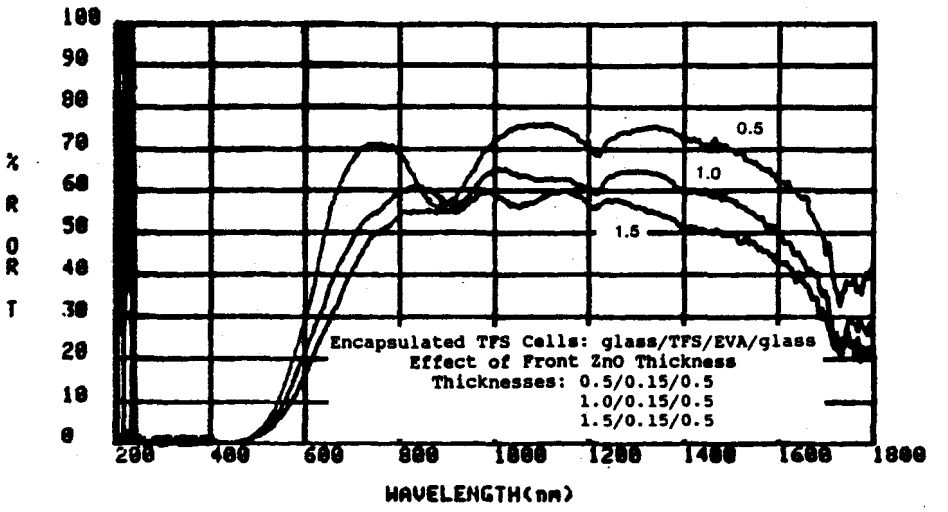

Fig. 3-13. Overlay of transmission spectra showing dependence on front ZnO transparent conductor thickness.

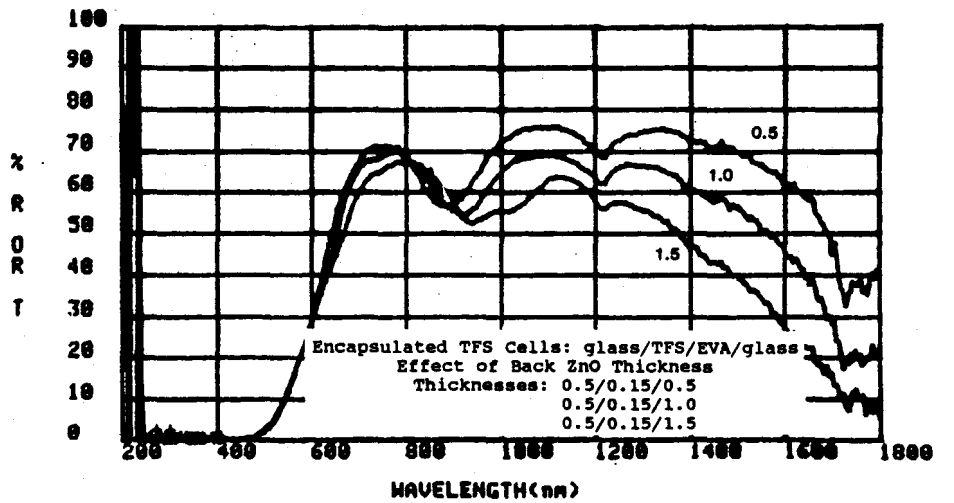

Fig. 3-14. Overlay of transmission spectra showing dependence on back ZnO transparent conductor thickness.

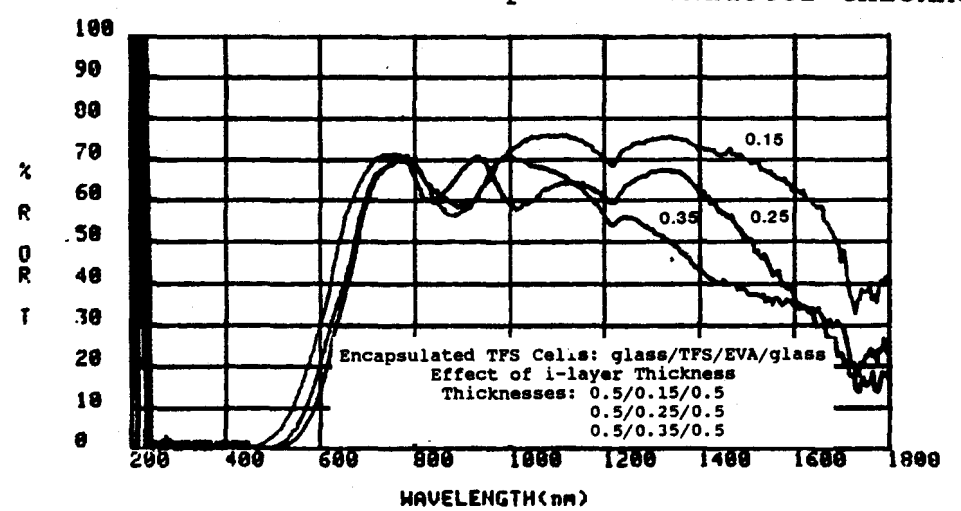

Fig. 3-15. Overlay of transmission spectra showing dependence on i-layer thickness.

probably depends on the details of optical interference patterns in the thin layers.

Figures 3-16 through 3-18 show a series of reflection spectra for the same range of thicknesses considered in Figs. 3-13 through 3-15. Several important comments can be made. The thinnest layer set 0.5/0.15/0.5 shows a large reflectance bump around 900 nm. This bump is apparently caused by a large mismatch in the indices of refraction of the layers in the TFS stack in this wavelength region. Detailed optical modeling will be required to ferret out the source of this feature. All of the thicker TC examples show an increased reflectance in the near IR region which goes along with the decreased transmission described earlier. All of the examples show that significant reflection occurs in the CIS absorption region from 0.6 to 1.3 micron. The spectrum for the thick i-layer case in Fig. 3-18 shows a very strong reflectance at 1400 nm which is connected with the unusually low transmission seen in Fig. 3-15 for this case.

These examples show dramatic optical effects for various thicknesses of the TFS device layers. However, it is difficult visually to compare the relative importance of each band with actual performance. This can be done using the integrated, weighted data described in the next section.

3.2.4.2 Averaged Optical Data and Cell Data

Examples of the values of the factors in the integrals for $\langle R_1 \rangle_{tfs}$ and $\langle R_1 \rangle_{cis}$ are shown in Figs. 3-19 and 3-20. The squares are the measured data, the solid lines the value of the weighting factor, and the diamonds the product of the weighting factor and the data. The ratio of the area under the diamond curve to that under the solid curve is equal to the average value to be calculated.

Table 3-4 contains the values calculated for the most important of the averages for the various TFS device layer configurations. Tables 3-5 and 3-6 contain the cell parameter values measured for the TFS devices and the CIS device respectively. Table 3-7 shows the TFS and CIS cell and calculated tandem efficiency as they depend on the TFS device parameters. The tandem efficiency is calculated simply as the sum of the individual cell efficiencies.

The first assumption to check is that the measured Jsc for the CIS cell is proportional to $\langle T_1 \rangle_{cis}$. If this assumption fails the use of the averaged quantities is not worth while. Figure 3-21 shows that the filtered CIS current is proportional to the average transmittance in the CIS absorption band as predicted. The range of $\langle T_1 \rangle_{cis}$ from 0.37 to 0.66 is considerable. Another check on the validity of the assumptions is to compare $\langle T_1 \rangle_{cis}$ to the ratio of the filtered current to the unfiltered current. Ideally the data should fall on the unit straight line. Figure 3-22 shows that the data are linear in this respect, but that the

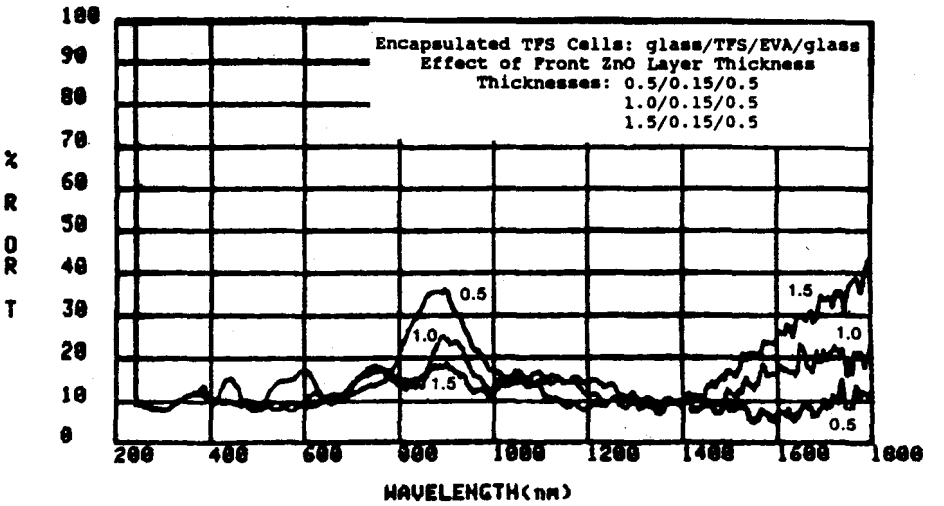

Fig. 3-16. Overlay of reflection spectra showing dependence on front ZnO transparent conductor thickness.

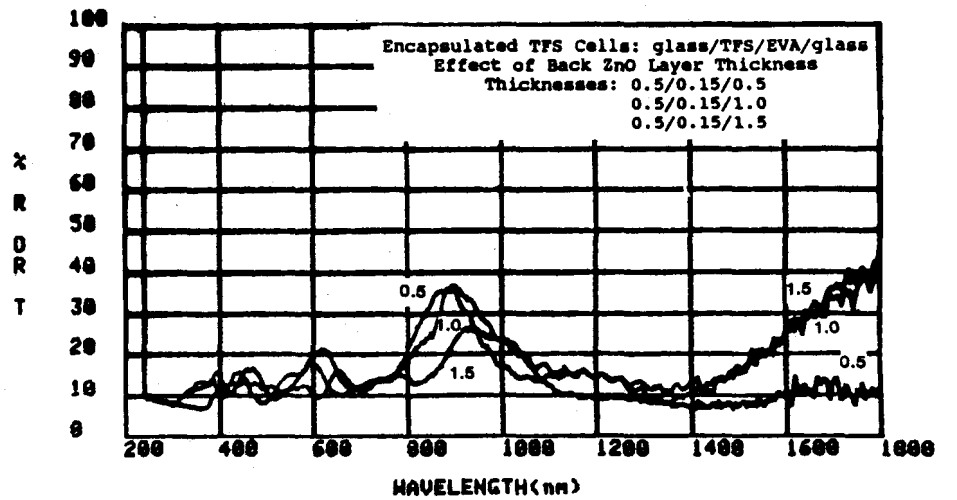

Fig. 3-17. Overlay of reflection spectra showing dependence on back ZnO transparent conductor thickness.

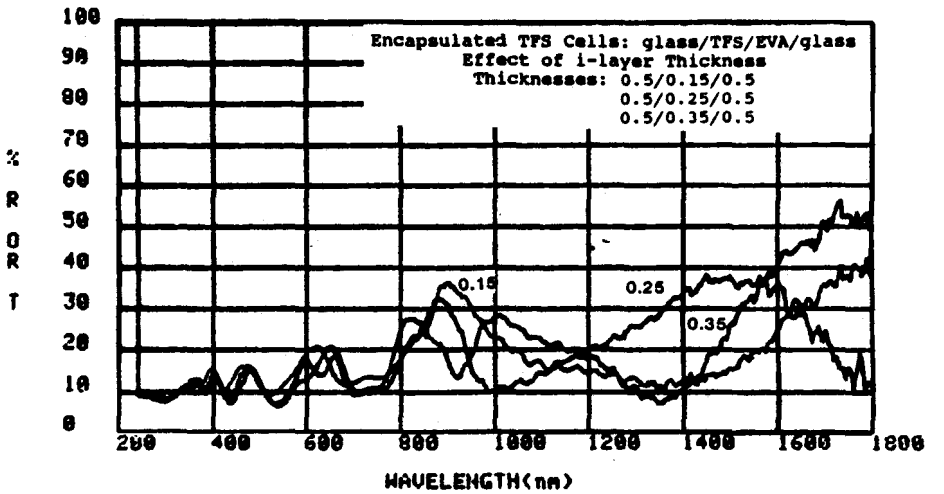

Fig. 3-18. Overlay of reflection spectra showing dependence on i-layer thickness.

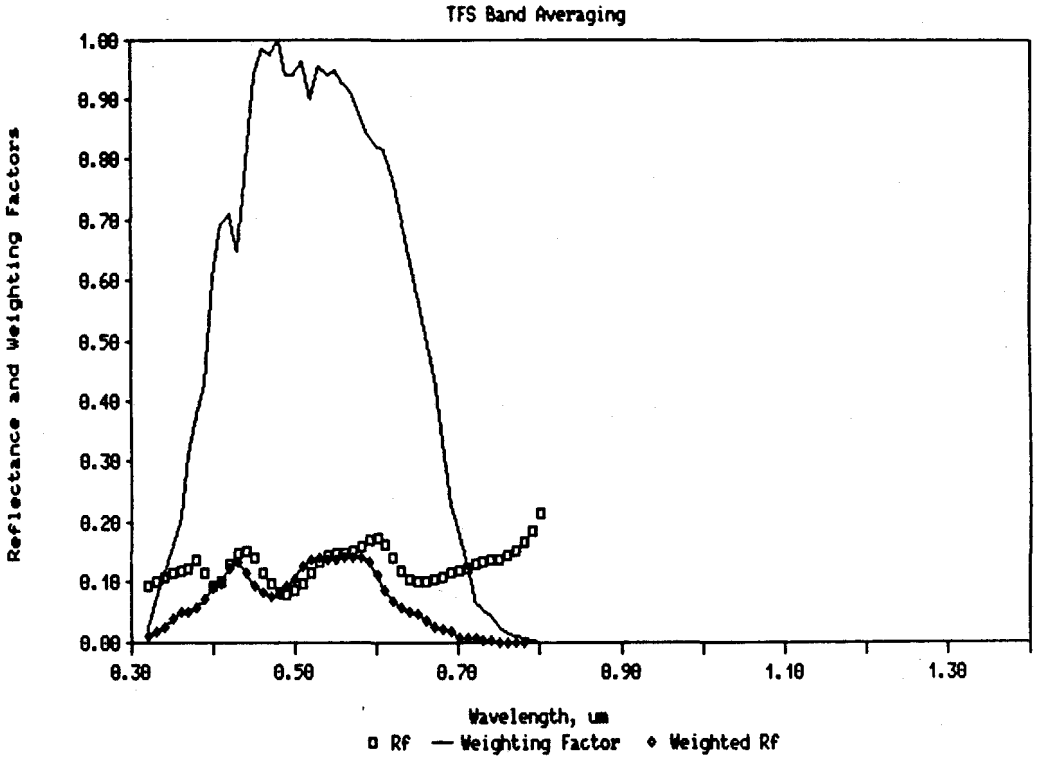

Fig. 3-19. Example of TFS band averaging for reflectance.

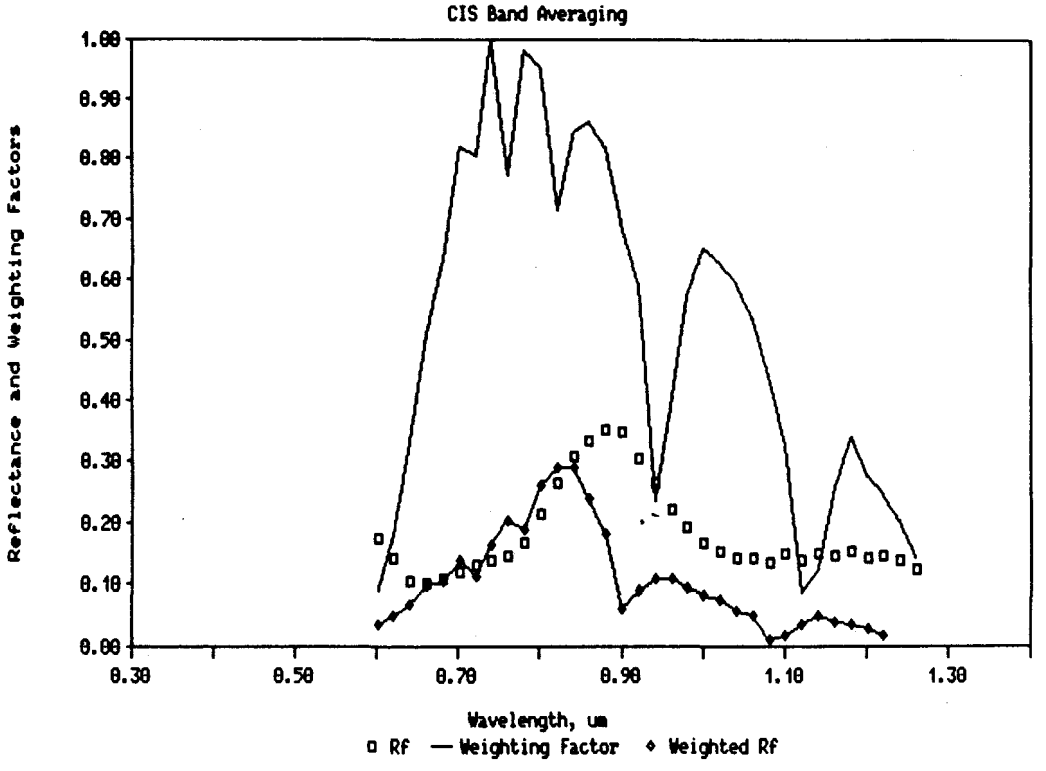

Fig. 3-20. Example of CIS band averaging for reflectance.

Table 3-4. Averaged optical factors and TFS device layer thicknesses.

FZO : Front ZnO Thickness
TFS : i-layer Thickness
BZO : Back ZnO Thickness

T/S	FZO	TFS	BZO	<R1>mtf	<R1>cis	<T1>tfs	<T1>cis
F1	0.5	0.15	0.5	0.127	0.196	0.173	0.668
F2	0.5	0.15	1.0	0.141	0.202	0.162	0.639
F3	0.5	0.15	1.5	0.146	0.212	0.152	0.599
F5	0.5	0.25	1.0	0.121	0.171	0.122	0.633
F6	0.5	0.25	1.5	0.150	0.213	0.122	0.609
F7	0.5	0.35	0.5	0.140	0.217	0.106	0.642
F8	0.5	0.35	1.0	0.124	0.194	0.101	0.621
F9	0.5	0.35	1.5	0.125	0.193	0.103	0.603
F10	1.0	0.15	0.5	0.101	0.154	0.118	0.573
F11	1.0	0.15	1.0	0.097	0.145	0.112	0.547
F12	1.0	0.15	1.5	0.101	0.147	0.113	0.533
F13	1.0	0.25	0.5	0.095	0.144	0.075	0.493
F14	1.0	0.25	1.0	0.092	0.137	0.080	0.529
F15	1.0	0.25	1.5	0.095	0.140	0.084	0.522
F16	1.0	0.35	0.5	0.101	0.160	0.071	0.549
F17	1.0	0.35	1.0	0.094	0.146	0.068	0.529
F18	1.0	0.35	1.5	0.109	0.165	0.070	0.523
F19	1.5	0.15	0.5	0.096	0.144	0.092	0.517
F20	1.5	0.15	1.0	0.098	0.142	0.087	0.485
F21	1.5	0.15	1.5	0.095	0.132	0.086	0.460
F22	1.5	0.25	0.5	0.089	0.137	0.062	0.485
F23	1.5	0.25	1.0	0.093	0.131	0.064	0.464
F24	1.5	0.25	1.5	0.126	0.176	0.055	0.382
F25	1.5	0.35	0.5	0.123	0.185	0.052	0.483
F26	1.5	0.35	1.0	0.095	0.143	0.049	0.449
F27	1.5	0.35	1.5	0.090	0.133	0.052	0.449

Table 3-5. TFS average device parameters and TFS device layer thicknesses.

FZO : Front ZnO Thickness
TFS : i-layer Thickness
BZO : Back ZnO Thickness

T/S	FZO	TFS	BZO	Voc	Jsc	ff	Eff
F1	0.5	0.15	0.5	0.825	8.510	0.313	2.200
F2	0.5	0.15	1.0	0.813	8.660	0.319	2.250
F3	0.5	0.15	1.5	0.828	11.750	0.446	4.340
F5	0.5	0.25	1.0	0.823	10.940	0.333	3.000
F6	0.5	0.25	1.5	0.811	11.780	0.344	3.290
F7	0.5	0.35	0.5	0.811	10.420	0.313	2.640
F8	0.5	0.35	1.0	0.821	10.240	0.322	2.710
F9	0.5	0.35	1.5	0.674	10.510	0.323	2.290
F10	1.0	0.15	0.5	0.716	13.610	0.636	6.200
F11	1.0	0.15	1.0	0.709	13.650	0.645	6.240
F12	1.0	0.15	1.5	0.642	13.510	0.691	5.990
F13	1.0	0.25	0.5	0.780	15.060	0.669	7.860
F14	1.0	0.25	1.0	0.764	14.980	0.667	7.640
F15	1.0	0.25	1.5	0.759	14.600	0.665	7.360
F16	1.0	0.35	0.5	0.811	15.600	0.665	8.410
F17	1.0	0.35	1.0	0.802	15.670	0.687	8.620
F18	1.0	0.35	1.5	0.798	15.350	0.672	8.240
F19	1.5	0.15	0.5	0.608	14.060	0.602	5.150
F20	1.5	0.15	1.0	0.597	14.340	0.558	4.780
F21	1.5	0.15	1.5	0.585	14.190	0.601	4.990
F22	1.5	0.25	0.5	0.650	15.630	0.615	6.240
F23	1.5	0.25	1.0	0.635	15.420	0.642	6.290
F24	1.5	0.25	1.5	0.640	15.010	0.648	6.220
F25	1.5	0.35	0.5	0.733	16.270	0.644	7.680
F26	1.5	0.35	1.0	0.722	16.140	0.627	7.310
F27	1.5	0.35	1.5	0.749	15.730	0.651	7.680

Table 3-6. CIS device parameters and TFS device layer thicknesses.

FZO : Front ZnO Thickness
TFS : i-layer Thickness
BZO : Back ZnO Thickness

T/S	FZO	TFS	BZO	Voc	Jsc	ff	Eff
F1	0.5	0.15	0.5	0.367	21.468	0.579	4.55
F2	0.5	0.15	1.0	0.365	20.458	0.572	4.26
F3	0.5	0.15	1.5	0.363	19.482	0.576	4.07
F5	0.5	0.25	1.0	0.362	19.623	0.575	4.08
F6	0.5	0.25	1.5	0.361	18.901	0.577	3.94
F7	0.5	0.35	0.5	0.363	19.810	0.577	4.15
F8	0.5	0.35	1.0	0.361	18.967	0.576	3.94
F9	0.5	0.35	1.5	0.357	17.937	0.575	3.69
F10	1.0	0.15	0.5	0.363	19.354	0.577	4.05
F11	1.0	0.15	1.0	0.361	18.410	0.577	3.83
F12	1.0	0.15	1.5	0.359	17.580	0.581	3.67
F13	1.0	0.25	0.5	0.359	18.207	0.578	3.78
F14	1.0	0.25	1.0	0.356	17.058	0.577	3.50
F15	1.0	0.25	1.5	0.357	16.763	0.579	3.47
F16	1.0	0.35	0.5	0.359	17.788	0.576	3.68
F17	1.0	0.35	1.0	0.357	16.916	0.579	3.50
F18	1.0	0.35	1.5	0.357	16.467	0.577	3.39
F19	1.5	0.15	0.5	0.360	17.911	0.577	3.72
F20	1.5	0.15	1.0	0.358	16.713	0.581	3.47
F21	1.5	0.15	1.5	0.355	15.659	0.577	3.21
F22	1.5	0.25	0.5	0.355	15.931	0.582	3.30
F23	1.5	0.25	1.0	0.352	15.457	0.576	3.13
F24	1.5	0.25	1.5	0.352	14.770	0.573	2.98
F25	1.5	0.35	0.5	0.357	16.345	0.578	3.37
F26	1.5	0.35	1.0	0.363	14.950	0.576	3.04
F27	1.5	0.35	1.5	0.351	14.614	0.578	2.97

Table 3-7. Tandem efficiency and TFS device layer efficiencies.

FZO : Front ZnO Thickness
TFS : i-layer Thickness
BZO : Back ZnO Thickness

T/S	FZO	TFS	BZO	TFS Eff	CIS Eff	Tandem Eff
F1	0.5	0.15	0.5	2.20	4.55	6.75
F2	0.5	0.15	1.0	2.25	4.26	6.51
F3	0.5	0.15	1.5	4.34	4.07	8.41
F5	0.5	0.25	1.0	3.00	4.08	7.08
F6	0.5	0.25	1.5	3.29	3.94	7.23
F7	0.5	0.35	0.5	2.64	4.15	6.79
F8	0.5	0.35	1.0	2.71	3.94	6.65
F9	0.5	0.35	1.5	2.29	3.69	5.98
F10	1.0	0.15	0.5	6.20	4.05	10.25
F11	1.0	0.15	1.0	6.24	3.83	10.07
F12	1.0	0.15	1.5	5.99	3.67	9.66
F13	1.0	0.25	0.5	7.86	3.78	11.64
F14	1.0	0.25	1.0	7.64	3.50	11.14
F15	1.0	0.25	1.5	7.36	3.47	10.83
F16	1.0	0.35	0.5	8.41	3.68	12.09
F17	1.0	0.35	1.0	8.62	3.50	12.12
F18	1.0	0.35	1.5	8.24	3.39	11.63
F19	1.5	0.15	0.5	5.15	3.72	8.87
F20	1.5	0.15	1.0	4.78	3.47	8.25
F21	1.5	0.15	1.5	4.99	3.21	8.20
F22	1.5	0.25	0.5	6.24	3.30	9.54
F23	1.5	0.25	1.0	6.29	3.13	9.42
F24	1.5	0.25	1.5	6.22	2.98	9.20
F25	1.5	0.35	0.5	7.68	3.37	11.05
F26	1.5	0.35	1.0	7.31	3.04	10.35
F27	1.5	0.35	1.5	7.68	2.97	10.65

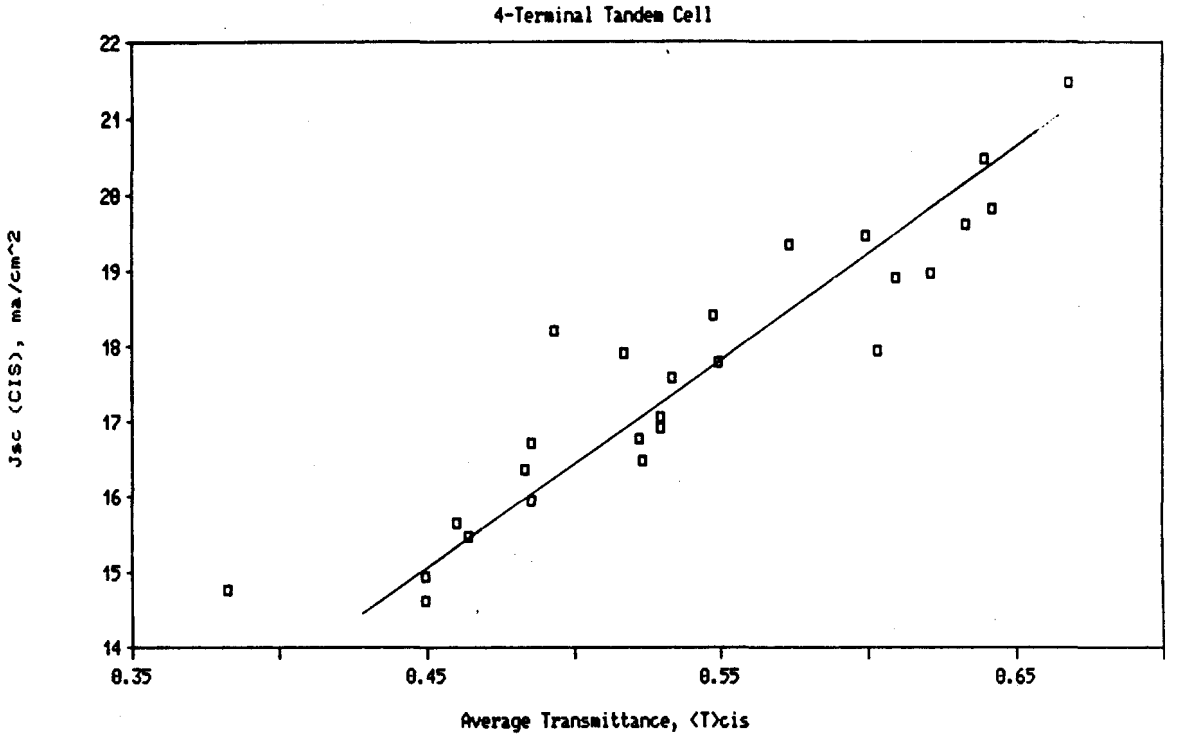

Fig. 3-21. CIS J_{sc} dependence on average transmittance.

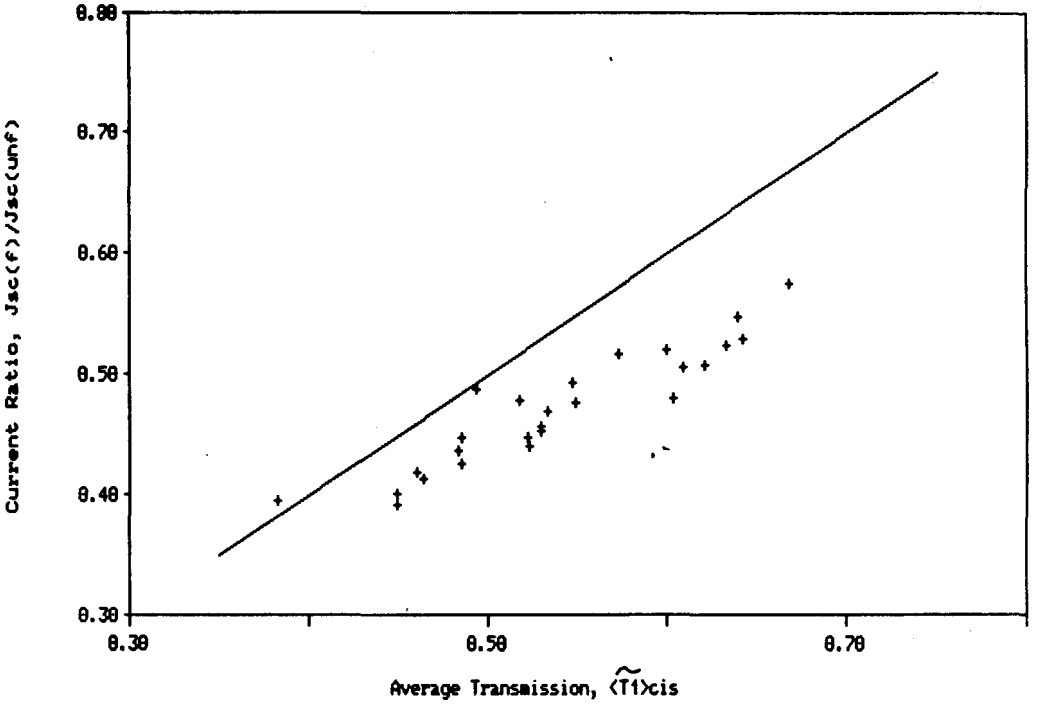

Fig. 3-22. CIS short circuit current ratio.

slope of the correlation line is not one and that the Jsc for the CIS is about 10-20% lower than predicted by $\langle T_1 \rangle_{cis}$. Part of this difference can be ascribed to the absorption of light by the CIS device front ZnO layer. This would account for 2.5 to 7.5% of the variation since that is the range of absorptivity of this layer. The balance of the difference is due mostly to the R_2 reflectance of the ZnO/Cd/CIS interface which T_1 does not include. A final check on the model is provided by comparing the measured Jsc of the CIS cell under different filters to that calculated from spectral response data. Figure 3-23 shows a comparison plot of the ratios of the filtered Jsc values to the unfiltered values for the cell tester measured values with the QE integrated values. These values are shown in Table 3-8. Again the conclusion is that linear relationships hold, but that the data do not follow theory exactly. Further work will be required to elucidate the causes of these differences. In any case we have gained confidence that the averaged optical parameters such as $\langle T_1 \rangle_{cis}$ have use in predicting performance of cells in tandem modules.

Next we consider the dependence of other parameters on the averaged optical functions. Jsc for TFS and CIS have an opposing trend as a function of the average transmittance in the CIS band as shown in Fig. 3-24. This effect is due to several causes. Values of high $\langle T_1 \rangle_{cis}$ occur for thin TFS i-layers and for thin layers of front ZnO transparent conductors. Thin layers of TFS cause the expected reduction in TFS Jsc. The thin front TC layers are smoother and contribute less to the scattering required to obtain high Jsc. Statistical analysis of the data as a three factor, three level experiment shows that the current enhancement due to TC thickness is four times larger than the effect due to i-layer thickness. The region of equal currents extends from $\langle T_1 \rangle_{cis}$ values of 0.35 to 0.50. This would be the feasible operation region for these devices in a two terminal, series connected configuration. As Fig. 3-25 shows, the upper range of this region is where the maximum in the tandem efficiency is found.

The dependence of Voc and fill factor for the TFS and CIS cells is shown in Fig. 3-26 as a function of $\langle T_1 \rangle_{cis}$. The CIS curves show that the efficiency of the CIS cell depends only on Jsc. Consequently, we expect that the efficiency of the CIS device should depend linearly on $\langle T_1 \rangle_{cis}$ based on the data shown in Fig. 3-22. The data in Fig. 3-26 for TFS show, however, a strong dependence on the average transmission in the CIS band. This is of course an indirect effect. The values for $\langle T_1 \rangle_{cis}$ above 0.60 correspond to very thin front TC layers which caused high series losses. These losses reduced the fill factor to about 0.30. A weak minimum may perhaps be perceived in the fill factor for values of $\langle T_1 \rangle_{cis}$ at 0.53. The Voc for the TFS cells seems to show a general increase for high values of $\langle T_1 \rangle_{cis}$. Statistical analysis shows this effect to be real and to correlate most strongly with thin front ZnO layers. It is not clear what causes this effect.

Table 3-8. Comparison of CIS calculated J_{SC} and measured J_{SC}.

Filter	J_{SC} (meas)	J_{SC} (QE)
No Filter	37.36	36.54
F1	21.47	19.46
F17	16.92	14.66
F27	14.61	12.51

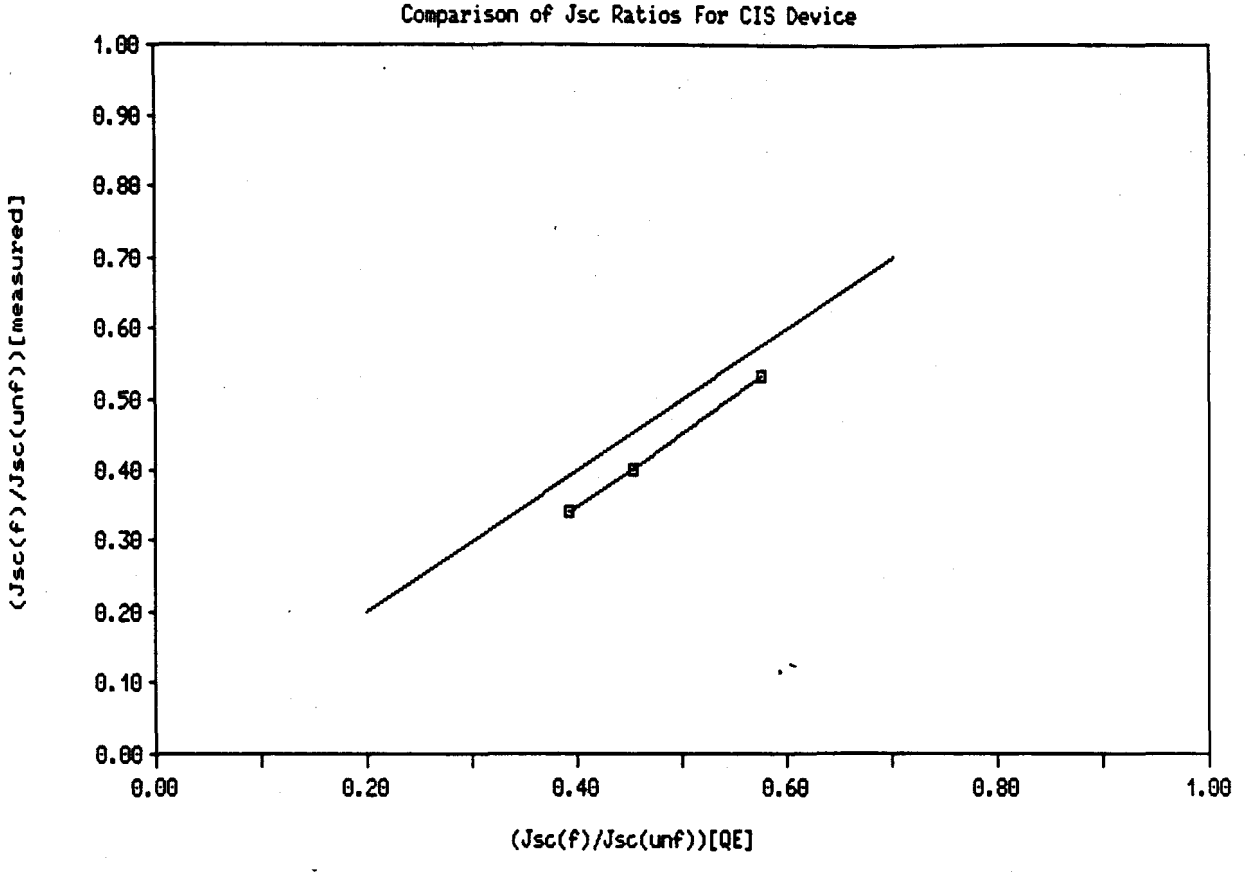

Fig. 3-23. Comparison of J_{SC} ratios for CIS devices.

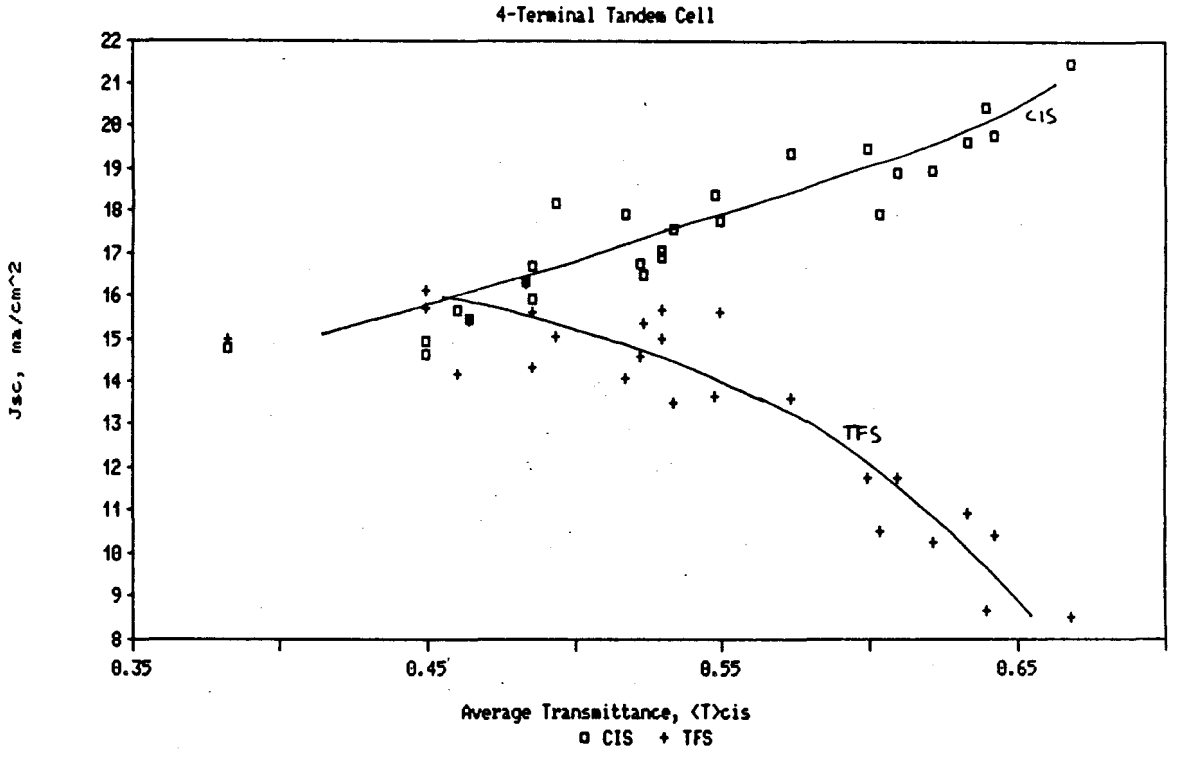

Fig. 3-24. Dependence of cell currents on average transmittance.

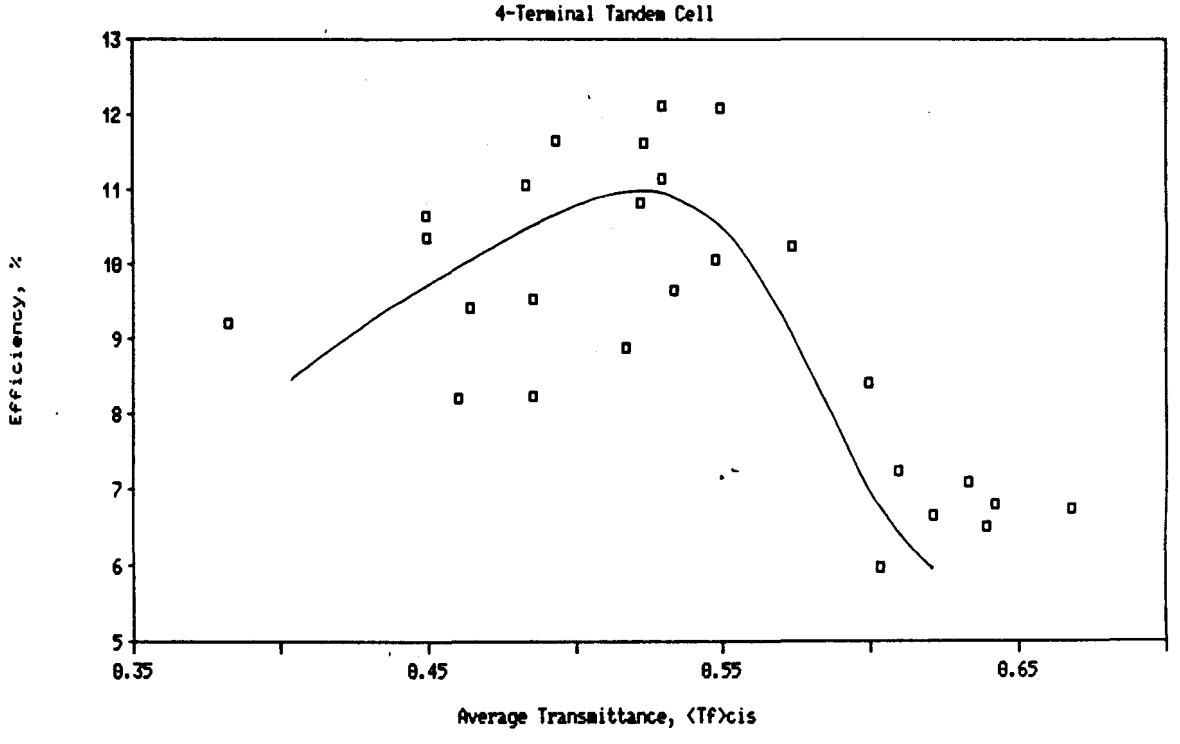

Fig. 3-25. Dependence of tandem total efficiency on average transmittance.

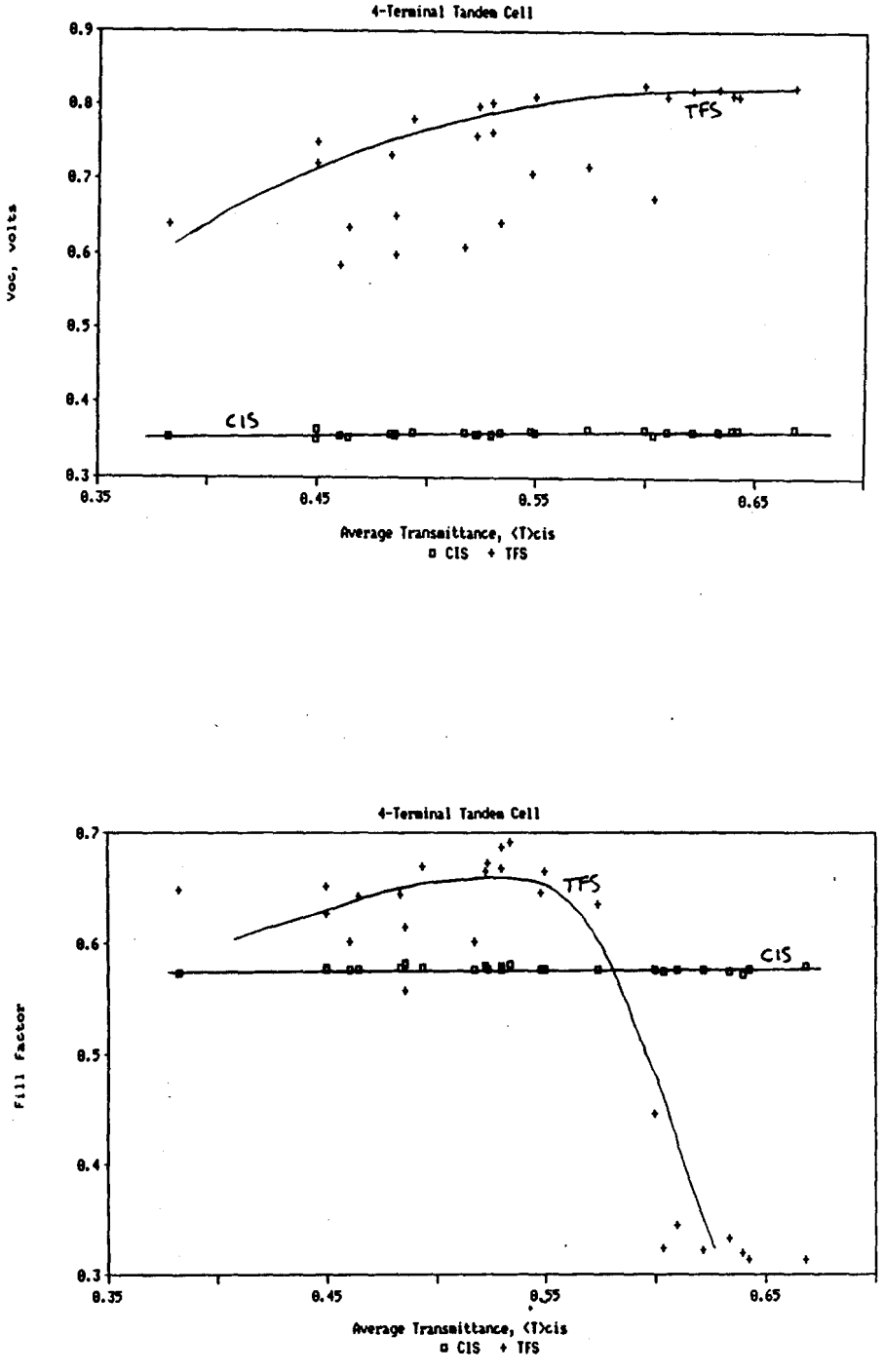

Fig. 3-26. Dependence of TFS and CIS V_{oc} and fill factor on $\langle T1 \rangle_{cis}$.

The effect on TFS and CIS cell performance due to the average front reflectivity is more difficult to interpret. Figure 3-27 shows the dependence of cell efficiency on $\langle R_1 \rangle_{tfs}$ for TFS and CIS. The scatter in the TFS data is large indicating that several effects are interacting strongly and that $\langle R_1 \rangle_{tfs}$ is not a leveraging indicator of performance. The highest efficiency TFS devices do correspond to the lower values of $\langle R_1 \rangle_{tfs}$. The dependence for CIS devices is weak. Figure 3-28 shows the data for the CIS band averaged front reflectance, $\langle R_1 \rangle_{cis}$. Again the data for TFS are widely scattered. The important aspect of this data set is that the values for $\langle R_1 \rangle_{cis}$ are so high: 0.13-0.21. This is important because it represents radiation which never enters the tandem module, it is reflected away before it can do any good.

The spectra for the best TFS layer combination are shown in Fig. 3-29. The value for the CIS band averaged front surface reflection, $\langle R_1 \rangle_{cis}$, is quite high at 0.146. This is probably due to a strong mismatch in the index of refraction at the ZnO/TFS boundary. In the CIS tandem absorption band from 0.6 to 1.3 micron the index of refraction of ZnO rapidly decreases from 1.9 to about 1.2 due to anomalous dispersion from the plasma absorption in the near IR. If the ZnO had an index of 1.9 to 2.1, as found in low conductivity samples, there would be an index matching effect to assist the transition from glass at 1.5 to TFS at 4.0. Index matching would reduce the reflections at the optical interface from glass to TFS. The absence of matching causes higher than anticipated reflection at this boundary. There is a resultant trade-off since the TC layers favor high conductivity with the accompanying plasma absorption which cause the anomalous dispersion.

3.2.4.3 Tandem Efficiency and Layer Thicknesses

A direct comparison of the effect of the variation in the three TFS layer thicknesses on tandem efficiency is shown in Figs. 3-30 through 3-32. The most important effect is that due to the thickness of the front layer. A relative maximum appears for a front layer thickness of 1.0 micron. The trade-off against greater thicknesses seems to be primarily due to the increase in scattering of the useful CIS radiation away from the CIS cell which is not balanced by increased currents in the TFS device. Examination of the I-V curves for the TFS cells show that the increase in thickness does not improve the fill factor. This indicates that for this cell current collection geometry 1.0 micron ZnO layers are thick enough to prevent significant series resistance losses in the TFS cell. Figure 3-31 shows that the back ZnO thickness does not correlate with tandem performance. The i-layer thickness dependence shown in Fig. 3-32 is weak. For i-layers in the range of 0.25 to 0.35 the trade-off of TFS current with CIS current is relatively balanced. Tanner's work shows that thicknesses above 0.35 micron should see a significant reduction in $\langle T_1 \rangle_{cis}$.

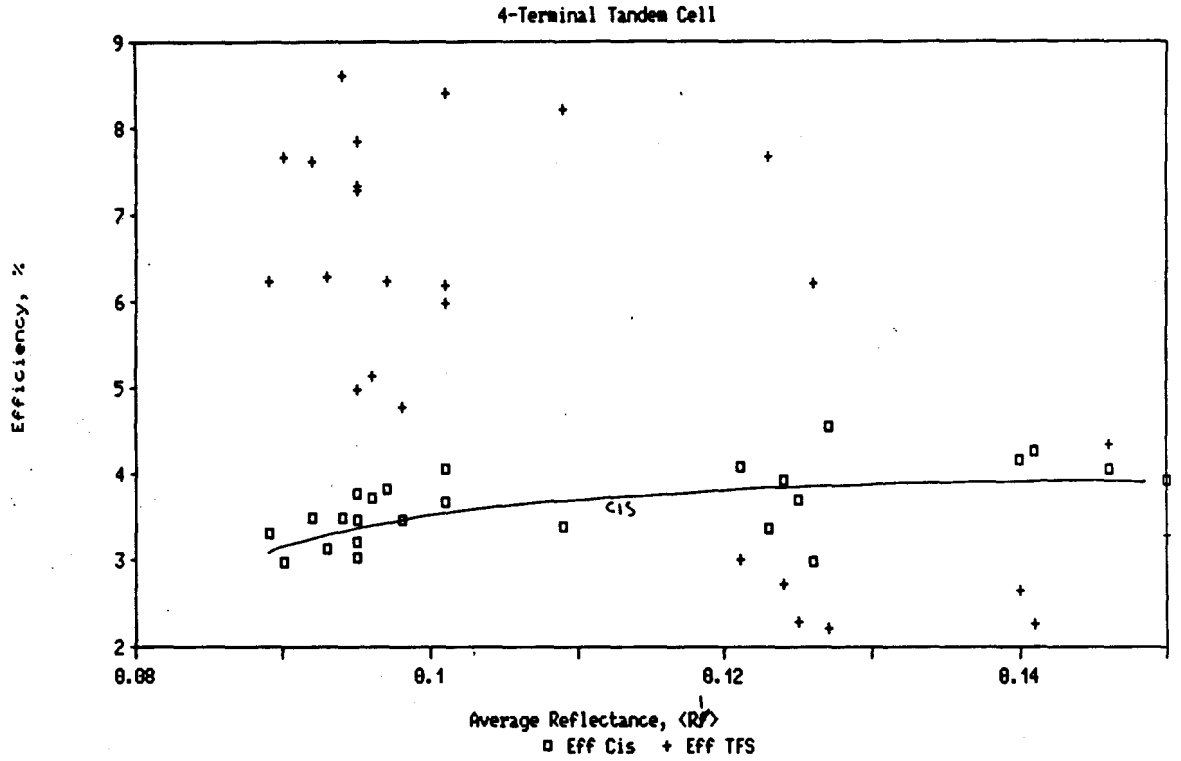

Fig. 3-27. Cell efficiencies as a function of $\langle R1 \rangle_{tfs}$.

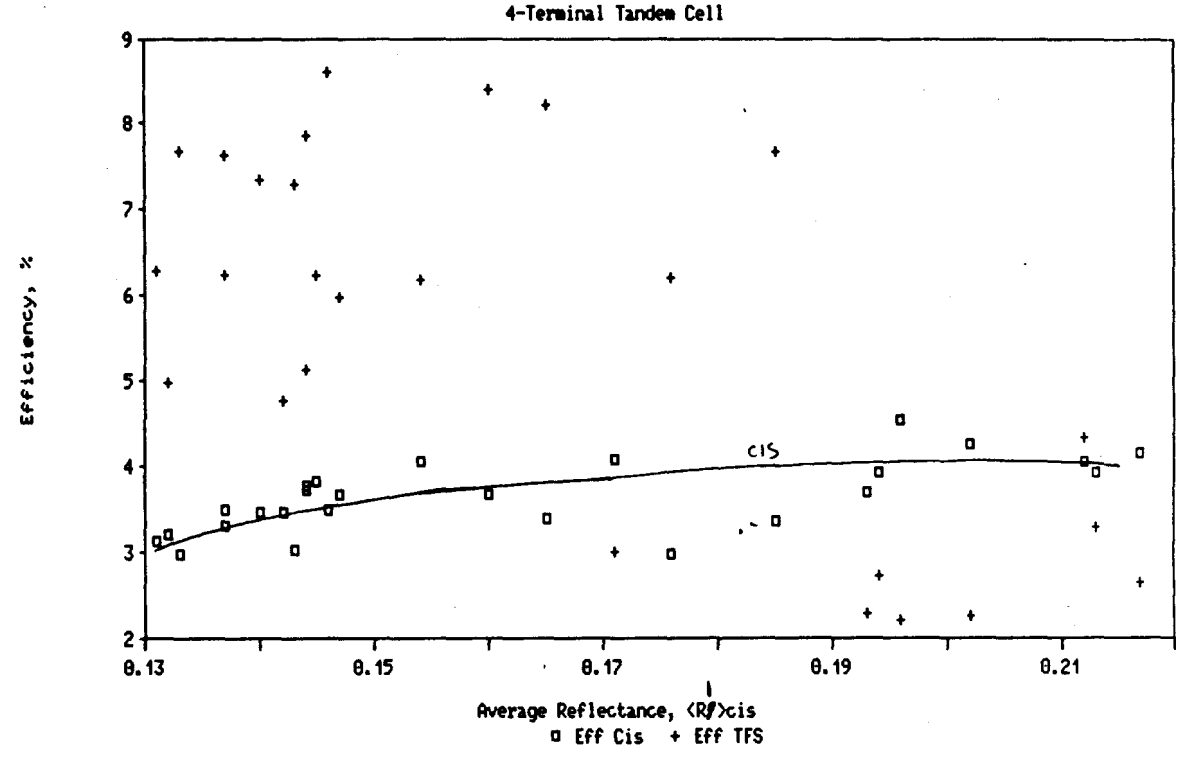

Fig. 3-28. Cell efficiencies as a function of $\langle R1 \rangle_{cis}$.

Thicknesses: 1.0/0.35/1.0
<T>cis=0.529, <Rf>cis=0.146

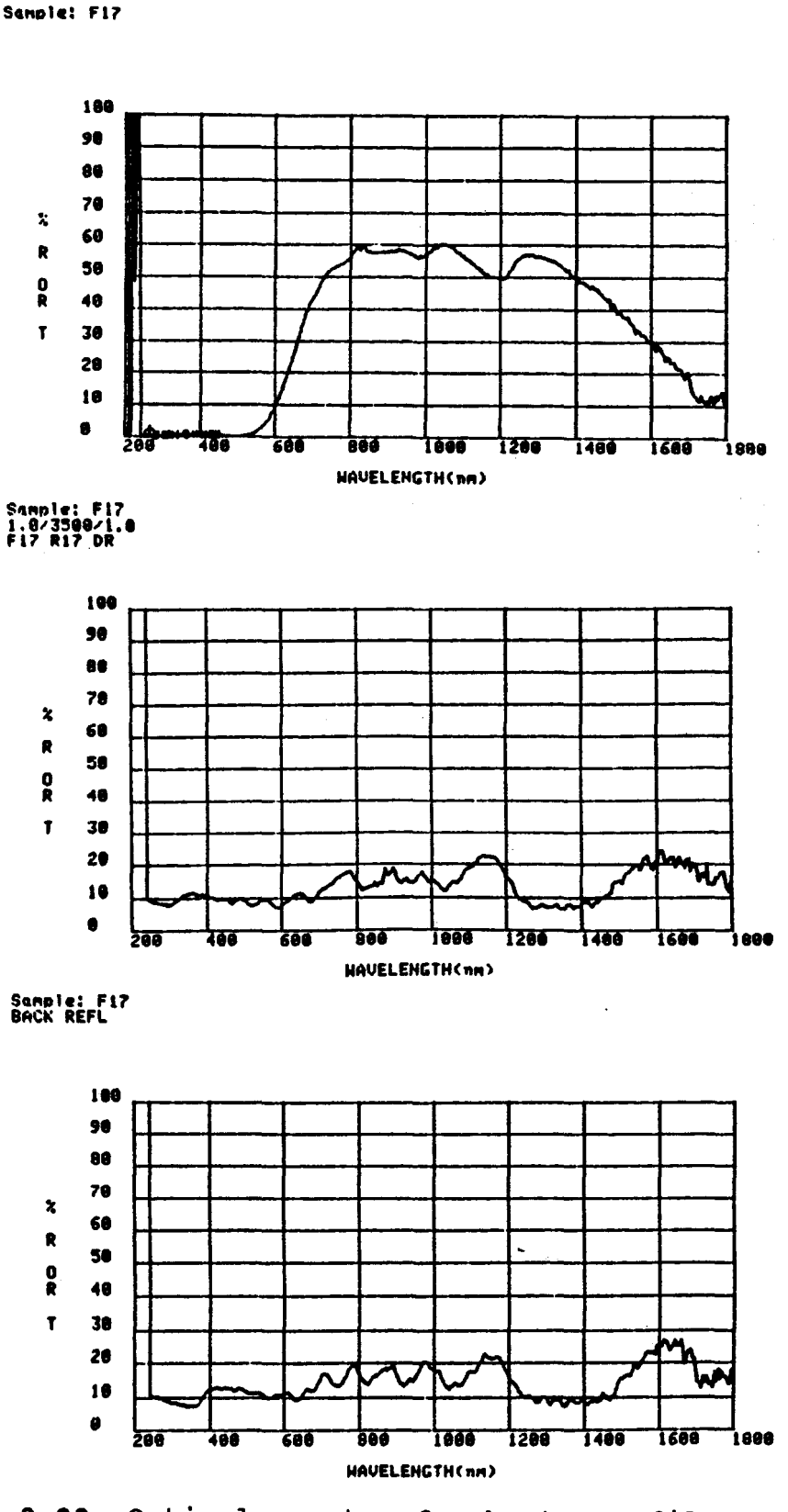

Fig. 3-29. Optical spectra for best TFS filter/cell.

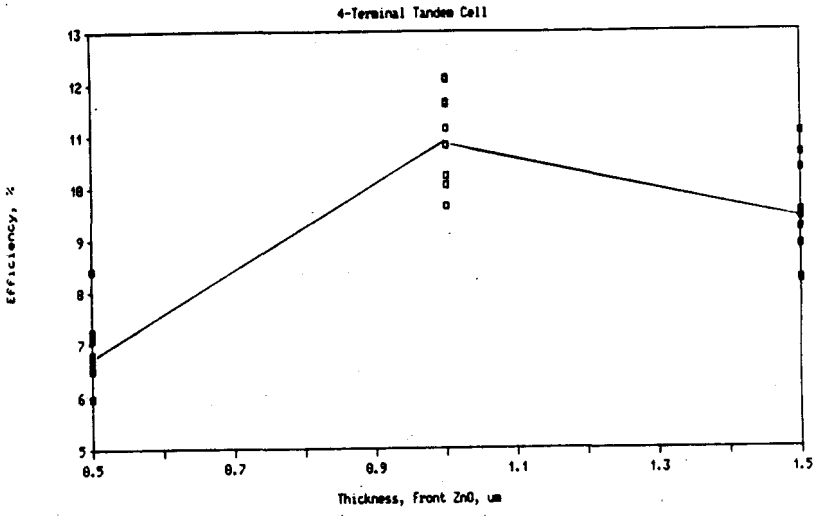

Fig. 3-30. Dependence of tandem total efficiency on front ZnO thickness.

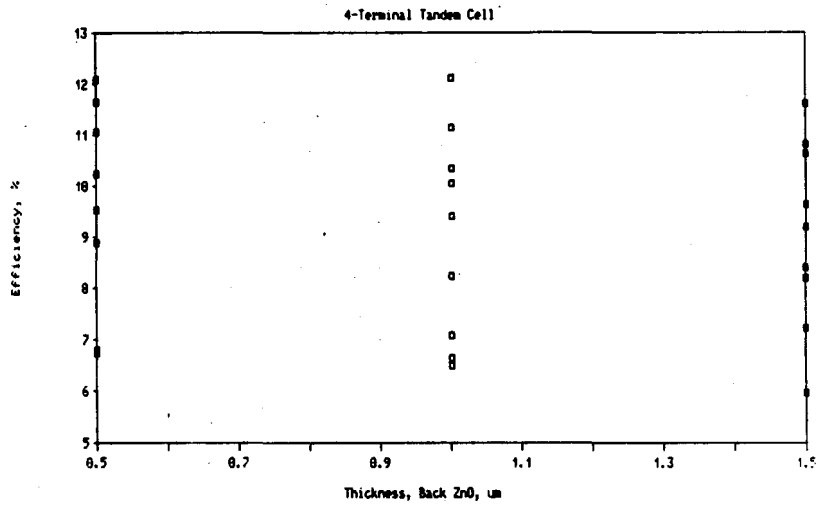

Fig. 3-31. Dependence of tandem total efficiency on back ZnO thickness.

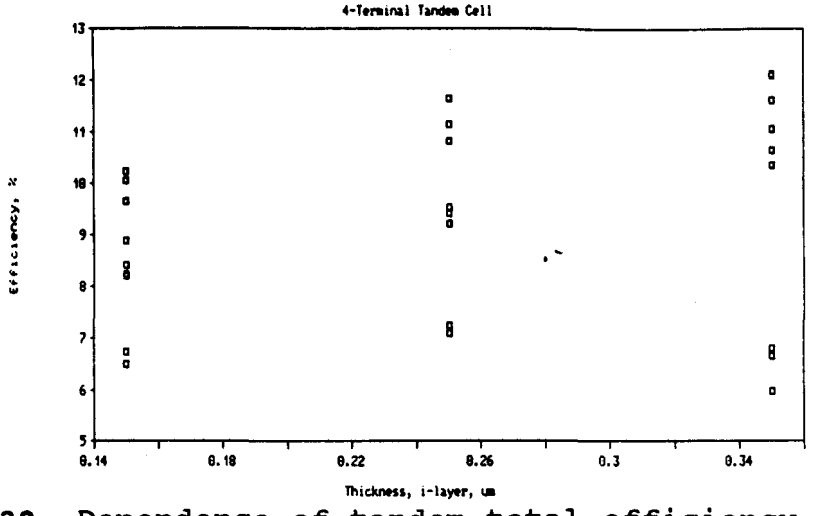

Fig. 3-32. Dependence of tandem total efficiency on TFS i-layer thickness.

3.2.4.4 Optical Losses in the Tandem Configuration

It is desirable to total up the losses which occur in the tandem device to determine which problems should be worked on. This can be done by using the weighted average of Eq. 3-1 in the CIS band for instance:

$$\langle A_1 \rangle_{cis} = 1 - \langle R_1 \rangle_{cis} - \langle T_1 \rangle_{cis}. \qquad (3\text{-}1)$$

The calculated value of $\langle A_1 \rangle_{cis}$ corresponds to losses in the TFS device in the CIS absorption band which are not accounted for by the reflection from the front surface or by transmission through the stack. Such losses include the absorption losses in the transparent conductors as well as effective losses due to high angle scattering and optical trapping which prevents the radiation from reaching the bottom CIS cell. Figure 3-33 shows the calculated values for $\langle A1 \rangle_{cis}$ as a function of front ZnO thickness. This variable seems to be the only one upon which $\langle A_1 \rangle_{cis}$ depends. The main conclusion is that 40 to 45% of the useful CIS light disappears in the TFS structure for TC thicknesses greater than 1.0 micron. This is a large amount of loss. The expected losses due to absorption by the TC layers is in the range of 5-15% based on the absorption coefficient for ZnO in this spectral band. The missing 25-35% of loss must be due to the scattering processes.

3.2.5 Future Work and Directions for Progress

A different view of the problem faced for increasing the efficiency of practical tandem devices is provided by Fig. 3-34. In this figure the relationship of the measured short circuit currents for CIS and the TFS cells is shown. Basically the currents anti-correlate. The direction for progress is to increase the Jsc of the CIS device without decreasing the current of the TFS device. This direction is shown by the arrow, which is at variance with the trend of the current data set.

This means that some significant change in approach is required to look for higher efficiency alternatives. The most obvious is to test the effect of using much smoother TC layers. This will have the effect of perhaps only modestly decreasing the TFS current while yielding a large increase in the CIS current. This is somewhat at variance with the dictum to marry optimal tandem cells to obtain the best tandem module.

Several conclusions can be deduced form the work carried out so far:

1. The crucial factor affecting CIS tandem cell performance is the higher than expected optical losses in the TFS stack. This loss function varied from 0.22 to 0.50.

2. The front transparent conductor controls the large losses.

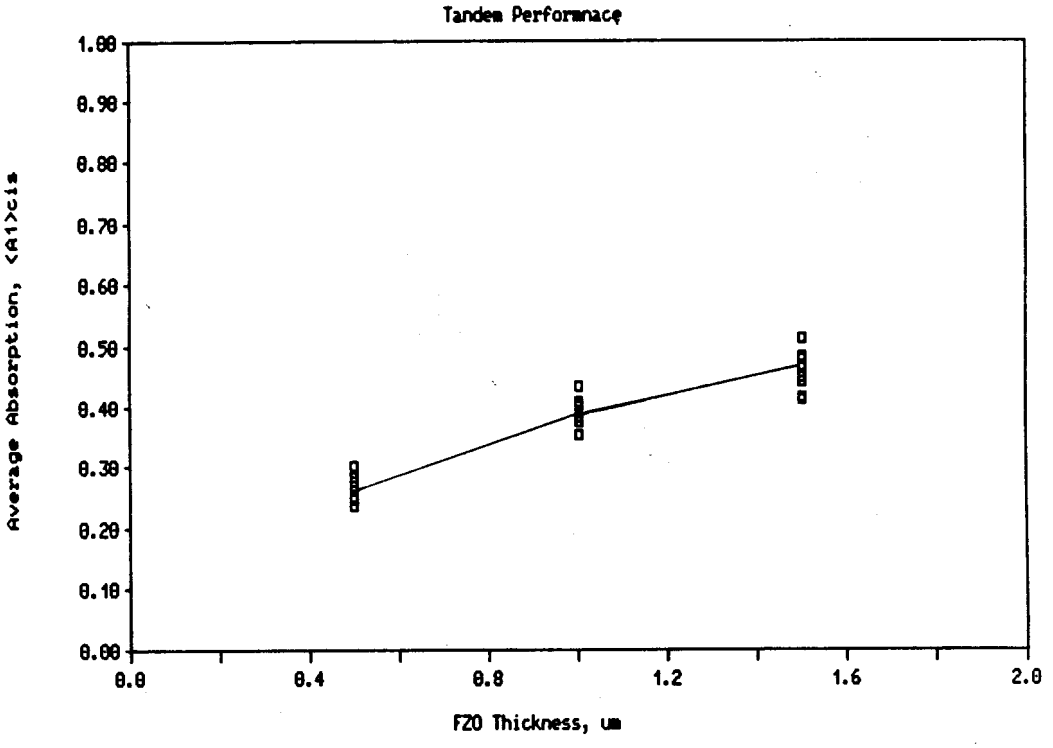

Fig. 3-33. Calculated average effective absorption in TFS structures in the CIS band, $\langle A_1 \rangle_{cis}$.

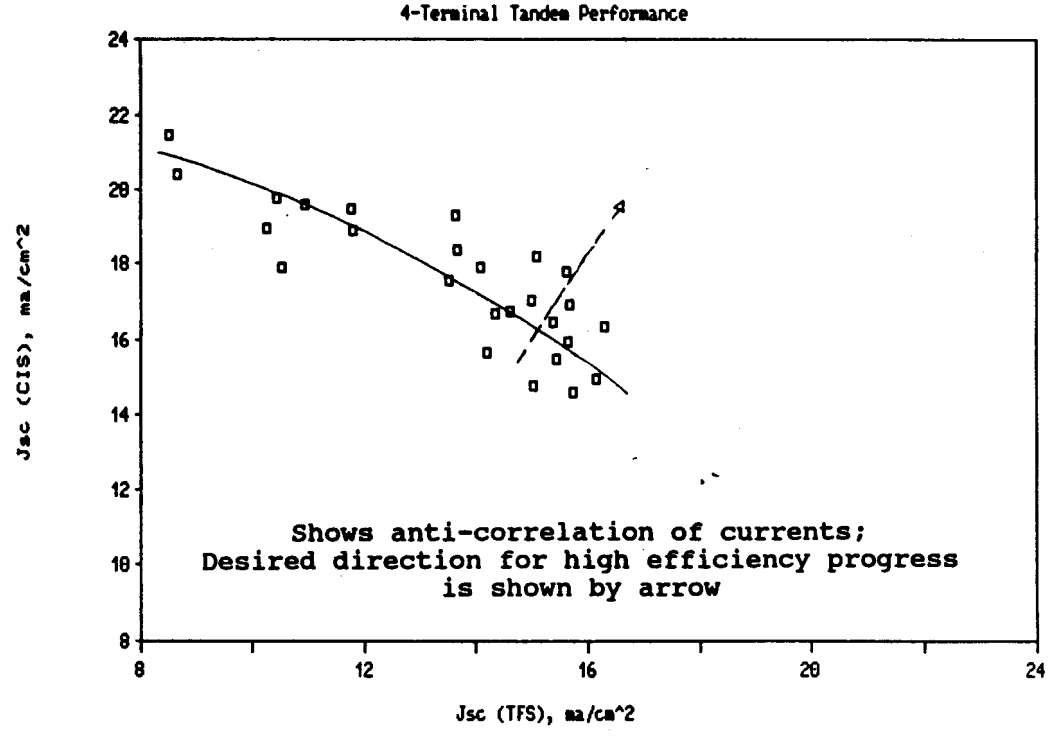

Fig. 3-34. Relation of cell currents in tandem configuration.

The losses appear to arise from two effects: TC layer absorption loss and large scattering of CIS band radiation.

3. The front reflection losses in both the TFS and CIS bands are higher than expected. In particular $\langle R_1 \rangle_{cis}$ ranges from 0.12 to 0.19 and is probably due to index mismatch at the ZnO/TFS interface.

4. The use of averaged optical quantities over relevant device spectral response bands is a useful technique for assessing the importance of various losses in tandem devices. The short circuit current of the bottom cell depends linearly on the average weighted transmittance in its response band.

The next steps are in process to unravel the optical issues. The goal is to accurately assess the fate of all the photons in the structure using a predictive model. This model will be used to point the direction of research to improve the efficiency of the complete device.

1. Measure performance response surface for the tandem device using smooth ZnO and thicker i-layers. This will assess the relative importance of TC surface smoothness in determining device efficiency. We expect $\langle T \rangle_{cis}$ to increase dramatically.

2. Using standard optical methods accurately measure the absorption losses in the ZnO films. Then assess the relative importance of these losses compared with scattering losses.

3. Look for ways to reduce $\langle Rf \rangle_{cis}$ using standard thin film optical methods as a guide for experiments. This approach is along the lines of thin film optical filter development.

4. Refine the photon counting and efficiency calculation using a detailed optical and current generation model.

5. Include the effects of rough surface scattering into a model for prediction of short circuit current and other optical losses.

3.3 REFERENCES

References for Section 3.1

1. D.L. Morel, K. Mitchell, R. Wieting, R. Potter, C. Eberspacher, D. Tanner, C. Fairchild. Proc. 18th Photovoltaic Specialists Conf., p. 876-882 (1985).
2. E. Berman, K.W. Mitchell. Proc. 7th European Photovoltaic Solar Energy Conf., Sevilla, Spain, p. 442-451 (1986).
3. K. W. Mitchell. Proc. First International Photovoltaic Science and Engineering Conf., Kobe, Japan, p. 691-694 (1984).
4. K.W. Mitchell. Solar Cells, 21:127-134 (1987).
5. K. Mitchell, C. Eberspacher, R. Wieting, J. Ermer, D. Willett, K. Knapp, D. Morel, R. Gay. Proc. Third International Photovoltaic Science and Engineering Conf., Tokyo, Japan, p. 443-448 (1987).

References for Section 3.2

1. Tanner, D. P., et al., Transparent Solar Modules, 18th IEEE PVSC (1985)
2. Mitchell, K. W., et al., High Efficiency Thin Film Tandem PV Modules, 5/87, 19th IEEE PVSC.
3. Mitchell, K. W., et al., Performance Modeling of Thin Film Tandem PV Modules, 5/87, 19th IEEE PVSC.
4. Mitchell, K. W., Device Aspects of Multijunction Photovoltaic Module Research, Solar Cells, 21, (1987), 127-134.
5. Mitchell, K. W., et al., Status of Thin Film Tandem PV Module Development, 11/87 3rd Intl PVSEC.
6. Eskenas, K. L. and Mitchell, K. W., (1985).
7. Berning, P. H., "Theory and Calculations of Optical Thin Films", in Physics of Thin Films (1), 1963, Academic Press, New York, NY, 1963, pp. 69-121. See equations (91)-(95).

Document Control Page	1. SERI Report No. SERI/STR-211-3350	2. NTIS Accession No.	3. Recipient's Accession No.

4. Title and Subtitle

Research on Amorphous-Silicon-Based Thin-Film Photovoltaic Devices, Semiannual Subcontract Report, 1 July 1987--31 December 1987

5. Publication Date: May 1988

6.

7. Author(s)

W. Bottenberg, K. Mitchell, and R. Wieting

8. Performing Organization Rept. No.

9. Performing Organization Name and Address

ARCO Solar, Inc.
Camarillo, California 93010

10. Project/Task/Work Unit No. PV840201

11. Contract (C) or Grant (G) No.

(C) ZB-7-06003-3

(G)

12. Sponsoring Organization Name and Address

Solar Energy Research Institute
1617 Cole Boulevard
Goden, Colorado 80401-3393

13. Type of Report & Period Covered: Technical Report

14.

15. Supplementary Notes

SERI Technical Monitor: W. Luft

16. Abstract (Limit: 200 words)

The objective of this work is to develop 13% (aperture area) efficient, 850-cm^2 four-terminal hybrid tandem submodules. The module design consists of a copper-indium-diselenide (CIS)-based bottom circuit and a semitransparent, thin-film silicon-hydrogen (TFS)-based top circuit. High-performance, semitransparent TFS devices and submodules were fabricated in which ZnO was used in the front and rear transparent conductors. High-performance CIS devices and submodules were also fabricated; however, the location and nature of the junction are not yet understood. Representative four-terminal hybrid tandem devices and submodules were fabricated from TFS and CIS component circuits. Optical coupling between the circuits was lower than expected, because of reflection losses at key interfaces. Efficiencies obtained for these devices and modules include 14.17% for a four-terminal, 4-cm^2 tandem cell and 12.3% for a four-terminal, tandem module.

17. Document Analysis

a. Descriptors: Photovoltaic cells ; silicon solar cells ; copper selenide solar cells ; thin films

b. Identifiers/Open-Ended Terms

c. UC Categories

270

18. Availability Statement

National Technical Information Service
U.S. Department of Commerce
5285 Port Royal Road
Springfield, Virginia 22161

19. No. of Pages: 107

20. Price: A06

Form No. 0069 (6-30-87)